Scholars' Mine

Doctoral Dissertations

Student Theses and Dissertations

Summer 2018

The significance of grouping and missed bubbles on interfacial area concentration and void fraction

Chandller Stephen-Leslie Mills

Follow this and additional works at: https://scholarsmine.mst.edu/doctoral_dissertations

Part of the Nuclear Engineering Commons, and the Thermodynamics Commons

Department: Mining and Nuclear Engineering

THE SIGNIFICANCE OF GROUPING AND MISSED BUBBLES ON INTERFACIAL

AREA CONCENTRATION AND VOID FRACTION

by

CHANDLLER STEPHEN-LESLIE MILLS

A DISSERTATION

Presented to the Faculty of the Graduate School of the

MISSOURI UNIVERSITY OF SCIENCE AND TECHNOLOGY

In Partial Fulfillment of the Requirements for the Degree

DOCTOR OF PHILOSOPHY

in

NUCLEAR ENGINEERING

2018

Approved by:

Joshua Schlegel, Advisor
Gary Mueller
Carlos Castano
Hyoung-koo Lee
Joseph Smith

ABSTRACT

The two-fluid model is used in nuclear reactor safety codes. Two of the important constitutive relations will be discussed in this study, the interfacial area concentration and void fraction. The Interfacial area concentration is directly affected by the number of bubbles and how these bubbles are categorized into groups. In this study, a new algorithm was implemented to account for trailing bubbles, bubbles with short response times, and the categorization of bubbles based upon diameter for all group 1 bubbles. The optical and conductivity probes were used to determine the void fraction and interfacial area concentration in a bubble column. The new algorithm was benchmarked against the previous algorithm. The data acquisition systems for both probes were set at 22 kHz. This is sufficient for the optical probe. However, due to the response time of the conductivity probe, the previous algorithm does not pick up all the bubbles at the 22 kHz sampling rate. There is an increase of up to 28% for the total interfacial area concentration when the trailing bubbles are collected, and bubble diameter is used instead of chord length for the optical probe. The conductivity probe for the 22k Hz sample rate in the new version, collects more bubbles than the previous version. The total void fraction for the conductivity probe is within 15% of the optical probe for the locations tested. The total interfacial area concentration is up to 80% higher than the optical probe. Additional testing should be completed at higher sampling rates to determine the overall accuracy when comparing the conductivity probe to the optical probe for the new algorithm. The higher sampling rate should increase the accuracy for determining the front and rear interface location for all bubbles in the system.

ACKNOWLEDGMENTS

TABLE OF CONTENTS

LIST OF ILLUSTRATIONS

LIST OF TABLES

1. INTRODUCTION

At present, about twenty percent of the electric power produced in the United States comes from nuclear reactors, and a safety of these reactor systems is always under scrutiny. All new reactors need to pass the performance evaluation (i.e., licensing prior to construction). A critical step in the licensing process is an extensive test of the safety of the nuclear reactor through computational simulations. Thus, simulated tests of various accident scenarios and conditions help to forecast the safety performance and to identify potential weaknesses in reactor systems. At present, the computational tools used for simulations of reactor systems include Reactor Excursion and Leak Analysis Program (RELAP), Transient Reactor Analysis Code (TRAC), and TRAC/RELAP Advanced Computational Engine (TRACE). In nuclear reactor safety codes like RELAP5, the one-dimensional nature of the field equations in the two-fluid model prevents a direct simulation of effects of many parameters. The effects of many parameters such as velocity or energy should be obtained from algebraic terms. The algebraic terms to the conservation equations are based on experimental results and not from complete physical ideologies. However, the correlations used in RELAP5 are sometimes dependent upon engineering judgment. In the cases where judgments are made, there is room for improvement.

In reactor systems, steam and water mixture creates a two-phase flow. The most practical model for representing two-phase flows is the two-fluid model [1]. The void fraction (VF) and interfacial area concentration (IAC) are important constitutive relations for the two-fluid model. They are necessary for calculating the interfacial transfer of mass,

momentum, and energy between the two phases [1]. The VF represents the amount of dispersed phase in a two-phase mixture, as shown by Equation 1.

$$\alpha_g = \frac{\text{Total volume of dispersed phase}}{\text{Total volume}} \tag{1}$$

The IAC represents the amount of surface area available for transfer of mass, momentum, or energy per unit volume of the mixture, as indicated in Equation 2:

$$a_i = \frac{\text{Total surface area of dispersed phase}}{\text{Total volume}} \tag{2}$$

Models for IAC and VF are tested using detailed experimental data. One of the most common methods for measuring IAC and VF is the four-sensor conductivity probe [2,3].

The four-sensor conductivity probe is an intrusive measurement technique that uses the difference in conductivity between two phases to measure local parameters in two-phase flows. The four-sensor conductivity probe combines the four sensors into three two-sensor pairs to calculate IAC in the system independent of bubble shape. Conductivity probes have been used because of their simplicity and capability for measuring local parameters. The conductivity probe is used to avoid averaging the IAC over the cross-sectional area of a flow channel. There are a few shortcomings when using conductivity probes. First, the response time of the circuit causes a rise time in the system for individual bubbles. The response time will lead to bubbles that are close to one another to miss a sensor. Second, the shape of the bubbles cannot be determined in the center of pipes, causing a reliance on the chord length of bubbles. The chord length is used as an estimation for smaller bubbles, leading to inaccuracies in group IAC.

The goal of the present study is to improve the accuracy of IAC and VF measurements. The three major areas of focus are the signal smoothing process, the pairing criteria, and the grouping of bubbles.

In the current smoothing process, the signal filtering system misses some bubble interfaces. In the case of one large bubble with multiple trailing bubbles, this can lead to fewer, larger bubbles being counted, resulting in an underestimation of the actual IAC. The goal of this work is to improve the filtration system by improving the normalization process and locating the peaks in the smoothing process for calculating IAC in the system. The improved filtration system will ensure the bubbles from the signal sensor represent the bubbles' actual size.

The pairing criterion also needs to be able to pick up the smaller bubbles that previous smoothing processes might miss. These "missing bubbles" are those that do not contact all four of the probe sensors. They are currently distributed evenly between bubble groups. However, smaller bubbles have a higher probability of missing one or more sensors than large bubbles. The new algorithm will place missing bubbles into smaller bubble groups, rather than distributing them evenly. This will allow an accurate representation of IAC in the system by cycling through paired bubble interfaces properly.

The grouping of bubbles into size groups for bubble coalescence and breakup modeling is also a concern. In current signal processing algorithms, the chord length is used to separate bubbles into various size classes. However, the chord length does not accurately represent the size of individual bubbles, as shown in Figure 1.1. Using the chord length will always underestimate the actual size of the bubbles. To accurately represent the actual size of the bubbles, researchers should use the diameter of the bubble.

1.1. LITERATURE REVIEW

To understand the measurement principle used in calculating the IAC and VF, a review of the fundamentals to measure these parameters using probes is necessary. This section investigates the two-fluid model, interfacial transfer, the two-group interfacial area transport equations, measurement techniques, two-group classification, and current experiments.
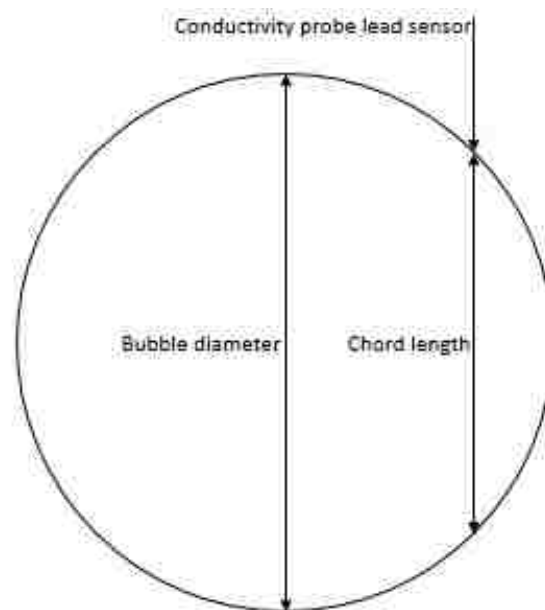
Figure 1.1. Diameter vs. Chord Length

1.1.1. Two-Fluid Model. In two-phase systems, one significant characteristic is the interaction between the individual phases. The interfaces play an important role in how the two-phases interact with one another. In a two-phase system, the shape and contours of the two-phase flows are continuously changing. To model two-phase flows, one can choose from two common methods based upon the mathematical treatment of the phases: the mixture formulation and the two-fluid formulation. In the mixture formulation, researchers blend the two phases together and treat them as a single phase. One advanced mixture

model is the drift-flux model (DFM). The DFM's point of focus is on the VF, the drift velocity, and the properties of the mixture. The DFM has become indispensable due to the simplicity of the model and its ability to predict the properties of the mixture in which the individual phases are strongly linked together [1]. However, for loosely coupled phases, the prediction performance in the DFM is not good enough. This deficiency is due to the major assumptions in the formulation. The DFM assumes that the motion in the system can be accurately articulated by the single mixture momentum equation. Again, the mixture momentum equation assumes that the kinematic constitutive relation can accurately describe the relative motion between the phases. This assumption is valid only when the two phases are strongly coupled together. This requires low acceleration to steady-state conditions or slow transients (i.e. without shocks). Ishii developed the two-fluid model in 1975 to overcome the limitation of the DFM, and Ishii and Mishima improved upon the process in 1984 [1, 4]. The two-fluid model contains the balance equations for continuity, momentum, and energy for each phase, coupled with the use of interaction terms and jump conditions. Ishii expressed the interaction terms through IAC and potential-driven fluxes [4].

Currently, researchers consider the two-fluid model to be the most accurate model for practical purposes due to the treatment of the individual phase interactions that occur at the interface. In the two-fluid model, since the macroscopic fields in two-phase flows are not independent of one another, time averaging leads to the need for constitutive relations for the interaction terms for the three balance equations [4,5]. The Eulerian time-averaged equation gives the balance equation for any quantity ψ, which for the two-fluid model is as follows [1]:

$$\frac{\partial \alpha_k \bar{\bar{\rho}}_k \bar{\psi}_k}{\partial t} + \nabla \cdot (\alpha_k \bar{\bar{\rho}}_k \bar{\psi}_k \bar{v}_k) + \nabla \cdot \alpha_k (\bar{J}_k + J_k^T) - \alpha_k \bar{\bar{\rho}}_k \bar{\phi}_k - I_k = 0 \qquad (3)$$

where I_k is the interfacial source term for the kth phase, which is expressed as;

$$I_k = -\frac{1}{\Delta t} \sum_j \frac{1}{v_{ni}} \{n_k \cdot [\rho_k(v_k - v_i)\psi_k + J_k]\} \qquad (4)$$

where the j and k subscripts are the jth interface and k^{th} phase, and T indicates the turbulent fluctuations. Also, α is the local time-averaged VF, ρ represents the fluid density, v is the velocity, ψ is the quantity being transported per unit mass, J is the generalized tensor efflux, and ϕ is the volumetric source/sink of ψ. Equation 4 articulates the interfacial transfer source in terms of a_i and driven flux. The time averaged a_i is;

$$\bar{a}_i^t = \frac{1}{\Delta t} \int_{[\Delta t]_{Tot}} a_i dt = \frac{1}{\Delta t} \sum_j \frac{1}{v_{ij} \cdot n} \qquad (5)$$

where the interfacial displacement velocity of the jth interface is $v_{ij} \cdot n$. The double over bar is the Eulerian time-average of the function F for the kth phase, as shown by Equation 5:

$$\bar{F}^t(x_0, t) = \lim_{\delta \to 0} \frac{1}{\Delta t} \int_{[\Delta t]_{Tot}} F_k(x_0, t) dt \qquad (6)$$

The phase average is defined by;

$$\bar{\bar{F}}_k = \frac{\bar{F}^t}{\alpha_k} \qquad (7)$$

The mass weighted mean is;

$$\bar{\psi}_k = \frac{\overline{\rho_k \psi_k}^t}{\overline{\rho_k}^t} = \frac{\sum_{k=1}^2 \overline{\rho_k}^t \bar{\psi}_k}{\sum_{k=1}^2 \overline{\rho_k}^t} \qquad (8)$$

Often the three-dimensional two-fluid model using temporal averaging is simplified into Equations 9, 10, and 11 [4,5]. However, the three equations are not

independent of each other and researchers must couple them. The terms represented by Γ_k and M_k in the balance equations are the mass transfer and interfacial force terms for the kth phase across the interfaces. IAC is key for predicting these terms.

Continuity equation:

$$\frac{\partial \alpha_k \rho_k}{\partial t} + \nabla \cdot (\alpha_k \rho_k \boldsymbol{v_k}) = \Gamma_k \tag{9}$$

Momentum equation:

$$\frac{\partial \alpha_k \rho_k \boldsymbol{v_k}}{\partial t} + \nabla \cdot (\alpha_k \rho_k \boldsymbol{v_k} \boldsymbol{v_k}) = -\alpha_k \nabla p_k + \nabla \cdot \alpha_k (\bar{\bar{\tau}} + \boldsymbol{\tau_k^t}) +$$

$$\alpha_k \rho_k g + \boldsymbol{v_{ki}} \Gamma_k + M_{ik} - \nabla \alpha_k \cdot \boldsymbol{\tau_i} \tag{10}$$

Enthalpy energy equation:

$$\frac{\partial \alpha_k \rho_k H_k}{\partial t} + \nabla \cdot (\alpha_k \rho_k H_k \boldsymbol{v_k}) = -\nabla \cdot \alpha_k (\bar{\bar{q}}_k + q_k^t) + \alpha_k \frac{D_k}{Dt} p_k +$$

$$H_{ki} \Gamma_k + a_i q_{ki}'' + \phi_k \tag{11}$$

The i in the subscript for the terms above denotes the values at the interfaces. The generalized interfacial drag is M_{ik}, interfacial mass transfer is Γ_k, interfacial shear stress is τ_i, viscous dissipation is ϕ_k, and interfacial heat flux is q_{ki}'' [1,4,5]. These interfacial transfer equations need to obey the balance laws at the interface. In addition, researchers can find equations for interfacial transfer conditions from local jump conditions, which are given in Equations 12-14 [1]:

$$\sum_k \Gamma_k = 0 \tag{12}$$

$$\sum_k M_{ik} = 0 \tag{13}$$

$$\sum_k (\Gamma_k H_{ki} + a_i q''_{ki}) = 0 \tag{14}$$

To resolve the two-fluid model, each variable requires a constitutive equation. For instance, the generalized drag force for the dispersed phase is modeled using Equation 15 [6,7,8]:

$$M_{id} = \frac{\alpha_d F_D}{B_d} + \frac{\alpha_d F_v}{B_d} + \frac{9}{2}\frac{\alpha_d}{r_d}\sqrt{\frac{\rho_c \mu_m}{\pi}} \int_t \frac{D_d}{D\xi}(v_d - v_c)\frac{d\xi}{\sqrt{t-\xi}} \tag{15}$$

In Equation 13, B_d represents volume of a standard dispersed fluid particle, F_D represents the standard drag force, μ_m is the mixture velocity, and F_v is the virtual mass force. The term furthest to the right in Equation 13 is the Basset force, which results from the change in velocity profile at the boundary layer. The first term expressed on the right side of Equation 15 can be written in terms of IAC [4,5]. Equation 16 therefore gives the standard drag force:

$$\frac{\alpha_d F_D}{B_d} = -a_i \left[\frac{C_D}{4}\left(\frac{r_{sm}}{r_D}\right)\frac{\rho_c v_r |v_r|}{2} \right] \tag{16}$$

Equation 16 specifies that the IAC and the drag coefficient are proportional to the drag force per unit area. In addition, by adding $\dot{m}_k$, which describes the mean interfacial mass flux, the source term for the mass continuity equation becomes $\Gamma_k = a_i \dot{m}_k$. Again, by applying the source term into Equation 14, it becomes;

$$\Gamma_k H_{ki} + a_i q''_{ki} = a_i[\dot{m}_k H_{ki} + h_{ki}(T_i - T_k)] \tag{17}$$

In Equation 17, q''_{ki} represents interfacial heat flux, which is used to model potential for energy transfer. Here, T_i is the temperature at the interface, h_{ki} is the interfacial heat transfer coefficient, and T_k is the bulk temperature from mean enthalpy. From Equations 1 to 17, the importance of a_i and how it is used in the two-fluid model are now apparent. To

be able to solve for a_i, a closure relation is necessary. The closure relation has led to researchers developing experimental correlations over time.

1.1.2. Interfacial Transfer. Particle size has been important to the transfer of mass and heat in a system. Earlier studies conducted by Calderbank and Moo-young showed on the effects of the interfacial area in gas-liquid dispersions [9]. Gal-Or and Hoelscher tested particle size distribution that affects the transfer of properties between phases in 1966 [10]. In 1967, Gal-Or and Walatka conducted a qualitative and quantitative analysis on a variety of parameters such as gas holdup, residence of phases, and average particle size on transfer rates. In previous studies, particle size was important to the transfer of properties between phases [11]. In 1980, Ishii and Mishima disclosed that small particles and their size are very important parameters in determining IAC [4,6].

In various flow regimes, three essential aspects for prediction of particle size are the maximum stable bubble size, bubble breakup and coalescence mechanisms, and (for boiling flows) nucleation sites. Figure 1.2a contains bubble flow at approximately 0.001 m/s in a bubble column. As the bubbles increase in size, the individual bubbles will start to distort. The distortion will change the surface area of the individual bubbles and therefore the IAC. As the bubbles make contact with one another and a rupture of the film layer occurs, the bubbles will coalesce. As shown in Figure 1.2b, at 0.8 m/s in a bubble column, it can be challenging to determine what is happening in the flow. However, in Figure 1.2b, there are much larger bubbles. These bubbles will cause break-up and coalescence to occur more frequently because of their size and turbulent eddies. The ability to anticipate IAC in the different flow regimes requires transport equations. Ishii and

Kojasoy conducted a study in 1993, which Kocamustafaogullari and Ishii continued in 1995 [12,13].

a.   b.

Figure 1.2. Bubbly Flow (a) and Churn Flow (b)

In Ishii and Kojasoy's study, they discovered that a key foundation for solving IAC is the particle number density. They derived the fluid particle number density transport equation by taking into account fluid particles entering and leaving a control volume, as shown by Equation 18:

$$\frac{\partial f(x,V,t)}{\partial t} + \nabla \cdot \left(f(x,V,t)v_p(x,V,t) \right) = \sum_j S_j(x,V,t) + S_{ph}(x,V,t) \quad (18)$$

In Equation 17, t represents a given time and $f(x,V,t)$ represents the particle density distribution function. The position is specified by x with a particle volume of V. The variable $v_p(x,V,t)$ represents the local particle velocity. The first term on the right side of Equation 17 is the net rate of change in the function from fluid particle interactions. The second term on the right side is the fluid particle source. However, Equation 19 is not appropriate for most two-phase studies that focus on averaged fluid particle behavior.

Later, Ishii and Kojasoy integrated over particle volume and applied the Leibnitz rule for integration and formed the bubble number density equation, Equation 19 [8,12].

$$\frac{\partial n}{\partial t} + \nabla \cdot n v_{pm} = \int_{v_{min}}^{v_{max}} \sum_j S_j(x, V, t)dV + \int_{v_{min}}^{v_{max}} S_{ph}dV \tag{19}$$

where n is the total number of particles. By multiplying Equation 20 with the average IAC of the particle volume and integrating over the volume, Ishii and Kojasoy obtained the interfacial area transport equation (IATE) as shown in Equation 20 [8,12]:

$$\frac{\partial a_i}{\partial t} + \nabla \cdot a_i \boldsymbol{v_i} = \sum_j \phi_j + \phi_{ph} \tag{20}$$

where a_i represents the average IAC of all fluid particles in the system, v_i represents the interfacial velocity, ϕ_j is the rate of change in the IAC from particle breakup and coalescence, and ϕ_{ph} represents the rate of change in the IAC from particle creation and destruction due to nucleation and condensation. In two-phase flows, the models for interaction between phases dates to the 1870s from studies about jet instabilities [14]. The studies conducted about particle interaction phenomena are important due to the strong coupling with the dynamics of the flow of the system. Some of the important studies include Jackson, Calderbank, and Hogarth [15,16,17]. They hypothesized that for coalescence to occur, a two-step process is necessary: 1. Drainage of liquid film between the bubble surfaces, and 2. A rupture of the film. Some of the key phenomena for coalescence include fluid particle collision from turbulent eddies, collisions due to different particle sizes and velocities, and collisions from partial interaction due to the wake of different particles. Figure 1.3 shows the various physical phenomena for coalescence mechanisms. Figure 1.3a shows that as the eddies form inside of the flow area, the bubbles

film layer will be disrupted and therefore combine. Figure 1.3b shows that collisions of bubbles will occur inside of the flow area. The varying sizes will cause the bubbles to have different velocities. The different velocities will cause the bubbles to press next to each. In addition, some breakup mechanisms include breakup due to turbulent eddies, surface instability at the interface of large particles, and laminar shear in viscous fluids. Figure 1.4 shows a few breakup mechanisms. Figure 1.4b shows break-up due to turbulent eddies. As the turbulent eddies hit the larger bubbles, the inertia from the impact of the eddies will cause the bubbles to break apart and form smaller bubbles.

a.   b.   c.
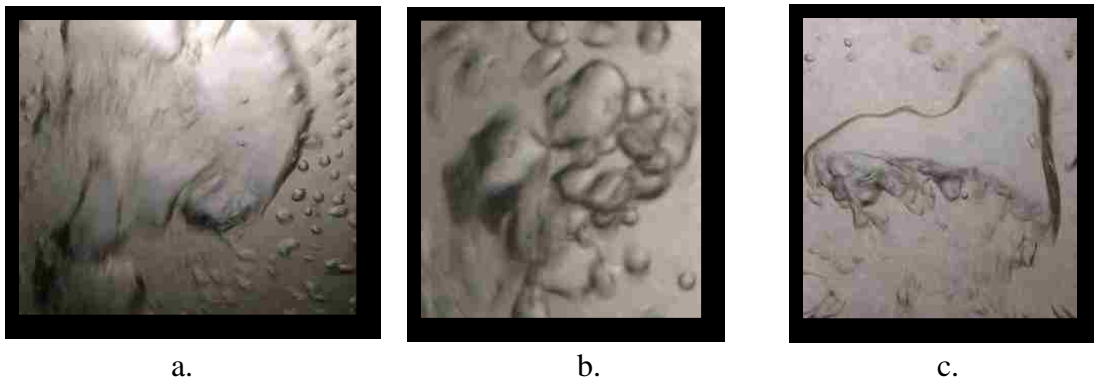
Figure 1.3. Coalescence Phenomena from Turbulent Eddies (a), Particle Size (b), and Wake Entrainment (c)

Figure 1.4b shows breakup due to surface instability. When a bubble increases in size, the bubbles will distort. When the distortions are large enough, the bubbles will break apart to form smaller bubbles. other and coalesce. Figure 1.3c shows that smaller bubbles will combine with larger bubbles due to the wake that is formed by larger bubbles.

a.   b.

Figure 1.4. Breakup Due to Impact From Turbulent Eddies (a) and Size (b)

For breakup due to turbulent impact, studies were conducted by Taylor, Kolmogorov, Batchelor, and Hinze [18-21]. They showed that breakup from turbulent impact occurs when the inertia of turbulent eddies overcomes the surface tension at the interface, causing the fluid particle to break. When a bubble increases in volume, an additional phenomenon occurs: surface instability at the interface of large particles. The size breakup mechanisms were examined by Thomason and colleagues and Wegener and colleagues [22,23].

1.1.3. Two-Group Interfacial Area Transport Equations. The IATE was proposed by Kocamustafaogullari and Ishii in 1995 [13]. The IATE is used to model the IAC in a system. The IATE uses bubble classification to separate individual bubbles based on the bubbles' properties to improve the predicted accuracy. After the proposition of the IATE, Wu proposed a one-group formulation to specify a system [14]. The one-group model is shown in equation 21:

$$\frac{\partial a_i}{\partial t} + \nabla \cdot (a_i \overrightarrow{v_{in}}) = \frac{2}{3}\left(\frac{a_i}{\alpha_g}\right)\left(\frac{\partial \alpha_g}{\partial t} + \nabla \cdot \left(\alpha_g \overrightarrow{v_g}\right) - \eta_{ph}\right) + \sum_j \phi_j + \phi_{ph} \quad (21)$$

$\frac{2}{3}\left(\frac{a_i}{\alpha_g}\right)\left(\frac{\partial \alpha_g}{\partial t} + \nabla \cdot \left(\alpha_g \overrightarrow{v_g}\right) - \eta_{ph}\right)$ is the volume expansion of bubbles from the pressure

changes in the system. $\sum_j \phi_j$ is the source or sink term due to bubble interaction

mechanisms in the system. ϕ_{ph} represents the phase change from evaporation or

condensation. $\frac{\partial a_i}{\partial t}$ is the time rate of change of IAC, and $\nabla \cdot \left(a_i \overrightarrow{v_{in}}\right)$ is the convection of

IAC. In the one-group IATE, there are many issues dealing with the large spectrum of

bubbles in the system. The large spectrum of bubbles contains a variety of drag coefficients

and interaction mechanisms that affect the properties of the system. The variety of bubbles

in the system led to inaccuracy when calculating the IAC. Therefore, the one-group

formulation is inaccurate when dealing with many flow regimes. The one-group model

bubbles should be spherical in shape, which only works for bubbly flows.

These shortcomings led Hibiki and Ishii to propose the two-group model [24]. Ishii

and Kim published the two-group IATE in 2003 [25]. Expanding the IATE model for two

groups is shown in Equations 22 and 23:

$$\frac{\partial a_{i1}}{\partial t} + \nabla \cdot \left(a_{i1} \overrightarrow{v_{in1}}\right) = \frac{2}{3}\left(\frac{a_{i1}}{\alpha_1}\right)\left(\frac{\partial \alpha_1}{\partial t} + \nabla \cdot \left(\alpha_1 \overrightarrow{v_{g1}}\right) - \eta_{ph}\right)$$

$$-C\left(\frac{D_c}{D_{sm\,1}}\right)^3 \left(\frac{a_{i1}}{\alpha_1}\right)\left(\frac{\partial \alpha_1}{\partial t} + \nabla \cdot \left(\alpha_1 \overrightarrow{v_{g1}}\right) - \eta_{ph}\right) + \sum_j \phi_{j1} + \phi_{ph\,1}$$

(22)

$$\frac{\partial a_{i2}}{\partial t} + \nabla \cdot \left(a_{i2} \overrightarrow{v_{in2}}\right) = \frac{2}{3}\left(\frac{a_{i2}}{\alpha_2}\right)\left(\frac{\partial \alpha_2}{\partial t} + \nabla \cdot \left(\alpha_2 \overrightarrow{v_{g2}}\right)\right)$$

$$+C\left(\frac{D_c}{D_{sm\,1}}\right)^3 \left(\frac{a_{i1}}{\alpha_1}\right)\left(\frac{\partial \alpha_1}{\partial t} + \nabla \cdot \left(\alpha_1 \overrightarrow{v_{g1}}\right) - \eta_{ph}\right) + \sum_j \phi_{j2}$$

(23)

Equation 22 shows one-group IATE, whereas equation 23 shows the two-group IATE. The two-group model separates the bubbles into two distinct groups. Group one contains spherical and distorted bubbles, and group two contains irregularly shaped bubbles, such as cap and slug or churn-turbulent bubbles, as shown in Figure 1.5.
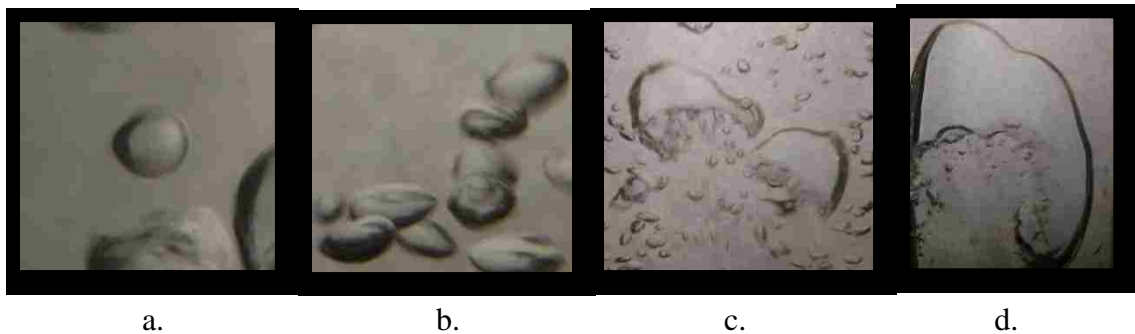
Figure 1.5. Spherical (a), Distorted (b), Cap (c), and Churn-Turbulent Bubbles (d)

1.1.4. Measurement Techniques. Multiple methods have been proposed for measuring IAC and VF. Some of the popular methods are chemical absorption techniques, the optical approach using light attenuation, photographic methods, wire mesh, and conductivity probes. In the chemical engineering field, most researchers prefer the chemical method [26,27]. In the chemical method, a system of fast pseudo-first-order reactions are used to calculate the IAC. The chemical method finds its origins in the gas absorption theory [28-31]. Gas-liquid reactions contain eight regimes classified on the characteristics of chemical reactions along with the concentration profiles of the specific reactants in the liquid. A common chemical method uses a NaOH(KOH) solution-CO_2 system due to its easy handling and analysis. However, there is a large error in the method

due to the dependency on the fluid properties, choice of chemicals, and the geometry of the flow channel. The chemical method has additional problems when the two-phase flow is not in steady state conditions because a large amount of time is required to obtain the necessary information.

Another method to calculate IAC is the photographic method. In the photographic method, researchers obtain the IAC by finding the average diameter and VF of the dispersed phase. The photographic method requires an image analysis of collected data. In the photographic method, the researcher must physically identify and measure the properties of the individual bubbles, but it requires a clear and flat channel to record the size of the individual bubbles as they flow through the test section. Moreover, this measurement technique is limited to bubbly flow and requires high CPU or computational time for test data analysis [32,33]. If large concentrations of bubbles are within the test area, the size is indeterminable. In addition, the diameter of each bubble requires calculation, leading to a time-consuming process for each experiment.

Prasser first described the wire mesh sensor (WMS) in 1998 [34]. In the WMS, two perpendicular arrays of electrodes form a grid that senses the conductivity from each of the nodes in the sensor. The liquid in the system has a higher electrical conductivity than the gas phase. The conductivity recorded by the WMS indicates whether gas or liquid is present at each node, leading to a distribution of gas and liquid phases collected from the sensor. Zhang tested the WMS, which yielded reasonable results for higher VF and high-resolution images of larger bubbles, but it does not work reliably for a lower VF where the average bubble size is smaller than the instrument resolution [35]. The WMS normally delivers fairly accurate estimates for VF and the interfacial velocity. However, the wire

diameter and spacing typically introduces a 4-10% error due to blockage of the cross-sectional area of the channel [36]. Prasser and Hafeli conducted WMS experiments in idealized bubbly flow conditions. They concluded that WMS overestimated the bubble size due to linear dependency and negative values of the local instantaneous gas fraction. Researchers will need further investigation into the WMS method in bubbly flow conditions [37].

The optical probe method uses light attenuation to acquire the area-averaged IAC and VF based on the intensity of scattered light. The light picked up by the sensor is then converted into a voltage to represent the liquid and gas phases [38]. The optical probe method is much easier and less time-consuming when compared to the chemical method or the photographic method. The major drawback to optical probes is that the system has a large upfront cost for implementation.

Neal and Bankoff first proposed the electrical conductivity probe, also called the electrical resistivity probe, in 1963 to measure local parameters [39]. The conductivity probe uses the difference in conductivity between the gas phase and the liquid phase to produce a change in voltage when a bubble encounters the tip of a sensor. The percentage of the time a single sensor in the conductivity probe is exposed to the gas phase determines the time-averaged local VF. Delhaye and Achard demonstrated that they could calculate interfacial velocity with multi-sensor conductivity probes, and therefore calculate IAC [40].

Both optical and conductivity probes are used in similar ways to calculate the IAC in a system. In both methods, the data acquisition system receives a voltage from all sensors of the probe. The major difference is the response time of the probes. The optical probe is

almost instantaneous when detecting the front and rear interface, whereas the conductivity probe has a rise and fall time for each sensor, as shown in Figure 1.6.

a.   b.
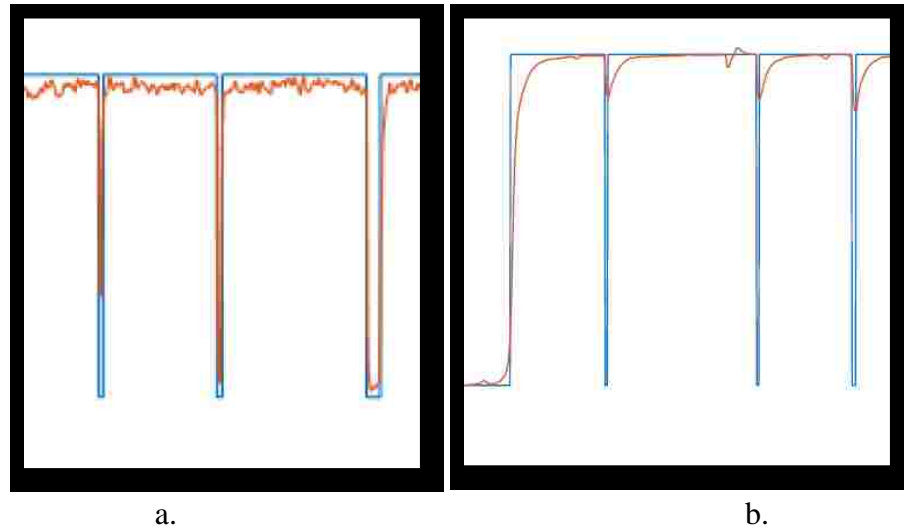
Figure 1.6. Differences in Signal Quality Between Optical Probes (a) and Conductivity Probes (b)

The faster response time of the signal allows for more accurate detection of the front and rear interfaces of the bubbles using optical probes. Since both methods have an associated voltage, they can be processed through the same algorithm and compared to ensure the accuracy of each method. Details discussions on both optical and conductivity probes are available in Sections 2.1.1 and 2.1.2.

1.1.5. Two-Group Classification. After calculating IAC, the measured bubbles are categorized into groups to ensure accuracy. The categorization is important to make corrections in the data and for model validation. In the two-group IATE model, the change in IAC can be dynamically predicted. However, the prediction accuracy of IAC in a system is dependent upon the experimental results obtained from measurement techniques. The

IATE allows the assessment of the transport phenomenon for each bubble group when variations in bubble size and relative velocity exist. Bubble groups are also necessary due to missing bubbles in a system. Missing bubbles are bubbles that may miss one or more of the four sensors, and therefore IAC cannot be calculated for the individual bubble. Since all bubbles do not hit all sensors every time, the missing bubbles still need to be counted. The missing bubbles are identified by the velocity formed by the lead sensor to determine the size of the bubble and the group they will be categorized into.

One of the models used to determine how to classify the bubble groups is the multiple-size-group model (MUSIG), which Lo created in 1996 [41]. In the MUSIG model, researchers organized the bubbles into many groups based on bubble size to improve the accuracy of breakup and coalescence prediction. There are two commonly used MUSIG models: the homogeneous MUSIG and inhomogeneous MUSIG. The homogeneous MUSIG model divides the dispersed phase of the system into N groups. Then, researchers calculate the one momentum equation for all groups of bubbles in the system, assuming all bubbles have the same velocity. However, the homogeneous model was shown to have many limitations due to the assumption that the slip velocities are independent of bubble size. In the inhomogeneous MUSIG model, researchers separate the dispersed phase into groups based upon the velocities associated with the N groups and solve multiple momentum equations for the dispersed phase. This improves accuracy at the cost of computational time.

Typically, either a four- or two-group method is used to classify bubbles. In the four-group approach, researchers group bubbles into spherical, distorted, cap, and slug bubbles. In the data processing algorithm to classify bubbles, it is necessary to obtain the

velocity of each bubble in the system. The bubble velocity is directly related to the chord length of the bubbles. In the past, determining the chord length of the bubbles has been the main method for grouping bubbles. Here, the type of bubbles can be determined by assuming the chord length is the diameter of the bubble.

To estimate the missing bubbles in the system, a correction is used for each group. In the case of group two, there is a higher likelihood that the larger bubbles will hit all sensors, while in group one, the smaller bubbles are more likely to miss at least one sensor. The major problem with technique is that the chord length is smaller than the bubble diameter, as shown in Figure 2.1. It can cause inaccurate classification of bubbles and therefore affects the IAC estimation for missing bubbles in the system. All missing bubbles in the system are separated into the groups associated with its velocity. Later, the effective bubbles, IAC results are used to calculate the average IAC for each group. The average IAC in a group is then multiplied by a factor created by the missing bubble to form the final IAC, as shown in equation 24:

$$a_i^t = \frac{N_{sph}}{N_{sph} - N_{miss\_sph}} [\bar{a}_i] \tag{24}$$

Wu and Ishii helped to predict a more accurate IAC and developed Equation 25 to improve the accuracy of groups:

$$a_i^t = \frac{N_{sph}}{N_{sph} - N_{miss\_sph}} \left[2 + \left(\frac{\sigma_{vz}}{\bar{v}_z} \right)^{2.25} \right] \langle \frac{1}{v_z} \rangle \tag{25}$$

Both Equations 24 and 25 are dependent upon the bubble groups and missing bubbles in the system.

1.2. OBJECTIVE

The main objective of this study is to improve the measurement accuracy of the four-sensor conductivity probe. The improvements that the current study will confirm are as follows:

1. Develop a more robust signal processing algorithm to reduce uncertainty in bubble interface identification

2. Improve the pairing process to reduce incorrect pairing of signals by implementing a double check to already paired bubble interfaces

3. Implement a new algorithm to categorize bubbles based on bubble diameter rather than chord length to improve bubble grouping accuracy

4. Evaluate the differences between optical and conductivity probes under high VF conditions and make recommendations for the use of each probe design

The desired objectives can be achievable by accomplishing the following tasks. First, a comparison of the raw signal with the logic pulse after signal conditioning of bubble interfaces to determine the size and location of bubbles. Second, a reduction in VF should occur from additional interfaces being discovered. Third, a shift in the calculated length of bubbles due to bubble diameter should be found. Fourth, the optical and conductivity probes should give similar results, signifying correct interface location. If all the objectives are met, the anticipated results when comparing the new and old algorithm should fall within the anticipated accuracy of 10% for IAC and VF.

2. METHODS

The methods section will include probe measuring techniques, signal processing algorithms, and improvements implemented into the algorithm. The first step to calculate the IAC and VF is to choose a measurement technique for observing the two-phase flow. The current study will discuss two measurement methods: the optical probe method and the conductivity probe method. In both methods, the probe output is the voltage signal. Output voltage amplitude changes due to the changes in the test fluid phase. Once the voltage change is measured, the processing is the same for both cases. After collecting the measured data from the sensors, an algorithm analyzes the signal to determine the IAC and VF. The algorithm first conditions the signal to find the front and rear interfaces of individual bubbles. Then, the algorithm pairs the individual signals together to find the common bubble interface. Next, bubbles are separated into groups to calculate IAC and VF for each group. Finally, the algorithm outputs the IAC and VF for each group.

2.1. PROBE MEASUREMENT TECHNIQUES

The conductivity and optical probes use different techniques, but both produce a voltage change that researchers can process using the same algorithm. Therefore, the results should be similar if the conditions remain consistent.

2.1.1. Conductivity Probes. In 1963, Neal and Bankoff found that while rigorous research on gas-liquid mixtures exists, details regarding the internal structure of the flow are still unknown. This lack of detail stemmed from a lack of appropriate instrumentation for performing precise measurements at various locations within the flow field. The parameters at specific radial locations that researchers deemed necessary to create precise

measurement included the local volumetric gas fraction, bubble frequency, and local bubble size distribution. Neal examined how the parameters were measured in attenuation of gamma rays and beta rays, radioactive tracers, and photographic records. He discovered that previous methods only calculated the parameters over a cross-sectional area and had errors up to 93%. Therefore, Neal proposed the use of the conductivity probe to measure local parameters. The concept behind the conductivity probe is that when a sensor is submerged in water, it makes contact with a bubble and a change in conductivity occurs. When a sensor meets a bubble interface, there will be a rise in the voltage of signal because of the difference in conductivity. If an immediate change occurs, then the sensors will produce a logic pulse for each one, as shown in Figure 2.1. The signals will be separated by the time it takes for a bubble interface to hit the next sensor, called the time delay. Complications can occur in conductivity probes due to the rise and fall of the voltage in the sensor and film from a bubble. For a conductivity probe, the process of penetrating a bubble can lead to a larger rise or fall time in the signal. The larger rise and fall time in the signal can introduce errors when the signal is conditioned.

After Neal proposed the idea of the conductivity probe to measure local parameters, Delhaye and Achard ran tests to determine if they could calculate IAC [40]. In 1984 and 1986, Kataoka and Ishii developed a method to calculate IAC for different types of bubbles and began using the conductivity probe to measure IAC [42,43]. In 1990, Kataoka and Serizawa stated that IAC in bubbly flow is directly related to the bubble diameter. They showed potential applications of using multi-sensor probes to calculate the IAC in two-phase bubbly flow systems [44]. In 1991 and 1992, Ishii and Revenkar reported their use of the four-sensor conductivity probe [2,45]. They recorded the theoretical profiles of the

VF and IAC using pictures of cap bubbles. The profiles and calculations from using the four-sensor conductivity probe were considered reasonable from their tests.
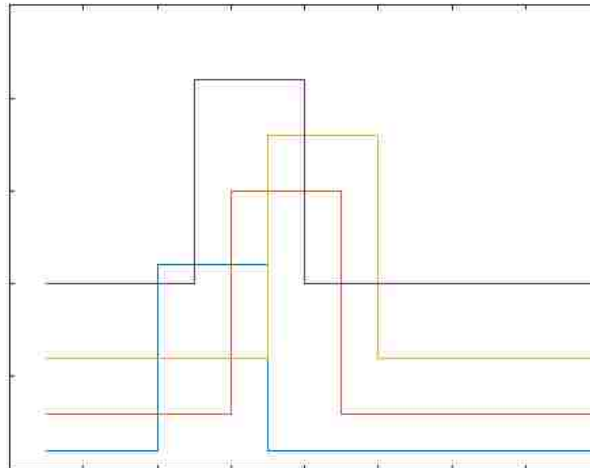
Figure 2.1. Logic Pulse for All Four Sensors

Some limitations exist in previous designs of the four-sensor conductivity probe. The limitations occur because of size and geometric configurations of the individual probes. Kataoka, Ishii, and Serizawa determined that the size of the individual probes caused the bubbles to deform between the probes, leading to inaccurate measurements [46]. The limitations and inaccurate measurements from previous two- and four-probe sensor methods led to the development of the miniaturized four-sensor conductivity probe. Kim and his colleagues developed the miniaturized four-sensor conductivity probe and a signal processing scheme that would work with the new probe [47]. The miniaturized conductivity probes they created had a thickness of 0.2 mm, allowing each sensor to be close to one another, as shown in Figure 2.2. The researchers ultimately tapered the sensors in the four-sensor miniaturized conductivity probe to allow the sensors to penetrate the

bubbles. The miniaturized four-sensor conductivity probe was benchmarked in the following few years to determine its validity.

Figure 2.2. Miniaturized Conductivity Probe

During Kim's experimental validation in 1999, he tested a variety of flow regimes with different types of bubbles. Kim's concern with the miniaturized probe was with the error in the Taylor bubble chord-length and the actual contour of the bubble's front and rear interfaces. In 2001, Kim tested bubbly flow in round pipes, and the data showed an error of approximately ±10%. Deviations in the data were from locations near the bubbly to cap-bubbly transitions [3]. In 2001, experiments using local values of slug flowed averaged over the cross-sectional area of the channel produced errors that were within ±10% of the anticipated values [48]. Ishii, Kim, and Uhle conducted benchmarking experiments for adiabatic air-water bubbly flow [49]. They experimented with round tubes of three different flow areas. The model data matched with the experimental data, presenting an error of ±10%. In 2015, Ishii and his colleagues used round pipes with the four-sensor conductivity probe at different axial locations in the bubbly flow [50]. The database consisted of about 2,000 time-averaged local measurements. They benchmarked

the conditions from the data within ±10% of the anticipated value, reaffirming the reliability of the data.

The two common conductivity probes used are the two- and four-sensor probes. The two-sensor conductivity probe assumes that all bubbles in the flow are spherical. Researchers use the four-sensor conductivity probe in flows where bubbles are not spherical.

When researchers calculate properties in two-phase flows, the total IAC and the total VF are normally under consideration. However, there is a lack of information about the accuracy of bubbles in individual groups. In 2014, to improve the accuracy of the groups, Shen and Nakamura developed a mathematical formulation to calculate the instantaneous velocity using the four-sensor conductivity probe. The algorithm uses the instantaneous interfacial normal unit vector and the local instantaneous three-dimensional interfacial displacement velocity vector for calculations. Shen's study, classified the bubbles into spherical bubbles and non-spherical bubbles [51]. The method used to separate the spherical bubbles in Shen's method is the bubble deviation coefficient from spherical shapes called the aspheric shape factor, as shown in Equation 26:

$$C_{dv} = \frac{|a_{i,2h} - a_{i,2h+1}|}{a_{i,2h} + a_{i,2h+1}} = \frac{\left| |\cos\theta_{i,2h}| - |\cos\theta_{i,2h+1}| \right|}{|\cos\theta_{i,2h}| + |\cos\theta_{i,2h+1}|} \tag{26}$$

Where C_{dv} is the asymmetrical degree found from the two interfacial normal vectors due to the shape deviation form a sphere on the 2h and 2h + 1 interfaces. If $a_{i,2h} = a_{i,2h+1}$ C_{dv} becomes zero for spherical bubbles and when bubbles are slightly deformed, C_{dv} is greater than zero. In this study, C_{dv} will vary between 0 and 1 due to the shape change for the bubble. The algorithm is practical and reliable for various multi-dimensional

two-phase flows with error bars of ±4.6% and ±14.0% for the bubble diameter and IAC, respectively. It will be necessary to conduct additional experiments before researchers can evaluate the accuracy of the method for classifying bubbles based on size.

2.1.2. Optical Probes. Another way to measure local parameters is the optical probe. Miller, Mitchie, and Delhaye presented and defined the optical probe processes and principles in 1969, 1970, and 1971 [52,53,54]. Delhaye and Jones summarized the processes for using optical probes in 1976 [55]. Galaup and his colleagues in 1976 and Abuaf and his colleagues in 1978 were some of the first research groups that used optical probes to measure local parameters [56,57]. In these experiments, the researchers established that they could measure the local VF and interfacial velocity in two-phase flows when using the optical probes. From Abuaf's test, many of the experiments for bubble velocities between 0.7 cm/s to 280 cm/s showed an accuracy of 1%. Frijlink developed the first four-sensor optical fiber probe in 1987, which Xue advanced in 2003 [58,59].

Optical probes have a similar configuration to conductivity probes. The difference between optical probes and conductivity probes are the tips of the individual probes. Manufacturers fashion optical probes from optical fibers instead of a conductive material. An optical fiber probe is shown in Figure 2.3. The optical fiber probe in this study is a light-reflection probe. A light-reflection probe builds upon the principle that as a bubble passes over the tip, light will reflect at the tip of the probe, and this reflection will turn into a signal. Researchers commonly use light-reflection probes because they are smaller and more accurate than light-transmitted optical fiber probes [57]. The light reflection optical fiber probe principle is based on Snell's law. At the tip of the probe, the light will either refract or reflect, depending upon the surrounding environment. The amount of light the

process attenuates and scatters in the mixture of phases results in the change of the optical properties. The change in the optical properties will result in the distinction between gas and liquid in the system.

Figure 2.3. Optical Fiber Probe

In a light reflection optical fiber probe, light rays are reflected if the index of refraction, n, is less than 1.15, and they are refracted if it is less than 1.15, as shown in Figure 2.4. When an optical fiber probe reflects light, the probe is in the gas phase. When the light is refracted, the probe is in the liquid phase. When the optical fiber probe is not in contact with the liquid film on the tip of the sensor, the resulting anomaly reduces the effectiveness of the conductivity probe. However, the anomaly of the film does not reduce the effectiveness of the optical probe [58]. In 1997, Farag and his colleagues used turbulent fluidized beds to find the dynamic properties of the liquid phase [60]. In Farag's study, he found that using the fiber optic probe would sometimes inaccurately measure the VF. The underestimation of bubbles in the study was most likely due to smaller bubbles. In 2015, Tian created a model for bubble velocity in upward and downward bubbly flows by using a four-sensor optical probe. The comparison between the area-averaged VF and bubble

velocity was within 15% under various conditions for the optical sensor compared to the photographic method [61].
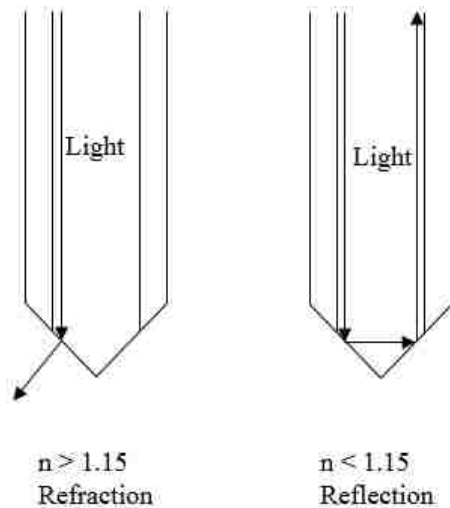
Figure 2.4. Refraction and Reflection of an Optical Fiber Probe

2.2. BUBBLE COLUMN

Tests conducted by Ishii and Kim in 2001, when the miniaturized four-sensor conductivity probes were first developed, worked with two-phase flows with superficial gas and liquid velocity [3]. These studies were conducted with local bubble velocities between 0.47 m/s and 6.09 m/s.

Researchers conduct experiments in bubble columns for a multitude of reasons due to their desirable qualities for testing different applications, such as high thermal stability, heat and mass transfer properties, low cost and maintenance, and a solid design without any moving parts [63]. In the field of chemical engineering, researchers use bubble column reactors to produce fuel, like sulfur-free diesel fuel, from dimethyl ether, bioethanol processes, and the Fischer-Tropsch process [63,64]. In 2009, Youssef and Al-Dahhan used

a bubble column to represent heat exchanging tubes for methanol synthesis [65]. In 2015, Kagumba and Al-Dahhan used bubble columns to test the diameter of tubes when designing heat exchangers [64]. In some operating conditions, including higher flow rates, multiphase reactors may become complex and chaotic. Researchers use bubble columns to test the properties of two-phase mixtures in complex environments. In another test, researchers performed tests in bubble columns to benefit bioreactors when aerobic cultivations are present in this method. In these types of experiments, it is imperative use to a simpler technique to find parameters in the system [66].

Two-phase flows are present in many different fields. In light water reactors, a phase change from water to steam or vice versa forms the water-steam two-phase flow in various systems, such as reactor coolant system, steam generators, heat exchangers, and condensers. Properties of the two-phase mixtures are important when analyzing accident scenarios, such as a loss of coolant accident (LOCA), a steam generator tube rupture, or a main steam line break.

2.3. SIGNAL PROCESSING

The signal processing algorithm can be subdivided into four steps: signal conditioning, pairing, group separation, and calculations. This section gives an overview of the algorithm and discusses the process of each step, as illustrated in Figure 2.5.

2.3.1. Signal Conditioning. The signal conditioning algorithm is broken into six separate sections: noise removal, finding the maximum and minimum voltage, normalization, noise threshold, detection of the bubble interface, and conversion to a logic pulse and/or signal storing. From the use of the six signal conditioning steps, researchers can change the original signal into a discernible logic pulse [40,42,43,67].

In the noise removal portion of the smoothing algorithm, a filter is added to the signal and is implemented to produce a continuous slope for each of the bubbles. First, a moving median filter is applied remove the high-frequency noise that results from the surrounding environment. If researchers do not apply this step to the regime, the signal processing code might mistake the noise for the front or the rear interface of a bubble, which will lead to inaccurate measurements for the IAC and VF. The moving median filter is normally set above four points. It is important to choose a moving medial filter that will not compromise the collected data.
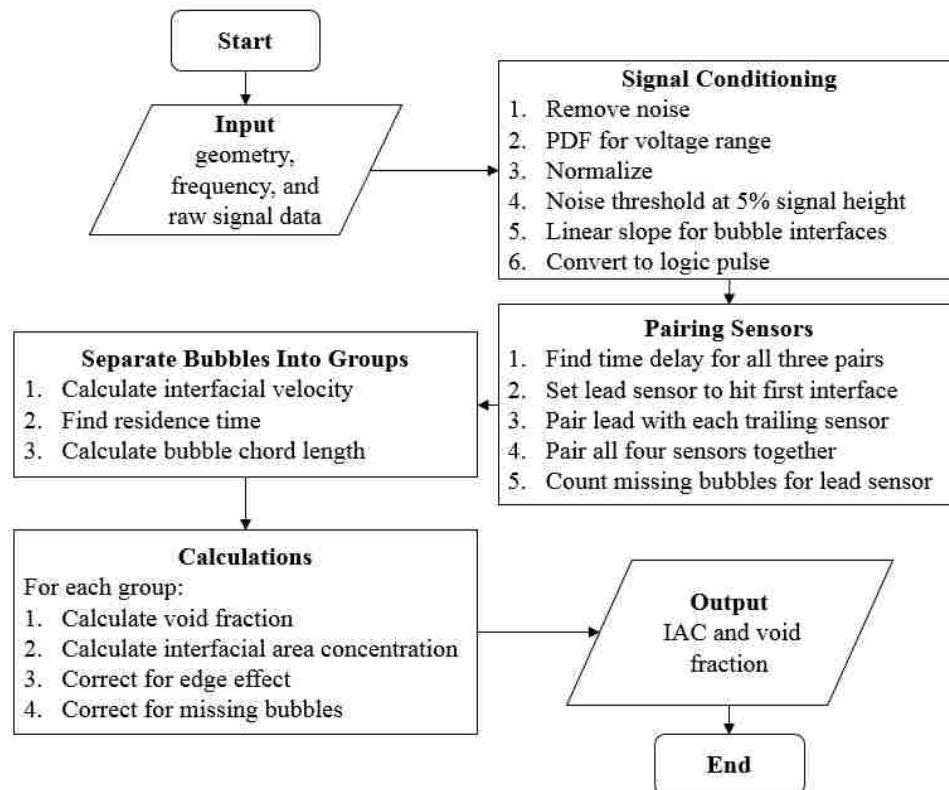
Figure 2.5. Algorithm to Calculate IAC and VF

After applying the moving median filter, researchers locate the maximum and minimum voltage in the system. The most important aspect to consider in the process is that sometimes an outlier can occur in the code. Any outliers can lead to large spikes in the signal and affect the normalization process. Once researchers find all the voltages in the system and remove the outliers, the signal is normalized.

Since every system will have a different voltage for each sensor, it is important for researchers to normalize the signal to ensure that they have completed the pairing process. After discovering the minimum and maximum voltage, the signal should normalize based on the respective maximum and minimum values. In Equation 4, V_i represents the voltage, V_{min} represents the minimum voltage, and V_{max} represents the maximum voltage:

$$V_{norm} = \frac{V_i - V_{min}}{V_{max} - V_{min}} \tag{27}$$

The voltage range is not important for calculating the local parameters. However, the lower region represents the liquid, and the upper region represents the gas. Therefore, regardless of the voltage each sensor collects, researchers should locate a common range. The common range allows the signal processing code to become independent of the voltage that the data acquisition system collects.

Once the signal is normalized, a noise threshold is applied to yield more reliable results. The noise thresholds are applied to the upper and lower boundaries of the voltage. Applying the threshold removes a large amount of noise that the sensor receives on the upper and lower bounds. The standard for the threshold is between 5% and 10% of the upper and lower portions of the signal. The algorithm allows one to modify the threshold depending upon the noise in the data acquisition within the system. Therefore, the threshold should exclude all noise from the upper and lower bound to increase the reliability of the

data. In the range of the two threshold values, the signal that researchers record is considered unreliable and should be excluded.

After applying the noise threshold, researchers will discover the bubble interface for each pulse. The signal for each case will have a rise and fall time associated with each interface, as shown in Figure 2.6. The rise and fall are due to the response time of the data acquisition system and the probe's intrusiveness in the system. As a bubble comes in contact with a sensor, it will deform. This phenomenon will cause a slight variation in the voltage of the system. To obtain the best location for each interface, researchers will need to implement a slope calculation for each peak.
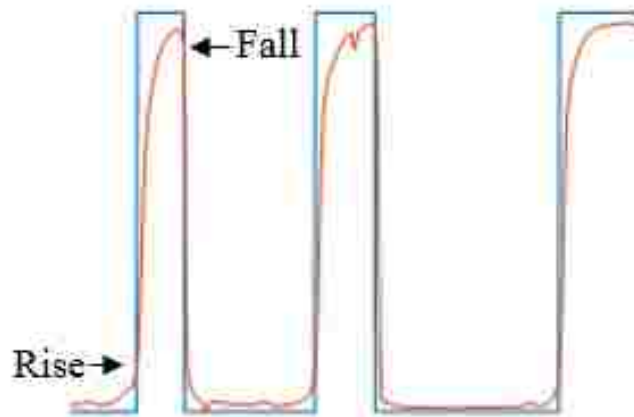
Figure 2.6. Rise and Fall of a Signal

The rise and fall time follows an exponential curve. However, 10-30% of the peak height is used find an acceptable position to determine the front and rear interfaces of the bubbles. The gradient is used to backtrack the signal to the actual interface and avoid fluctuations due to the sensor entering and leaving the interface.

After researchers discover the interface, they either store the signal or convert it to a logic pulse to check the position of the interface. The point in which the signal switches from the bottom to the top is the front interface, whereas the reverse is the rear interface. Using these parameters, researchers will divide the data points by the frequency to determine the residence time of each bubble.

2.3.2. Pairing Sensors. After the interfaces of all four sensors are found, they are paired together. The pairing process takes the lead sensor and one trailing sensor to determine if two signals are the same interface. Since the lead sensor is the longest, it should on average encounter a bubble first. To start, each of the lead sensor interface locations is set as a starting point. Then, a method to find the time delay for each sensor is determined. When a bubble encounters a sensor, it will have a chance to encounter the other three sensors. If the same bubble encounters another sensor, there will be a time delay between the two sensors. This time delay should be applied when pairing the two sensors to form a common interface. In a system where bubbles are moving at different velocities, there can be challenges when pairing the sensors together. The three common methods to pair the signals are the cross-correlation method, the DFM, and user-defined velocity. For each of the models, a reference velocity needs to be determined to determine the average bubble velocity for the system. The cross-correlation method uses a predefined period and measurement of similarity to find the time delay between two sensors. In the cross-correlation method within the allotted period, the transition points are compared to one another to find the most common delay between the lead sensor and each of the trailing sensors. The most common delay between the two sensors will determine the average time delay in the system. Since each bubble has an associated velocity, it is important to ensure

the bubbles are paired with the correct interface. In the DFM, the gas and liquid phase velocities are used to find the average time delay in the system, as shown in Equation 28 [1]:

$$v_{g\_DFM} = 1.2(j_g + j_f) + 0.25(1 - \alpha_g)^{1.25} \tag{28}$$

where j_g and j_f are the superficial gas and liquid velocities and α_g is the VF calculated from the lead sensor. In the user-defined bubble velocity, the user directly inserts a reference velocity to define the average velocity of the system. For all three cases to achieve correct pairing, two times the time delay is used to pair the signals. However, it is not a good estimate for all bubbles in the system. A cut-off at around 50% of the mean value is used to remove signals that are too close to one another. For signals that are too far apart, a cut-off at 95% of the max time delay is set to remove possible pairing. Then, all four sensors are paired together to find a common interface. The lead sensor is used to determine that all interfaces to be measured and missing bubbles are accounted for at this step.

2.3.3. Separation of Bubbles into Groups. After the bubbles are paired, they are categorized into four groups. The four bubble types most researchers choose are spherical, distorted, cap, and Taylor bubbles. The chord length information is used to categorize the groups. Effective grouping calculations are possible utilizing the four- and two-probe approach. When separating bubbles based upon types, researchers can distinguish IAC for each type of bubble separately. Ishii and Zuber have devised a method to separate each type of bubble by specific limits [6,68]. Equation 29 calculates the spherical bubble limit, and Equation 30 calculates the distorted limit, shown by:

$$D_{ds} = 4\sqrt{\frac{2\sigma}{g\Delta\rho}\left(\frac{\mu_f}{\left(\rho_f\sigma\sqrt{\frac{\sigma}{g\Delta\rho}}\right)^{\frac{1}{2}}}\right)^{\frac{1}{3}}}$$ (29)

$$D_{dmax} = 4\sqrt{\frac{\sigma}{g\Delta\rho}}$$ (30)

In Equations 29 and 30, σ is the surface tension between water and air, g is gravity, $\Delta\rho$ is the change in density between water and air, ρ_f is the fluid density, and μ_f is the dynamic viscosity of the fluid. Any bubbles that are smaller than Equation 29 are categorized as spherical. Bubbles that are larger than Equation 29 but smaller than Equation 30 are considered distorted. Slug bubbles are larger than the diameter of the pipe and their chord length is larger than the diameter of the pipe [22]. Cap bubbles are found between Equation 6 and the slug bubble criterion, which is the pipe diameter. For all research calculations, the chord length is used from the lead sensor since it will make the first contact with the bubble and therefore will be considered the most accurate. Researchers then use the chord length as the diameter for classifying the bubbles.

2.3.4. Defining IAC and VF. In a two-phase system, the four-sensor probe will intrude in the flow of the mixture. In an optimal situation, a bubble will flow upwards in the direction of the probe and hit the lead sensor followed by the three trailing sensors. If all four probes hit the probe in order, it is assumed that the bubble moves in an axial direction and the probe touches near the center of the bubble [58]. In cases where the bubble missed a sensor or the trailing sensors did not make contact shortly after, calculations register that the sensor pierced the bubble close to the side. In addition, researchers can

calculate the length of spherical bubbles from the two-sensor probe approach using the lead and a single trailing sensor.

After Kataoka formulated a method to determine the local time-averaged IAC, the probes were tested in different flow regimes [42,43]. Researchers only use the two-sensor conductivity probe for bubbly flow where all bubbles are assumed to be spherical. In a two-sensor probe, researchers assume all bubbles have the same probability of encountering the sensor at any location on the bubble's surface. For larger bubbles, a four-sensor probe is essential to ensure accurate results. The four-sensor probe can track distorted, cap, slug, and churn turbulent flow regimes. The four-sensor probe uses three two-sensor pair configurations to couple the lead sensors with the other three trailing sensors. Then, researchers determine the time-averaged VF by determining how long they exposed a single sensor to the gas phase. Ishii defines and presents the ability of the conductivity probe to obtain local time-averaged IAC through his work in Equation 31 [1]:

$$\bar{a}_i^t = \frac{1}{\Delta T} \sum_j \left(\frac{1}{|v_i \cdot n_i|} \right)_j \tag{31}$$

Equation 13 infers that if researchers obtain the bubble interfacial velocity, they can determine the local IAC. By using three two-sensor probes set to represent the x, y, and z axis, Kataoka, Ishii, and Serizawa determined the time-averaged IAC regardless of bubbles' shapes [42,43]. They assumed that there was a correlation between $\frac{1}{|v_{ij}|}$ and $\frac{1}{cos\phi}$ and thus suggested Equation 32 to calculate the problem:

$$\bar{a}_i^t(x_0, y_0, z_0) = 2N_t \overline{\frac{1}{|v_i|}} \cdot \overline{\frac{1}{cos\phi}} \tag{32}$$

Where:

$$\frac{1}{|v_\iota|} = \frac{\Sigma_j \frac{1}{|v_{ij}|}}{\Sigma_j} \text{ and } \frac{1}{cos\phi} = \frac{\Sigma_j \frac{1}{cos\phi_j}}{\Sigma_j} \tag{33}$$

In Equation 33, N_t represents the bubbles that pass by the location of measurement, and ϕ_j represents the angle from the jth interface and the interfacial velocity. In the two-sensor probe, researchers assume every part of a bubble has an equal probability to encounter the probe. Kataoka came up with the final form shown in Equation 34 [42,43]:

$$\bar{a}_i^t(x_0, y_0, z_0) = \frac{4N_t \left[\Sigma_j \frac{\frac{1}{|v_{szj}|}}{\Sigma_j} \right]}{1 - cot\frac{1}{2}\alpha_0 \, ln\left[cos\frac{1}{2}\alpha_0\right] - tan\frac{1}{2}\alpha_0 \, ln \, sin\frac{1}{2}\alpha_0} \tag{34}$$

In many two-phase systems, bubbles are not spherical. In these cases, the two-sensor probe cannot be used. To account for bubbles that are not spherical, the four-sensor probe is necessary. The four-sensor probe approach assumes three two-sensor pairs with a lead sensor that connects the three trailing sensors. When using three two-sensor probes, representing the x, y, and z axis, researchers can simplify the time-averaged IAC into Equation 35 [42,43]:

$$\bar{a}_i^t = \frac{1}{\Delta T} \sum_j \left[\left(\frac{1}{v_{s1j}}\right)^2 + \left(\frac{1}{v_{s2j}}\right)^2 + \left(\frac{1}{v_{s3j}}\right)^2 \right]^{1/2} \tag{35}$$

When using Equation 15, no hypothesis is necessary for the bubble shape when calculating IAC. $\bar{a}_i^t$ is the IAC for the dispersed phase that Kataoka and Ishii in 1994, Kim and his colleagues in 1998, and Wu and Ishii in 1999 improved upon in their respective research [23, 46, 69]. The improvements these researchers made are due to many

assumptions regarding the two-sensor probe. Some of these assumptions include the belief that all bubbles are spherical; there is no fluctuation in direction when a probe pierces a bubble, and any location of a bubble can encounter the probe. For the four-probe sensor, there are a few key considerations that researchers should keep in mind. The three considerations are when the size of a bubble is large compared to the distances of the sensors, when all four sensors pierce a bubble interface, and when the bubble is not significantly distorted. When researchers encounter these considerations, they may use the front and rear interfaces to calculate the IAC for bubbles that are not spherical. One important factor when calculating IAC for larger bubbles includes the distortion of the bubbles and how it affects the position of the interface. When calculating Taylor bubbles, one sensor will miss the interface near the wall of the measurement area due to a liquid film from the Taylor bubbles. When bubbles miss a sensor, IAC cannot be calculated due to inadequate information. Wu and Ishii attempted to correct the bubbles that the probes missed using a variety of tests [69]. Most corrections during testing required around 1,000 bubbles to obtain a statistical error of 7%.

2.3.5. Determining the Frequency. The data acquisition system samples the sensor voltage at a fixed sample rate. Researchers can miss bubbles that are small due to the response time or an insignificant number of sampling points. If the bubble velocity in a system is high, the system may require larger sampling frequencies to identify the bubbles in the system that are close to one another. The time in which the gas phase in an experiment is exposed to the sensor is directly related to the VF. If the sample rate causes small bubbles to miss, the accuracy of IAC and VF can come into question. If smaller bubbles are frequently missed, the time delay found in a signal connecting bubble

interfaces can lead to an inaccurate IAC. The sampling frequency is important for measuring with either the optical or conductivity probes. To see the effects of sample frequency, Worosz and his colleagues in 2016 studied 16 specific frequencies from 1 to 250 kHz [70]. Worosz's study, he normalized the frequencies based on the 250 kHz sampling. For most frequencies, the VF was within 5% of the anticipated value. However, he found for low gas velocities, such as 0.17 m/s, they had a stronger dependence on sampling frequency than higher gas velocities, such as 1.5 m/s. In the lower superficial gas velocities, the experiment was required to maintain a 5% accuracy, which showed in the study of the 250 kHz frequency sample. In most cases converged by 10 kHz and by 30 kHz, the VF was within the same level of agreement as the 250 kHz. The greatest requirement for increasing the sampling frequency deals with the minimum size of the individual bubble. In low superficial gas velocities, the bubbles are smaller, and therefore researchers can miss them if the frequency is not high enough.

To find the optimal frequency of the data acquisition system, researchers must consider the sample size and accuracy. To convert a signal into a numeric sequence, researchers will apply specific types of sampling to the system. According to Shannon, an adequate sample rate is the Nyquist rate in samples per second [71]. The Nyquist rate is two times the highest frequency in the system, which will allow the original signal to recover its original form [72]. Researchers consider the highest frequency that occurs in the system as the band limit. When the band limit in a system is too high, this can cause the signals to become indistinguishable from one another. To prevent the signal from becoming indistinguishable researchers can apply a low-pass filter before sampling. Finding the optimal sampling rate can be difficult because it will vary depending upon the

response of the actual method and how quickly the signal will vary. Only when at least two samples are collected within the frequency of the oscillation of the signal will the optimal sample rate be achieved. To use the linear slope approximation for 20% of the minimum peak, researchers must determine a minimum of five points. If the minimum peak height in the system that should be calculated is 10% of the signal height and it takes $100 \, \mu$s to obtain the data, the optimal frequency would be 10 kHz.

3. EXPERIMENTAL SETUP

For testing the signal processing algorithm an environment that will produce a two-phase mixture is necessary. In this study a bubble column will be used to produce this condition. The bubble column will be exposed to the air and the gas velocity will be controlled while both of the probes are inserted into the mixture. The multiple gas velocities will produce bubble flow a transition flow and two churn turbulent flows. Each flow will help validate the original algorithm and allow a comparison to the new algorithm.

3.1. SOFTWARE

The software used in this study to calculate the IAC and VF is the Matrix Laboratory (MATLAB). MATLAB is a proprietary programming language that allows for matrix manipulation, plotting of formulae, and implementation of algorithms into the interface with other popular programming languages including Formula Translation (FORTRAN). FORTRAN is one of the initial high-level programming languages. FORTRAN was designed to solve problems algebraically. FORTRAN in the past has been extensively used in the fields of mathematics, science, and engineering. Historically, researchers have used FORTRAN to handle data processing. While FORTRAN has served as a foundational tool for many years, technology has improved these types of tools to the point where FORTRAN is no longer the optimal coding choice and is not as commonly used as it once was.

3.2. EXPERIMENTAL PROBES

Experiments used in this study consisted of two different measurement techniques. The two types of probes are the four-sensor conductivity probe and the four-sensor optical probe. Each of the probes were designed and developed in the Thermal Hydraulics Experiment, Modeling, and Engineering Simulation (THEMES) laboratory for use in the bubble column. The next two sections will explain the creation and design of each probe type.

3.2.1. Conductivity Probe Design. The creation of the conductivity probe starts with four needles. Each of the individual needles are 40 mm long and 0.2 mm in thickness. The radial surface of the needles are scuffed to provide a surface for the coating to adhere. Next, the needles are dipped into EP19HT, an insulating coating, to ensure the individual needles will not encounter one another, disrupting the output of the signal. Once the four needles are coated, they are baked in an oven at 130°C for 1 hour and 15 minutes. This allows the coating to harden onto each of the needles. Then, each needle is dipped in water, and a multimeter is used to test if the coating was properly applied. A wire is attached to the back of the needle and soldered together, allowing for a solid connection. Once soldered, a heat shrink tube is applied to the individual needle to ensure the soldering will not be exposed to any unwanted stress. Next, the tip of each needle is abraded with a Dremel tool at an angle to remove the coating from the tip, allowing the edge to remain tempered. Each needle is placed into a ceramic tube to keep consistent spacing at the back end of the sensor. The needles represent each of the sensors in the probe.

Then, the sensor are spaced vertically with the lead sensor 1 mm longer than the three trailing sensors. Epoxy is applied to all the sensors against the ceramic tube to make

sure the vertical position is set in place and cured. Each of the sensors is spaced horizontally from one another, producing a tetrahedral shape with the lead sensor at the center. The four sensors are coated with epoxy approximately 1 mm from the tip of the shortest sensor to permanently keep consistent spacing. The stainless steel housing tube is cut approximately 60 mm from one end and bent to a 90° angle to allow the probe to be inserted into the bubble column port. The four wires attached to the sensors are fed through the stainless steel housing tube until only the sensors are exposed. Epoxy is then applied to connect the steel tube to the ceramic tube of the probe. Additional epoxy is applied to the 90° portion of the steel tube to ensure water will not enter an exposed portion of the sensor. A fitting is applied to the steel tube to seal the probe into the bubble column. A grounding wire is attached to the back end of the steel tube to complete the circuit. The probes are placed underneath a microscope, allowing the distances to be measured between the individual sensor tips, as shown in Figure 3.3.
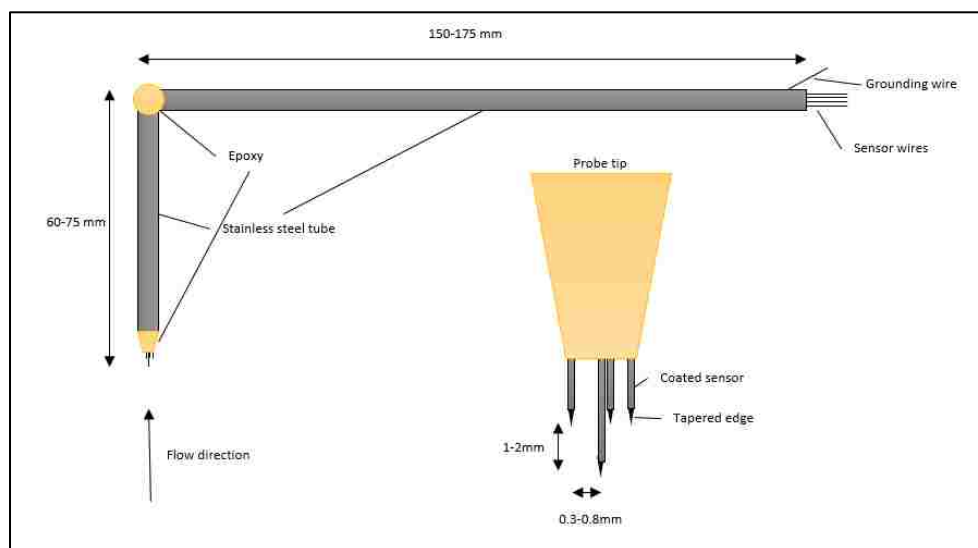
Figure 3.1. Conductivity Probe Layout

Figure 3.1 is a diagram of the conductivity probe design. The distances shown in Figure 3.1. will slightly vary between each probe while they are constructed. Figure 3.2 shows the final product of the design ready for insertion into the bubble column. The fitting at the end can be replaced with an actuator, allowing the radial positions to be measured.

Figure 3.2. Four-Sensor Conductivity Probe

a. b.

Figure 3.3. Probe Tip (a) and Probe Tip Under Microscope (b)

3.2.2. Optical Probe Design. The four-sensor optical fiber probe that is used for experimentation in this study is made of optical fibers. Each of the optical sensors is made from a quartz glass core 0.2 mm in diameter, a cladding 0.2 mm of silicon, and a Teflon protective layer 0.2 mm in diameter. The total outside diameter for each sensor is 0.6 mm. At the very tip of each sensor, the glass core may be uncovered by removing the cladding

and protective layer for 2 mm. The glass tip is formed into a round shape to ensure that the total internal reflection will occur when a bubble passes through any of the individual tips. The three trailing sensor tips are kept the same length and form an equilateral triangle, and the fourth tip is 2 mm longer and placed in the center. After the four tips are arranged into a tetrahedral shape, epoxy is applied with the use of a plastic jig to ensure consistent spacing. The distance from the center sensor to any tip is kept around 0.9 mm from the housing tube. The housing tube's inner diameter is slightly larger than the 1.8 mm spacing formed by the sensors. After the tips are arranged, the sensors are inserted into the stainless-steel tube and glued in place. After the probes are in place, the 3D coordinates are found with a high-resolution microscope, so each of the distances are known between probes. The stainless-steel tube is bent to form a 90-degree angle. This allows the probe to be inserted into the bubble column. Figure 3.4 shows the optical probe dimensions, and Figure 3.5 shows the final design.
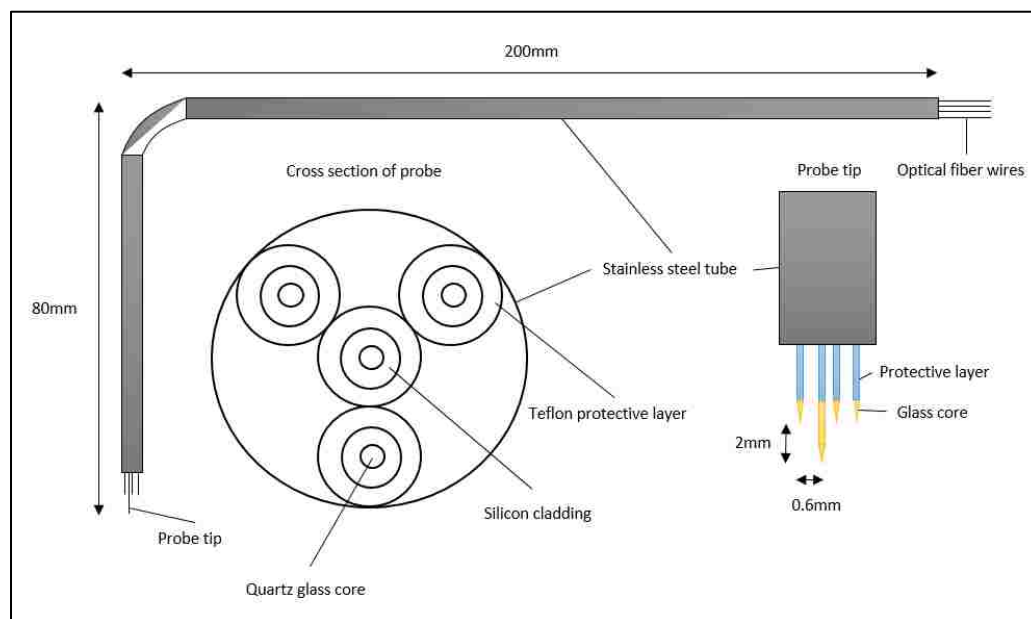
Figure 3.4. Optical Probe
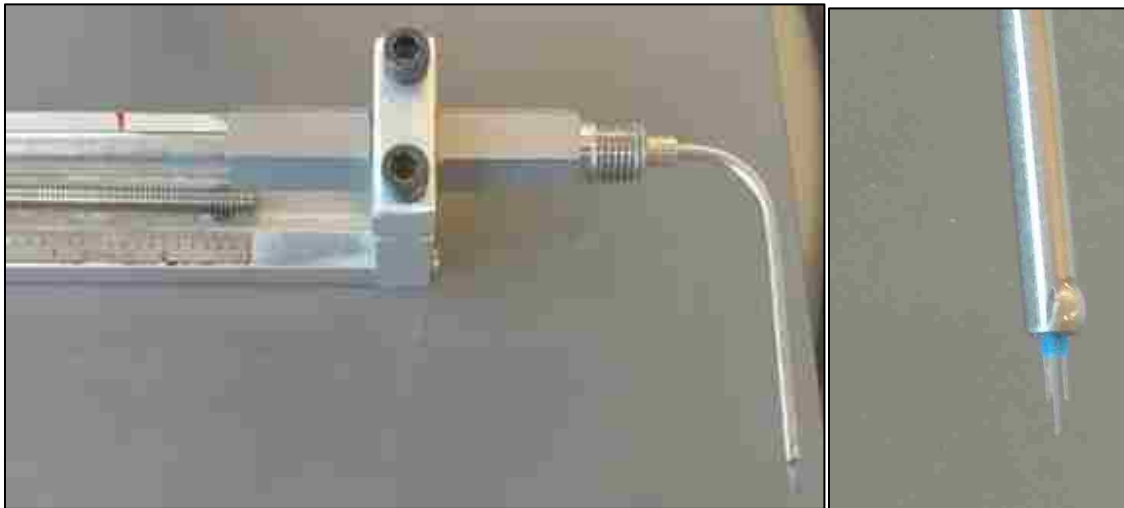
Figure 3.5. Four-Sensor Optical Fiber Probe and Tip

3.3. SYSTEM

The process and data acquisition system (DAQ) for the optical probe and conductivity probe are two different systems. This section will discuss the system from the probe wires to the data acquisition system. Each measurement technique has a different setup and DAQ for collecting data.

3.3.1. Conductivity Probe System. For the conductivity probe, a power supply is hooked up to each sensor that runs through the circuit, as shown in Figure 3.6 and 3.7. When the probe is submerged in water, a constant signal is produced. As soon as the sensor contacts a bubble, the change in conductivity causes the voltage to rise in the system. The signal is transferred through power supply box into the iNET-510 Wiring box and then into the iNEt-430 portable DAQ, as shown in Figure 3.8. The voltage is collected by each channel and at a sample rate of 22 kHz, which is the maximum for the system. The channels are combined into a format that can be interpreted by MATLAB.

Figure 3.6. Power Supply Box
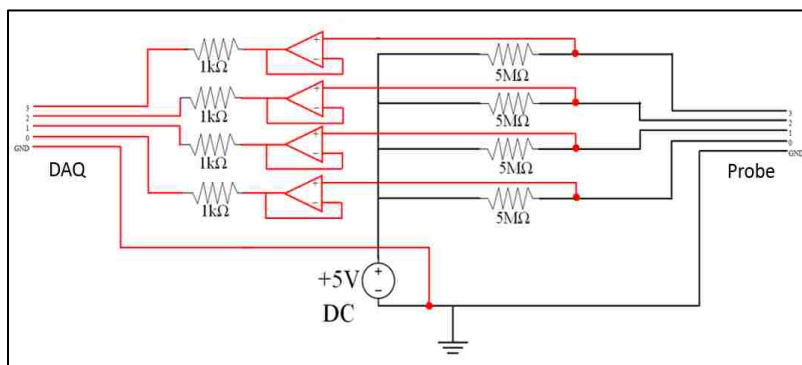
Figure 3.7. Power Supply Circuit

a.   b.

Figure 3.8. Portable DAQ for Conductivity Probe iNET-510 (a) and iNET-430 (b)

3.3.2. Optical Probe System. The wires from each of the optical probes are connected using a standard optical connector. The standard optical connector transmits the laser via electronic unit along the fiber to the tips. The optical probes use the principle of total internal reflection. When the tip of the optical fiber probe is in the liquid, the interface of the glass and water will cause the light to refract. The refraction is due to the comparatively small change in the refractive index. When the tip of the optical probe is exposed to the gas phase, the glass-air interface will cause the light to reflect. Most of the light is reflected at the tip heads, back to the electronic unit where it is received. Then, the light is converted into a voltage via a photodiode, as shown in Figure 3.9.
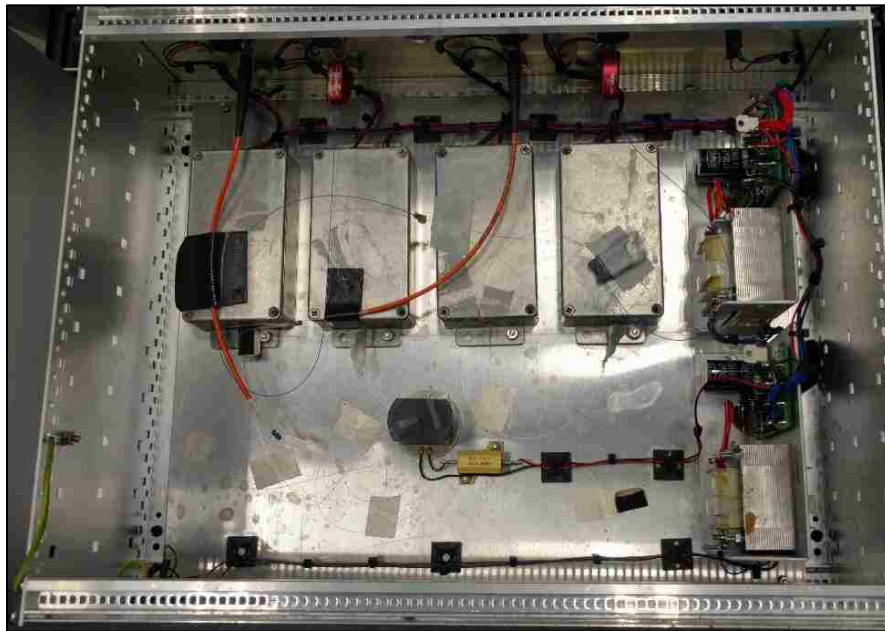
Figure 3.9. System to Convert to Voltage

After the signal is converted to voltage, coaxial cables transmitted the signal into a PD-BNC-16 panel to allow the signal to be converted to the Power DAQ PD2-MFS-8-1M/12 at a sampling frequency of 40 kHz.

3.4. BUBBLE COLUMN

The experiments are conducted in a cylindrical bubble column with a diameter of 5.5 in. and a height of 64 in. from the distributor to the top of the bubble column. The bubble column has sixteen half-inch threaded connectors to allow for instrumentation at different heights. The bubble column can produce bubbly and churn flows reaching up to an estimated 0.8 m/s gas velocity. An actuator is applied to the probes 32 in. from the top of the bubble column to control the radial distance of the measurement device. The distributor has one hundred 1.2 mm holes to distribute the gas phase easily through the cross section of the column. The water is put into the bubble column via the inlet at the bottom of the column, which also acts as the drainage line shown in Figure 3.10. The top of the bubble column is exposed to the air.
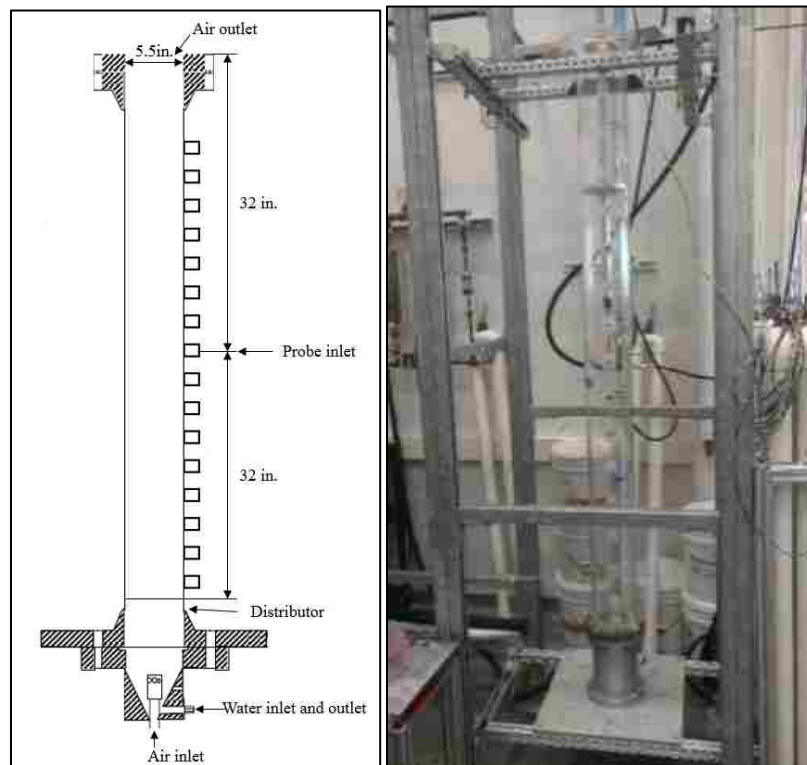
Figure 3.10. Bubble Column

The gas inlet is hooked up to a rotameter set as displayed in Figure 3.11, allowing the gas velocity to be controlled. The range of velocities for the rotameter in the system is 0-1.1 m/s. The gas velocity is limited to 0.8 m/s due to the top of the bubble column being exposed to air and causing overflow.

Figure 3.11. Rotameter to Control Gas Velocity

4. DATA PROCESSING CHANGES

This section will cover the two algorithms and the differences that are implemented into the system. Each implementation should effect the IAC but the VF should remain close to the 10% of the original algorithm. This will ensure the authenticity of the new signal processing algorithm.

4.1. CURRENT DATA PROCESSING

In the original data processing scheme created by Kim, improvements to the miniaturized four-sensor conductivity probe enhance the accuracy and increase the confidence in the two-fluid model. For smoothing the signal, a threshold is applied to the code. This threshold value is used to account for the noise in the signal which is generated from the measuring and data acquisition equipment. Once the trend in the signal is found to be increasing, the peak is determined for each signal. The peak was previously found by determining the position where the gradient of the current location is 10% of the maximum possible gradient for all positions in the signal. This calculated position is used as the starting point to determine the local minimum and maximum of the current peak. Once the peak is found the next step is to determine the local minimum for the signal. Once the local minimum is determined, the rear interface is determined taking the downward slope after the maximum peak is found. After the two positions (i.e., the minimum and maximum) peak heights are determined, a correction is applied for finding the actual front and rear interfaces of the bubbles. The front and rear interfaces are found by determining the

gradient of the current location and then moving backward until the starting location for the front interface is discovered.

In the conditioning algorithm, there are a few areas that can be improved. First, if a sensor penetrates a bubble with a second bubble close to the first bubble, the old algorithm will sometimes miss the trailing bubble. Second, if the individual bubbles are above or below the threshold for the system, occasionally these bubbles are missed completely. For larger sample rates, the bubbles response time to the sensor will overcome the minimum threshold allowing the sensor to capture the small bubbles. However, for lower sample rates the threshold values can have a detrimental effect on the signal when using the four-sensor conductivity probe. The bubbles that have a short residence time will cause only a small increase in the signal voltage.

In 2005, Shen assumed that bubble diameter was much larger than the bubble chord length [73]. In 2008, this assumption led to the research of measuring the interfacial displacement velocity component in two-phase flows [74]. In 2013, Shen developed a method to determine if the bubbles were spherical and moved the larger bubbles into a different group if that bubble was not spherical [75]. Shen's approach demonstrated the problem with small bubble measurements by including the non-spherical bubbles into the overall distribution of the model. However, Shen's algorithm does not shift all group-one bubbles but only spherical bubbles. The algorithm only determines whether a bubble is spherical or not and does not shift the distorted bubbles in the signal processing algorithm. Shen's argument stated that bubble diameter is much larger than the chord length, distorted and spherical bubbles may shift between groups. An algorithm is necessary to calculate the bubble diameter for group one bubbles for achieving this process.

4.2. DYNAMIC RANGING

When using the four-sensor miniaturized conductivity probe, Kim in 1999 suggested that the signal could be normalized by determining the most probable voltage for the lower bound and the highest voltage for the upper bound [3]. The algorithm for signal conditioning separates the voltage into four sections. The first section will contain the liquid phase values, and the fourth section contains the gas phase along with the noise associated with each phase. Kim applied the most probable voltage for the normalization only on the lower bound of the signal. The most probable voltage can also be applied to the upper bound as well. Figure 4.1 shows that the probability density function for a signal.
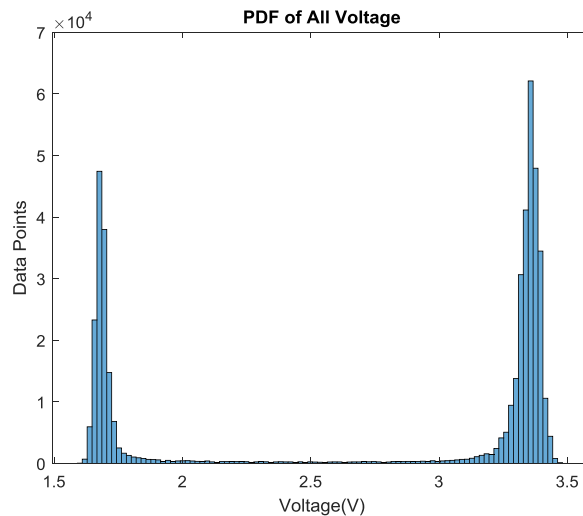
Figure 4.1. PDF of Voltage

A histogram can be applied to define the gas phase and search for bubbles that are very close together in flow regimes. Also, the histogram will help to find the minimum and maximum peaks to normalize the signal. In lower bubble velocities, the most probable

voltage is not always useful for conductivity probes due to the response time of the sensor.

Figure 4.2 demonstrates problems with low gas velocities for conductivity probes.
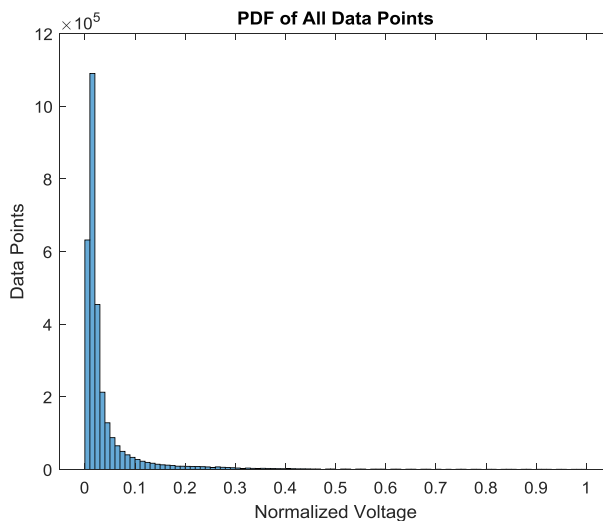
Figure 4.2. Gas Velocity 0.05 m/s Signal

Flows with high bubble velocities, the response of the signal will produce a slight

dip in the signal as shown in Figure 4.3.
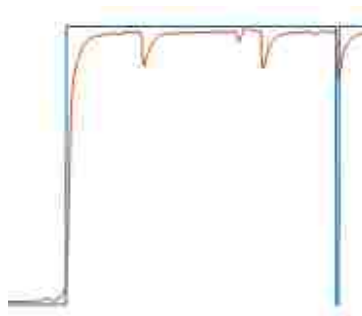
Figure 4.3. Missed Bubbles Due to Bubbles Proximity

In cases where bubble proximity is very close, changing the moving median filter

to larger values will flatten the signal at the top and therefore still miss the bubbles that are

close to one another. To accurately capture all bubbles, a rigorous method is necessary to obtain the closest possible upper and lower bounds to determine the bubbles. The bounds can be found by using the histogram of all voltages in the system. The most probable voltage in the system is near the center of the peak in the histogram as shown in Figure 4.1. Therefore, when partitioning the histogram into bins, a few of the highest values can be used to obtain the middle value for the gas and liquid phase. The background noise can be obtained by first checking for outliers, then removing any extremely large values on the upper bound and extremely small values on the lower bound. Then, the noise in the system can help determine the new minimum and maximum threshold values. The new boundaries can then be applied to normalize the signal to obtain the optimal range in the system. This will allow for detection of small and trailing bubbles.

4.3. SMOOTHING ALGORITHM CHANGES

The smoothing algorithms mentioned in 2.3.1, can contain missed or incorrect bubble sizes due to trailing small bubbles and short response times. In these cases, either the smaller bubbles are collected as one larger bubble, or the bubble is missed completely. To overcome this limitation, a moving comparison of local minimums and maximums were implemented into the code. For all bubbles in the algorithm, after the moving median filter is applied, the algorithm searches for a predetermined amount of points usually between eight and twenty points. These points will determine if the slope is still increasing or if the bubble has hit a peak. If the peak is identified, a small comparison of 0.01 of the normalized signal height is used to determine if the signal has started to fall for smaller bubbles or if there is a small amount of noise at the current comparison location. For the signal where a trailing bubble occurs directly after a larger bubble, the gradient in the previous code will

sometimes miss the small trailing bubbles. Figure 4.4 shows the previous algorithm and the missing bubbles in the signal.
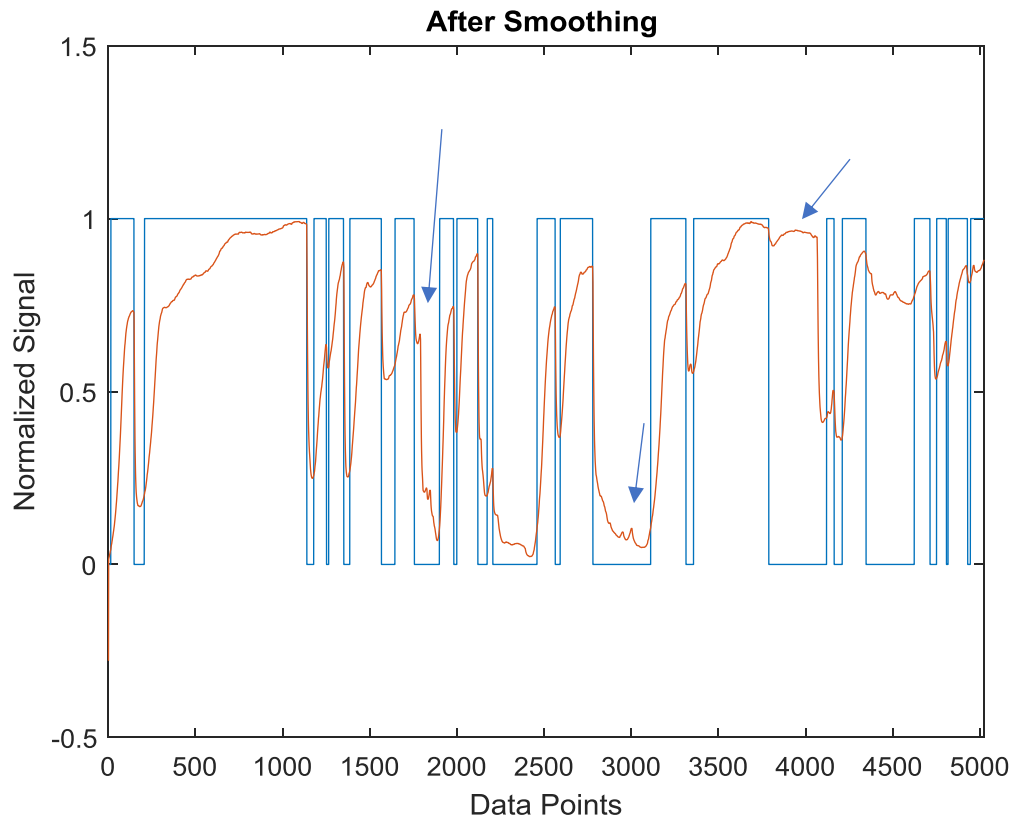
Figure 4.4. Old Smoothing Algorithm and Some of the Missed Bubbles

4.4. VELOCITY SCALING

Formation of a common interface is must to pair each of the signals. The velocity can be discovered by considering the distance between the lead sensor and the first trailing sensor. The two variables can be used to establish a velocity for each bubble. In the system, the bubble velocity can be used to pair the signals. The three common methods to pair the

signals are the cross-correlation method, the drift-flux model, and the user-defined velocity.

For the cross-correlation method, a predefined period is measured and applied to the front interface. Each bubble will have a location where the signal will transition between the liquid and gas phase. The transition point is stored to determine when a bubble encountered the sensor. When a bubble encounters a sensor, it will have a chance to encounter the other three sensors. If the same bubble encounters another sensor, there will be a time delay between the two sensors. This time delay should be applied to pair the two sensors which will produce a common interface. In a system where bubbles are moving at different velocities, there can be challenges pairing the sensors together. In the cross-correlation method, the allotted time frame for the transition points is compared to find the most common delay between the lead sensor and each of the trailing sensors. The most common delay between the two sensors will determine the average time delay in the system. Since each bubble has an associated velocity, it is important to ensure the bubbles are paired with the correct interface. This method is inaccurate when fewer bubbles are collected.

In the DFM, the gas and liquid phase velocities are used to find the average time delay in the system as shown in Equation 36[1]:

$$v_{g\_DFM} = 1.2(j_g + j_f) + 0.25(1 - \alpha_g)^{1.25} \tag{36}$$

In Equation 34, j_g is the superficial gas velocity, j_f is the superficial liquid velocity, and α_g is the VF calculated from the lead sensor. In the user-defined bubble velocity, the user directly inserts a reference velocity to define the average velocity of the system. For all three cases to achieve correct pairing, the time delay is doubled and used to pair the

signals. However, this is not always a good estimate for all bubbles in the system. A cut off at around 25-50% of the mean value is used to remove signals that are too close to one another. For signals that are too far apart, a cut off at 95% of the maximum time delay is used to remove incorrectly paired signals. The pairing in the system should form a Gaussian distribution and have a bell curve shape due to the varying sizes of the individual bubbles. Since the bubbles in the system are moving, it is important to make sure that two different bubble interfaces are not paired together. To achieve correct pairing, bubbles that are extremely close or extremely far apart should not be paired together.

4.5. DETERMINING THE BUBBLE RADIUS

A set of equations is needed to switch from chord length to bubble diameter. This section will go through the system of equations and an overview of the computational method used to solve the system of equations.

4.5.1. Bubble Radius Calculations. A system of equations needed to solve for the radius of a sphere. Kataoka, Ishii, and Serizawa in 1986, and Revankar and Ishii in 1992 formulated a method to calculate the interfacial velocity and normal vector components [44,46]. The equations start with the normal vector for the components of x, y, and z, as shown in Equation 37, and the material derivative in Equation 38:

$$\hat{n} = \frac{\nabla f}{\|\nabla f\|} \tag{37}$$

$$\frac{\partial f}{\partial t} + \vec{v} \cdot \nabla f = 0 \tag{38}$$

Rearranging Equation 2 and solving for interfacial velocity will produce Equation 39:

$$v_{in} = \frac{-\dfrac{\partial f}{\partial t}}{\|\nabla f\|} \tag{39}$$

Combining Equation 3 with Equation 1 will produce Equation 40:

$$\left|\left(\vec{l_{0j}} \cdot \hat{n}\right)\right| = v_{in}\Delta t_{0j}; j = 1,2,3 \tag{40}$$

Equation 40 is the matrix used to determine the normal vector components based on the probes. Equation 5 shows the expanded form of Equation 41:

$$\begin{bmatrix} l_{1x} & l_{1y} & -\Delta t_1 \\ l_{2x} & l_{2y} & -\Delta t_2 \\ l_{3x} & l_{3y} & -\Delta t_3 \end{bmatrix} \begin{bmatrix} \dfrac{n_x}{n_z} \\ \dfrac{n_y}{n_z} \\ \dfrac{v_{in}}{n_z} \end{bmatrix} = \begin{bmatrix} -l_{1z} \\ -l_{2z} \\ -l_{3z} \end{bmatrix} \tag{41}$$

Using the definition of the unit normal vector, Equation 42 can be established:

$$n_x^2 + n_y^2 + n_z^2 = 1 \tag{42}$$

The first system of four equations is the combination of Equation 41 and Equation 42. The unknowns in the system are n_x, n_y, n_z, and v_{in}. In Equation 41 and Equation 42, n_x, n_y, n_z, are the normal x, y and z components and v_{in} is the interfacial velocity. If $\frac{n_x}{n_z}$, $\frac{n_y}{n_z}$, and $\frac{v_{in}}{n_z}$ are defined as new variables, then Equation 41 becomes a linear equation with three unknowns. After solving for $\frac{n_x}{n_z}$, $\frac{n_y}{n_z}$, and $\frac{v_{in}}{n_z}$, Equation 42 can be used to solve each variable individually. After solving for n_x, n_y, n_z, and v_{in}, the next step is to find the bubble velocity and the radius of the bubble by forming a second system of four equations. Figure 4.5 shows a diagram of a bubble with p denoting one of the trailing sensors and 0 representing the leading sensor. Paranjape derived Equations 43-46 to calculate the

diameter of the individual bubbles. In Equations 43-46, R represents the radius of a spherical bubble, $\hat{n}$ is the normal vector, and v_g is the bubble velocity [76].
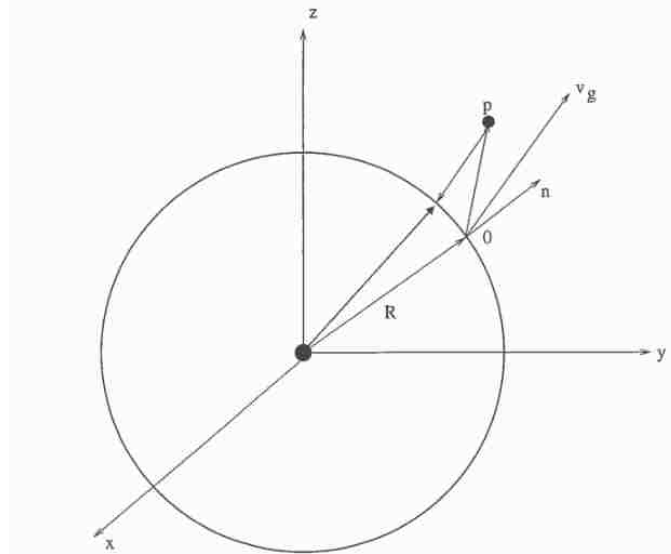
Figure 4.5. Bubble Diagram for Equations 43-45

Equation 43-45 uses the geometry in Figure 4.5 to calculate the radius using the vector coordinates.

$$\left\| R\hat{n} + \vec{l}_{0p} - \vec{v}_g \Delta t_p \right\| = R \tag{43}$$

If the bubble is perfectly spherical, the distance between the lead sensor ($\vec{l}_{0p}$) will cancel the length described by multiplying the bubble velocity with the time-delay between ($\vec{v}_g$) the two probes (Δt_p). Equation 43 represents the wobble of the bubble and reduces the residuals while calculating the radius.

$$\left(R\hat{n} + \vec{l}_{0p} - \vec{v}_g \Delta t_p \right) \cdot \left(R\hat{n} + \vec{l}_{0p} - \vec{v}_g \Delta t_p \right) = R^2 \tag{44}$$

Equation 44 is similar to Equation 43, except that it calculates the dot product to compute the radius squared.

$$\left(v_{gx}^2 + v_{gy}^2 + v_{gz}^2\right)\Delta t_p^2 + 2R\left(\hat{n} \cdot \vec{l}_{0p} - v_{in}\Delta t_p\right)$$
$$- 2\Delta t_p\left(l_{px}v_{gx} + l_{py}v_{gy} + l_{pz}v_{gz}\right) = -l_{0p}^2 \tag{45}$$

In Equation 45, the curvature of the bubble is $2\Delta t_p\left(l_{px}v_{gx} + l_{py}v_{gy} + l_{pz}v_{gz}\right)$,

$2R\left(\hat{n} \cdot \vec{l}_{0p} - v_{in}\Delta t_p\right)$ accounts for the wobble of the bubble, and

$\left(v_{gx}^2 + v_{gy}^2 + v_{gz}^2\right)\Delta t_p^2$ accounts for the displacement when the bubble contacts the trailing

sensor. The square of the distance between the lead and trailing sensor l_{0p}^2, balances the

terms on the right-hand side. Figure 4.6 shows the geometry used to formulate Equation

46. The geometry in Figure 4.6, there are only three equations and four unknown variables.
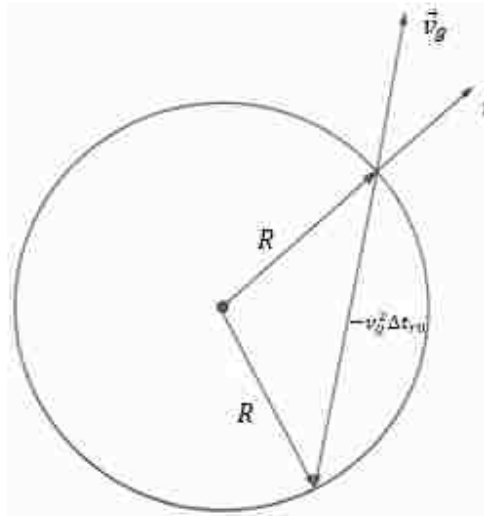
Figure 4.6. Bubble Geometry for Equation 46

To solve the last equation, it is necessary to obtain the chord length of the bubble.

Figure 4.6 shows the geometry used for Equation 44.

$$\left\| R\hat{n} - \vec{v}_g \Delta t_{r0} \right\| = R \tag{46}$$

Equation 10 uses the second geometry to calculate the vector components to find the radius. A computational method is required to solve Equations 43-46. The second system of equations uses a computational method. The trust-region dogleg method is a special technique derived from the trust-region method (TRM). The TRM is indispensable for solving nonlinear problems. It uses the quadratic model from the Taylor series for its calculations. As shown in Equation 47, f_k is the function, B_k is the hessian of the function, g_k^T is the transpose of the gradient of the function, and p is the change in the function's guess.

$$min\, m_k(p) = f_k + g_k^T p + \frac{1}{2} p^T B_k p \qquad (47)$$

First, the TRM defines a region around the current best solution of the problem. Next, the TRM uses the gradient and the hessian to choose the search direction. Figure 4.7 shows an illustration of the dogleg method.
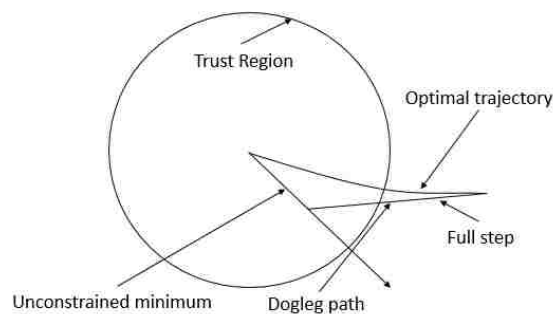
Figure 4.7. Trust-Region Dogleg Search Procedure

The algorithm looks for a step in the direction of the solution by using an anticipated step and a full step in the search region [77]. The TRM finds how large of a step is necessary before improving the direction. If the algorithm has an obvious decrease in the solution

(closer to zero which would be more accurate) from the anticipated step, then the step is taken. If the forward step is small or the solution increases, then the trust-region and next step will shrink. The dogleg method uses is a special case of the TRM. It uses the Powell dogleg procedure for finding the step p. The step p is produced from a convex blend of a Cauchy step and a Gauss-Newton step to find f_k. The trust-region dogleg method (TRDLM) is efficient because the algorithm requires only one linear solve per iteration for the Gauss-Newton step. Also, the TRDLM can be more robust than the Gauss-Newton method using the line search. The TRDLM does not work when the solution to m_k is negative and requires an adjustment inside of the code so that the solution will never become negative. Researchers need to adjust the solution's initial value using the velocity in the z direction to obtain a positive initial guess.

4.5.2. Radius Calculation Corrections. Since distorted bubbles are not spherical and may vary from depending on when the bubble touches the surface, an average radial distance is required for a more accurate diameter. The average is determined by calculating n_x, n_y, n_z, and v_{in} for a bubble shown in Equation 41 and 42. Then, for all variables that contain the distance from the lead sensor to a trailing sensor are calculated for all three pairs. Based on the three values determined for the radius, an average bubble radius is calculated. The value is checked making sure that the bubble radius is positive and follows the assumption that the chord length is larger than the bubble diameter. Each of the three systems of equations for a bubble is run through the TRDLM until there are only slight changes in the bubble radius calculated. For smaller bubbles where the bubble diameter is spherical, the TRDLM converges quickly and may only need to be calculated once. However, bubbles larger than the distorted limit will not work for this method as it

will have a wide variation between solutions. To account for the large changes, the average is determined. However, once the bubble is found to belong to group 2, the algorithm stops. The cord length value is then replaced by the calculated radius, and the bubbles are categorized.

4.5.3. Conductivity Probes and Optical Considerations. There are a few major differences that need to be accounted for when comparing optical and conductivity probes. First, optical probes have a much faster response time when bubbles contact a sensor as shown in Figure 4.8.
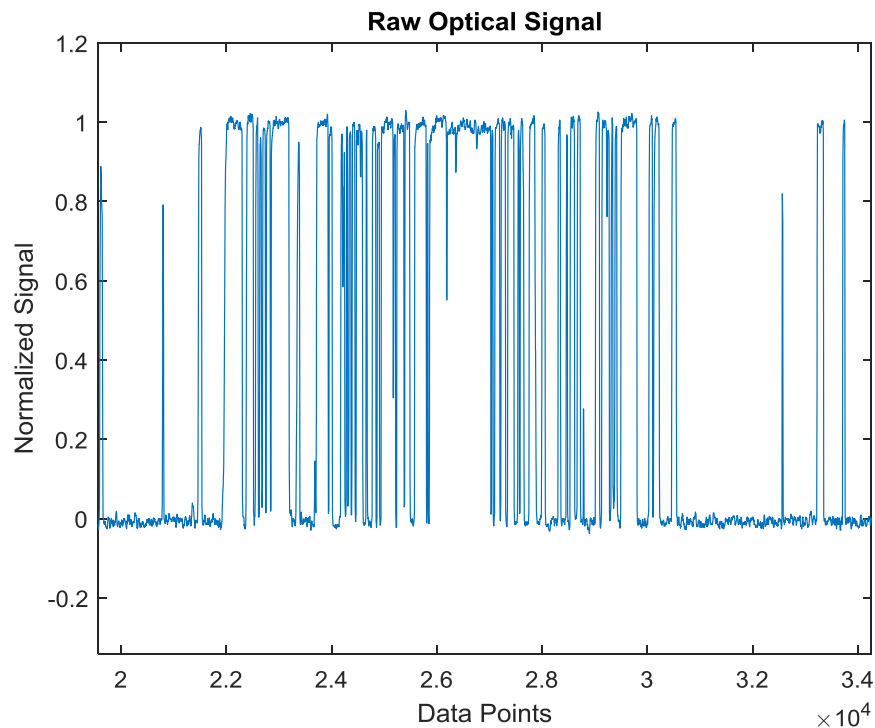
Figure 4.8. Normalized Raw Optical Data

The optical probe with a fast response time, allows for an accurate front and rear interface estimate. The conductivity probes will have a slower response time. However, the

linear approximation will allow for an estimate for the front and rear interface. For either estimation, a sufficient amount of points is necessary to use the linear approximation and determine the front and rear interfaces of the bubbles.

5. RESULTS

The results section will divulge to information obtained after running 300 seconds of data the data obtained will help determine the accuracy of the new algorithm as well as the shortcoming produced.

5.1. SMOOTHING

In many where bubbles are close to one another, some of the bubbles can miss a sensor. The objective of this section is to discuss the differences between the two smoothing methods. The analysis will demonstrate how the additional trailing bubbles that might be missed. In addition, the new minimum and maximum threshold should allow smaller bubbles to be acquired. One of the major reasons for missed bubbles is due to the response time of the sensors. If a bubble comes in contact with a sensor for a very small amount of time, the bubble can be assumed to be background noise. If many of these bubbles are missed, it will start to affect the VF and IAC in the system. To ensure that the bubbles are not missed, the new smoothing algorithm was implemented into the code.

5.1.1. Conductivity Probe Squaring. For conductivity probes, each peak in the signal, will have an exponential increase in voltage as the sensor is exposed to the gas phase. The signal will increase until the maximum allowable voltage in the system is detected. Then, the voltage will stay at the maximum until the bubble leaves the rear interface. When a bubble leaves a rear interface, there will be a decrease in the voltage of the system. The decrease in voltage will continue until another bubble encounters the sensor. At this point, the voltage will rise again until the sensor leaves the rear interface for

the next bubble. If the response time is small, then the smaller group 1 bubbles would normally be missed in the original algorithm. To demonstrate the differences between the two algorithms, a comparison of the peaks that represent the individual bubbles will be displayed. Figure 5.1 demonstrates the two algorithms.   Figure 5.1a shows the previous algorithm and   Figure 5.1b shows the new algorithm.   Figure 5.1 is for the position closest to the wall for a gas velocity of 0.05 m/s.
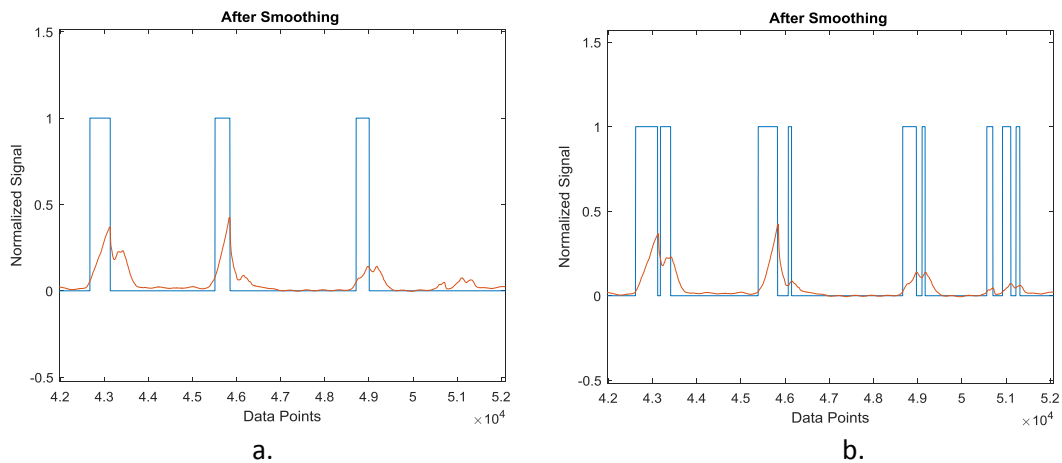
Figure 5.1. Old Version (a) and New Version (b)

There are many spherical and distorted bubbles in lower gas velocities. The spherical and distorted bubbles may appear behind the first bubble and the newer algorithm attempts to catch all of these trailing bubbles. The trailing bubbles will not add a large amount to the VF but will increase the IAC in the system. The next two figures show a magnified in version of   Figure 5.1 and how the new algorithms catch two types of missing bubbles that were encountered in   Figure 5.1. Figure 5.2 shows a few examples of trailing

bubbles. To improve the threshold, the bubbles with a small residence time are also now acquired by the new algorithm as shown in Figure 5.3.

a.   b.
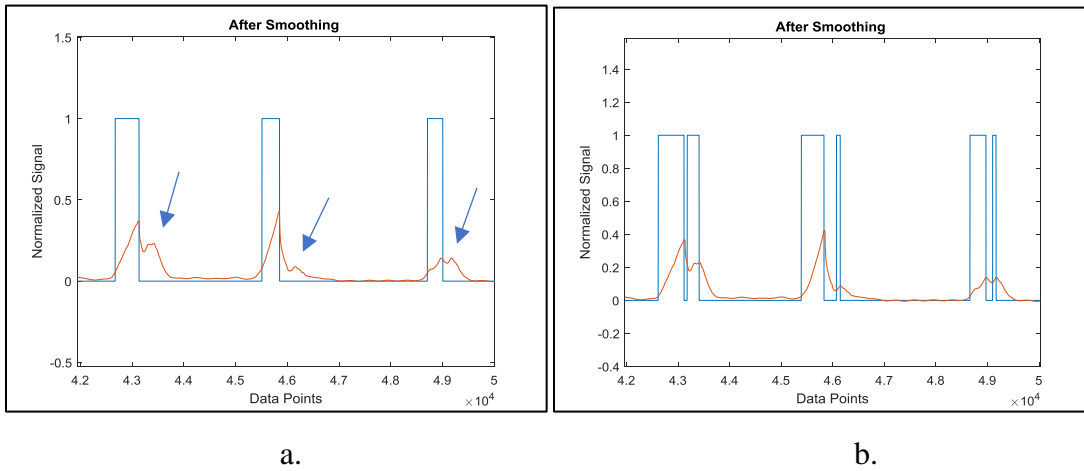
Figure 5.2. Old Version (a) New Version (b) for Trailing Bubbles

a.   b.
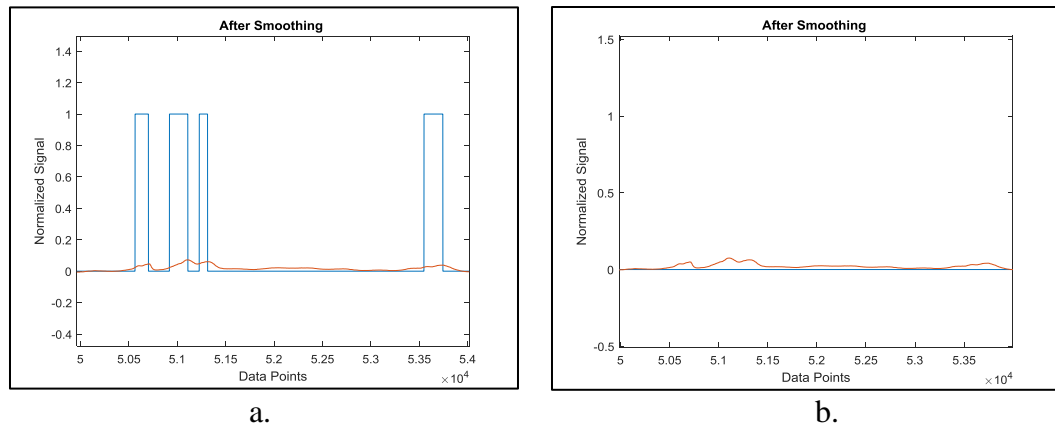
Figure 5.3. Old Version (a) New Version (b) for Threshold Missed Bubbles

Figure 5.4 is when the bubble velocity in the bubble column is 0.7 m/s. Figure 5.4 shows when a large number of bubbles are clustered together. The biggest challenge regarding the bubbles with a small response time is the location of the front and rear

interfaces. The front and rear interfaces are not always easy to identify. To determine the change in the number of bubbles, Figure 5.5 shows a comparison for all radial location for the lead sensor at four different gas velocities. The four gas velocities used are 0.05, 0.18, 0.30, and 0.7 m/s.
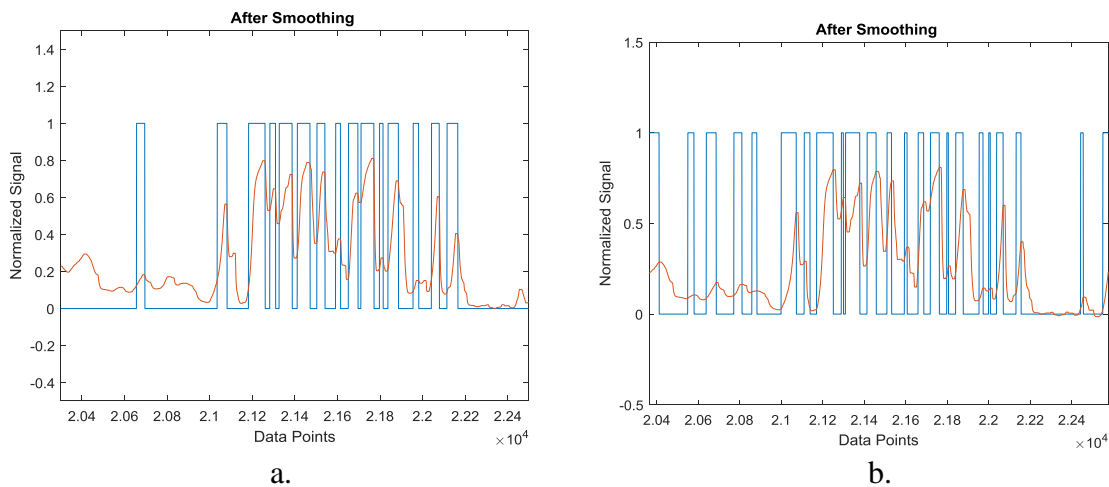
Figure 5.4. Old Version (a) New Version (b) for jg of 0.7 m/s
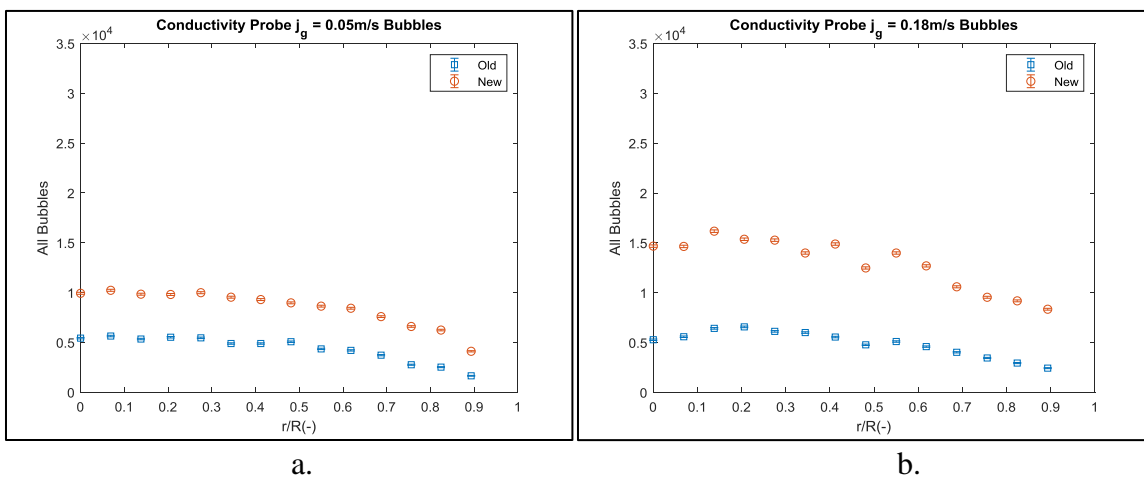
Figure 5.5. Conductivity Probe All Bubbles Collected for Old and New Algorithm 0.05 (a), 0.18 (b), 0.30 (c), and 0.7 (d) m/s for 300s
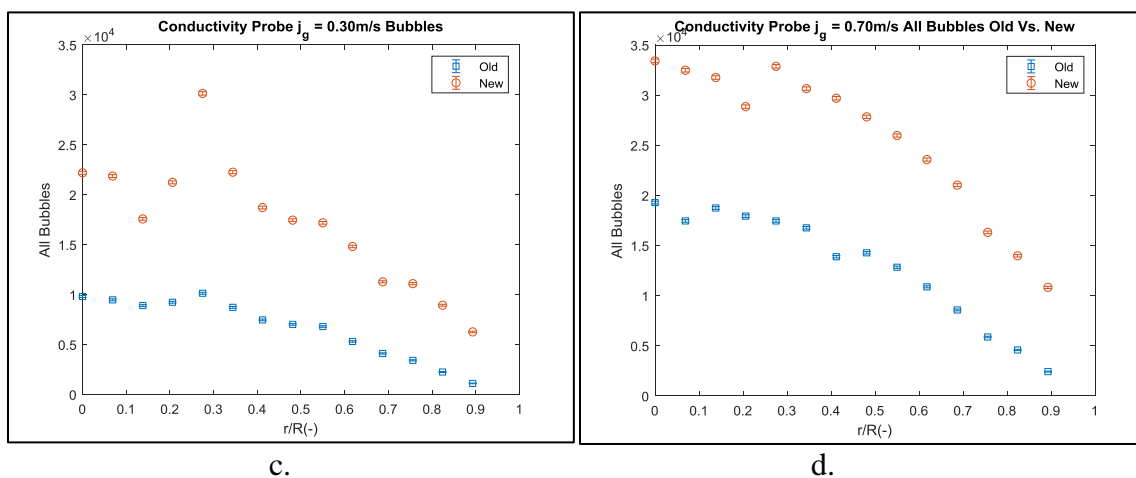
Figure 5.5. Conductivity Probe All Bubbles Collected for Old and New Algorithm 0.05 (a), 0.18 (b), 0.30 (c), and 0.7 (d) m/s for 300s continued

Each of the different gas velocities are used to show a range of different types of flows from bubbly to churn turbulent flows, as displayed in Figure 5.. There is an increase in the amount of bubbles picked up after the completion of the smoothing process for the conductivity probe. Figure 5. demonstrates that as the bubble velocity increases the number of bubbles, in the system also increases. The code shows an increase in the number of bubbles collected by the new algorithm. These new bubbles are the trailing bubbles and bubbles that grazed the sensor for a short duration. The new bubbles will change the IAC and VF within the system. For each velocity, the percent error between the old and new versions is shown in Table 5.1. The difference between the two algorithms, normally show that the number of bubbles captured are twice or even three times as much as the previous algorithm. This is due to the response time of the conductivity probe not increasing enough to catch the smaller and trailing bubbles.

Table 5.1. Conductivity Probe All Bubbles Old and New Algorithm 0.05 (V1), 0.18 (V2), 0.30 (V3), and 0.7 (V4) m/s 300s Percent Error

r/R	V1	V2	V3	V4
(-)	(%)	(%)	(%)	(%)
0	83.39	178.28	126.73	73.22
0.069	81.18	162.79	130.40	495.29
0.138	83.86	152.14	97.35	69.35
0.206	77.69	133.36	129.91	60.90
0.275	83.19	149.06	197.27	502.87
0.344	95.87	132.99	155.21	82.85
0.412	90.81	168.47	150.49	509.01
0.481	76.69	161.50	148.35	95.19
0.55	98.57	174.02	152.12	102.52
0.618	101.02	175.86	179.63	116.38
0.687	104.16	163.79	174.74	144.89
0.756	138.11	177.12	225.06	177.12
0.824	149.36	212.65	299.62	204.67
0.893	149.61	244.50	463.01	344.85

5.1.2. Optical Probe Squaring. The residence time is much quicker for optical probe, therefore it does not affect the results with a smaller sample rate as much when compared to the conductivity probe. The rise and fall of the signal is almost instantaneous and therefore fewer bubbles are missed. The difference between the two smoothing

methods is therefore expected to be less obvious. There are cases where the bubbles brush against the probe and a small signal is not registered by the threshold. In addition, trailing bubbles must be extremely close to the first bubble to cause any missed bubbles. Figure 5.6 displays trailing bubbles and threshold in an optical probe system. Trailing bubbles will still occur in the optical probe but are less likely.

a.   b.
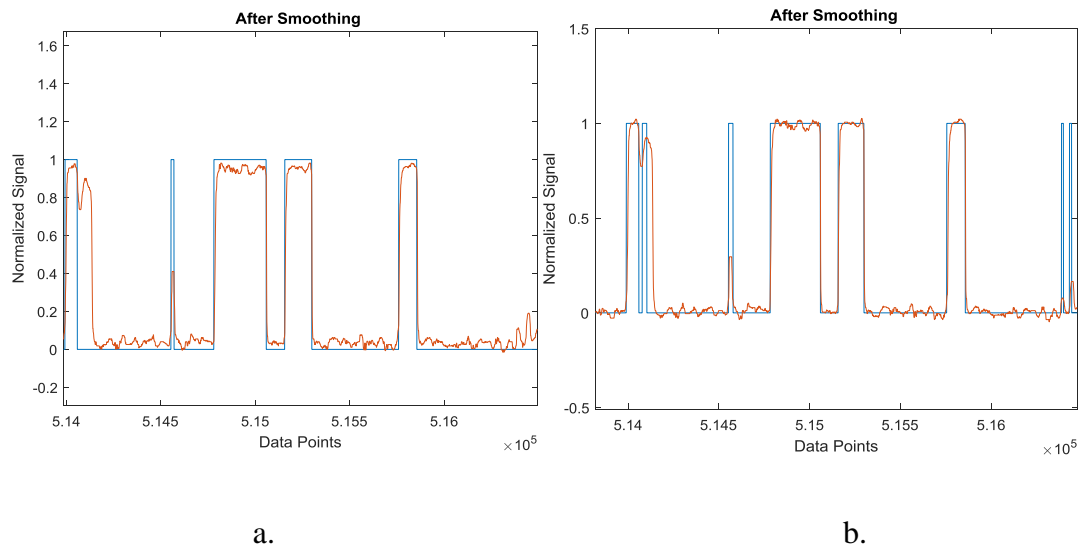
Figure 5.6. Old Version (a) New Version (b) for Trailing Bubbles and Missed Threshold Values

To determine the change in the number of bubbles for the optical probe case, Figure 5.7 shows a comparison of all radial locations for the lead sensor for four different gas velocities. The four gas velocities used are 0.05, 0.18, 0.30, and 0.7 m/s. Each of the different gas velocities are used to show a range of different types of flows from bubbly to churn turbulent flows. An increase in the amount of bubbles picked up after the completion of the smoothing process can be determined.

Figure 5.7. Optical Probe All Bubbles Collected for Old and New Algorithm 0.05 (a), 0.18 (b), 0.30 (c), and 0.7 (d) m/s for 300s

In Figure 5.7 there is a much smaller change in the amount of bubbles registered by the new and old squaring process. Between two algorithms there is a slight increase in the total amount of bubbles collected in the new algorithm. These bubbles will help to estimate the number of bubble that should be in the system since the optical probe has a much faster response time then the conductivity probe. Table 5.2 has the error associated between the two algorithms.

Table 5.2. Optical Probe All Bubbles Old and New Algorithm 0.05 (V1), 0.18 (V2), 0.30 (V3), and 0.7 (V4) m/s 300s Percent Error

r/R	V1	V2	V3	V4
(-)	(%)	(%)	(%)	(%)
0	3.46	5.25	20.69	4.05
0.069	3.44	0.96	6.75	2.77
0.138	3.00	3.76	9.91	3.42
0.206	3.45	4.36	18.41	3.62
0.275	15.03	4.15	22.76	3.29
0.344	3.71	4.57	3.08	3.80
0.412	4.12	5.86	5.18	3.58
0.481	5.12	6.82	15.01	4.85
0.55	5.12	5.78	7.84	5.14
0.618	4.05	11.75	17.32	5.79
0.687	7.77	4.53	11.68	6.31
0.756	9.62	10.53	12.26	8.32
0.824	53.72	14.22	12.61	8.50
0.893	43.17	41.90	66.71	9.34

The difference is under 10% in most radial positions when comparing the two algorithms. However, there is still an increase in the number of bubbles picked up by the new algorithm. These bubbles are mainly due to trailing bubbles since the response time is much quicker than the conductivity probe.

5.1.3. Optical and Conductivity Probe Squaring Comparison. Figure 5.8 is a comparison of the amount of bubbles registered by the new algorithm for the optical and conductivity probes.

Figure 5.8. Optical and Conductivity All Bubbles Collected for Old and New Algorithm 0.05 (a), 0.18 (b), 0.30 (c), and 0.7 (d) m/s 300s

To make up for the small response time of the signal a lower threshold is applied. The measurements that are taken near to the wall of the bubble column are not as easily

picked up by the conductivity probe. Table 5.3 is the difference in bubbles between the

optical and conductivity probes.

Table 5.3. Optical and Conductivity All Bubbles Old and New Algorithm 0.05 (V1), 0.18 (V2), 0.30 (V3), and 0.7 (V4) m/s Percent Error

r/R	V1	V2	V3	V4
(-)	(%)	(%)	(%)	(%)
0	0.12	0.99	8.87	13.53
0.069	2.49	3.96	22.45	10.90
0.138	7.71	14.75	12.04	11.29
0.206	4.19	8.30	1.65	1.95
0.275	8.84	10.39	38.38	18.77
0.344	0.89	1.33	25.86	12.19
0.412	3.09	12.77	6.59	7.16
0.481	10.60	1.44	1.16	10.33
0.55	4.92	20.06	8.53	7.53
0.618	15.99	0.07	6.28	1.31
0.687	15.18	1.37	22.62	0.99
0.756	11.02	8.32	14.58	14.06
0.824	16.12	1.10	15.44	20.87
0.893	58.61	6.85	56.55	30.29

For the first two velocities, the amount of bubbles in the system are within 15% of

one another with outliers occurring mainly close to the wall of the bubble column. The

amount of bubbles collected when comparing the optical and conductivity probe using the new algorithm are much closer than the original algorithm. The bubbles in higher gas velocities become very chaotic. The number of bubbles can change between measurements, but the VF and IAC should show a similar pattern to one another. To determine if these new signals are bubbles or if they are noise in the system, a comparison of the pairing of all four sensors is analyzed next.

5.2. PAIRING

Since the conductivity probe for the new algorithm collected more bubbles there should be an increase in the number of effective bubbles in the system. The 2-sensor probe approximation is used for spherical bubbles and a 4-sensor probe is used for distorted and group 2 bubbles. Smaller bubbles that brush against the probes are more likely to be smaller in size and may miss at least one sensor.

5.2.1. Conductivity Pairing. For bubbles in the system since there is an increase in the total amount of bubbles registered by the conductivity probe, there should be an increase in the amount of paired bubbles as well. The data in the next section displays the amount of effective bubbles that are pierced by all four sensors for both the older algorithm and the newer algorithm. Figure 5.9 displays the effective bubbles for the conductivity probe for the four gas velocities 0.05, 0.18, 0.30, and 0.7 m/s respectively. The bubbles follow a similar pattern as the total number of bubbles. The effective bubbles are increasing at a similar rate as the total bubbles increase. The new signals are therefore likely to be additional bubbles and not just noise registered by the algorithm. The bubbles higher velocities show a much closer comparison to the old and new algorithm for the conductivity probe.
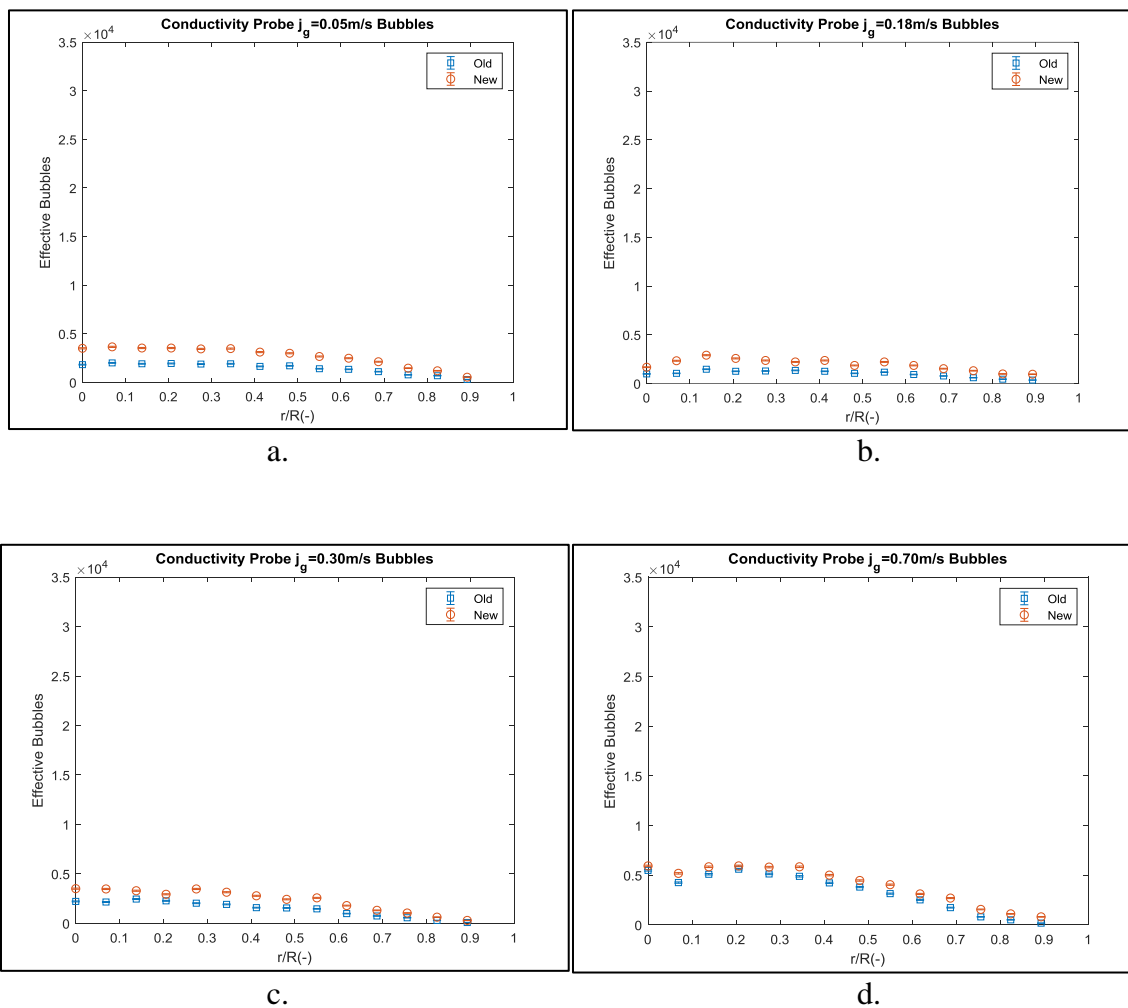
Figure 5.9. Conductivity Probe Effective Bubbles Collected for Old and New Algorithm
0.05 (a), 0.18 (b), 0.30 (c), and 0.7 (d) m/s 300s

Table 5.4 displays the change in the amount of paired bubbles in the bubble column. The total number of bubbles in the first velocity doubled and this increase is also shown in the amount of effective bubbles. Table 5.4 shows the increase to 100% in many cases for comparing the conductivity probe for the two algorithms. The lowest change is in the 0.3 m/s gas velocity near the wall of the system where much less bubbles appear.

Table 5.4. Conductivity Probe Effective Bubbles Old and New Algorithm 0.05 (a), 0.18 (b), 0.30 (c), and 0.7 (d) m/s 300s Percent Error

r/R	V1	V2	V3	V4
(-)	(%)	(%)	(%)	(%)
0	69.25	57.98	8.29	69.25
0.069	124.13	60.56	21.56	124.13
0.138	97.95	35.23	14.25	97.95
0.206	104.77	30.06	5.73	104.77
0.275	82.18	70.99	13.87	82.18
0.344	65.49	63.60	19.28	65.49
0.412	90.74	75.07	18.09	90.74
0.481	78.72	54.78	16.91	78.72
0.55	90.93	76.95	29.51	90.93
0.618	100.93	85.49	23.66	100.93
0.687	99.72	74.50	54.88	99.72
0.756	119.06	81.27	94.18	119.06
0.824	125.12	110.14	111.52	125.12
0.893	167.26	230.95	361.45	167.26

5.2.2. Optical Pairing. Figure 5.10 shows the amount of paired bubbles by the optical probe for both algorithms. For the first velocity, there is a slight decrease in the amount of paired bubbles. As the gas velocity increases and the bubble density at the center

of the bubble column increases, there is a slight increase in the number of effective bubbles

in the system that were successfully paired.
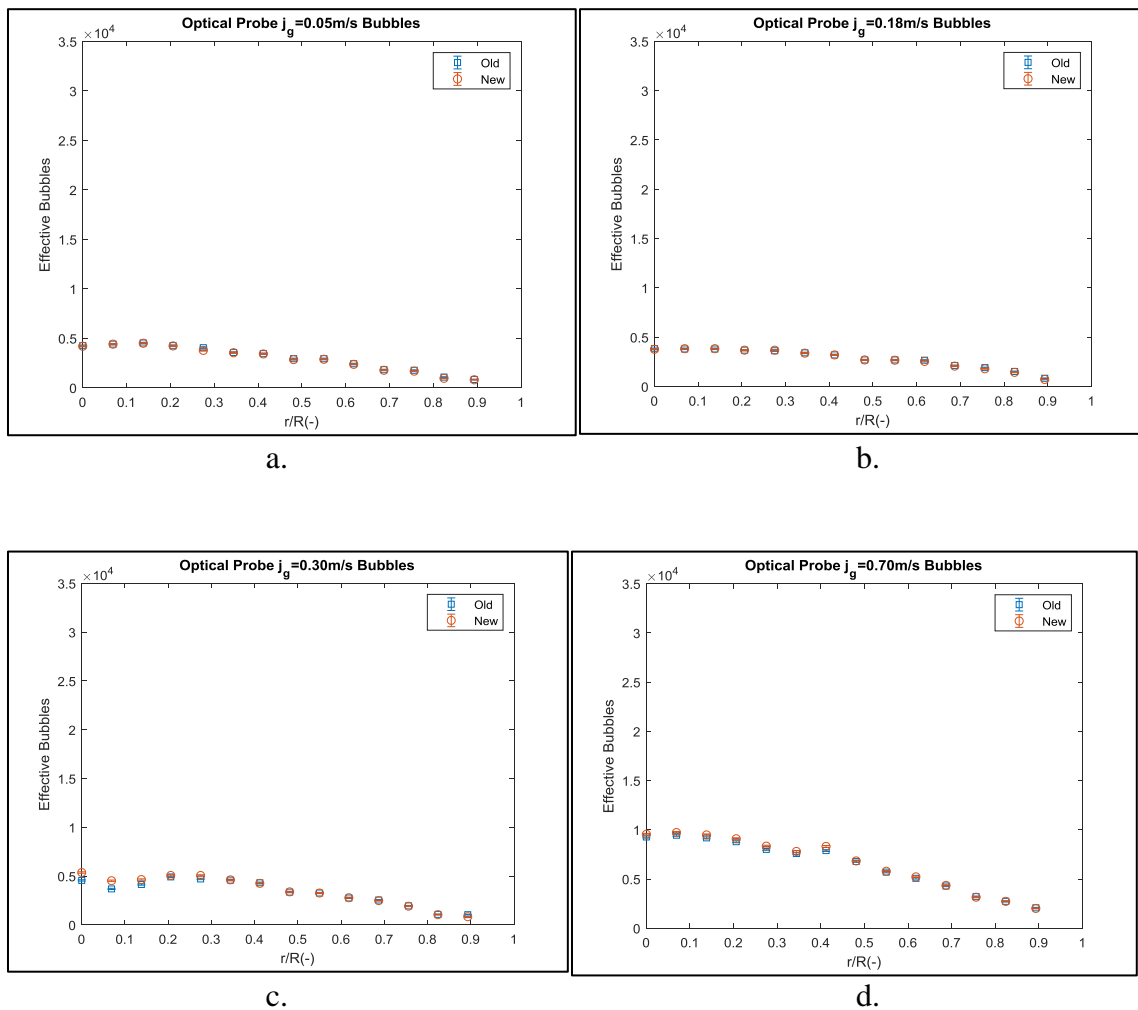
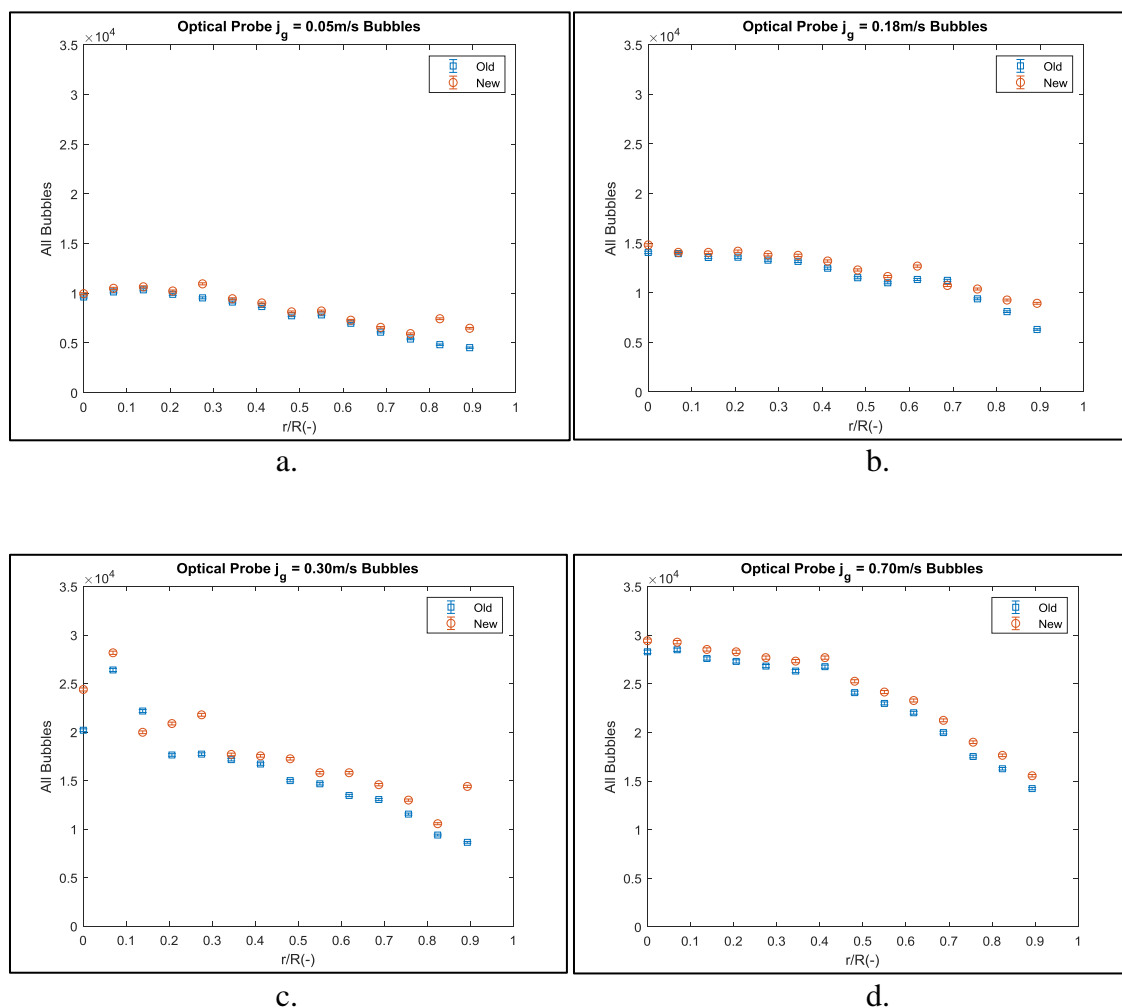

Figure 5.10. Optical Probe Effective Bubbles Collected for Old and New Algorithm 0.05
(a), 0.18 (b), 0.30 (c), and 0.7 (d) m/s 300s

Table 5.5 displays the change in the amount of bubbles paired. The change in most

cases is negligible which should occur due to the small response time using the optical

probe. The other missing bubbles are due to the switch in paring locations, threshold values

chosen, and trailing bubbles that are now registered

Table 5.5. Optical Probe Effective Bubbles Old and New Algorithm 0.05 (V1), 0.18
(V2), 0.30 (V3), and 0.7 (V4) m/s 300s Percent Error

r/R	V1	V2	V3	V4
(-)	(%)	(%)	(%)	(%)
0	1.62	1.25	17.81	3.08
0.069	0.41	0.87	22.99	2.96
0.138	0.53	0.71	12.94	3.20
0.206	1.13	0.16	3.17	3.59
0.275	6.24	1.15	7.51	3.97
0.344	1.51	0.88	0.52	2.69
0.412	1.04	0.75	1.25	5.05
0.481	2.25	0.11	0.53	0.88
0.55	1.83	0.45	0.09	1.47
0.618	2.72	4.28	0.65	3.20
0.687	3.75	3.52	2.01	1.47
0.756	3.75	5.33	1.68	1.96
0.824	13.19	6.64	1.68	0.11
0.893	2.89	16.01	18.39	2.77

5.2.3. New Version Optical and Conductivity Effective Bubble Comparison.

When comparing the optical and conductivity probes with one another, the optical probe should have more successfully paired bubbles than the conductivity probe. The difference between the two is due to the response time of the signal. The optical probe, with an almost instantaneous response time will increase the number of effective bubbles in the system. Figure 5.11 shows a comparison between the effective bubbles between the two methods.
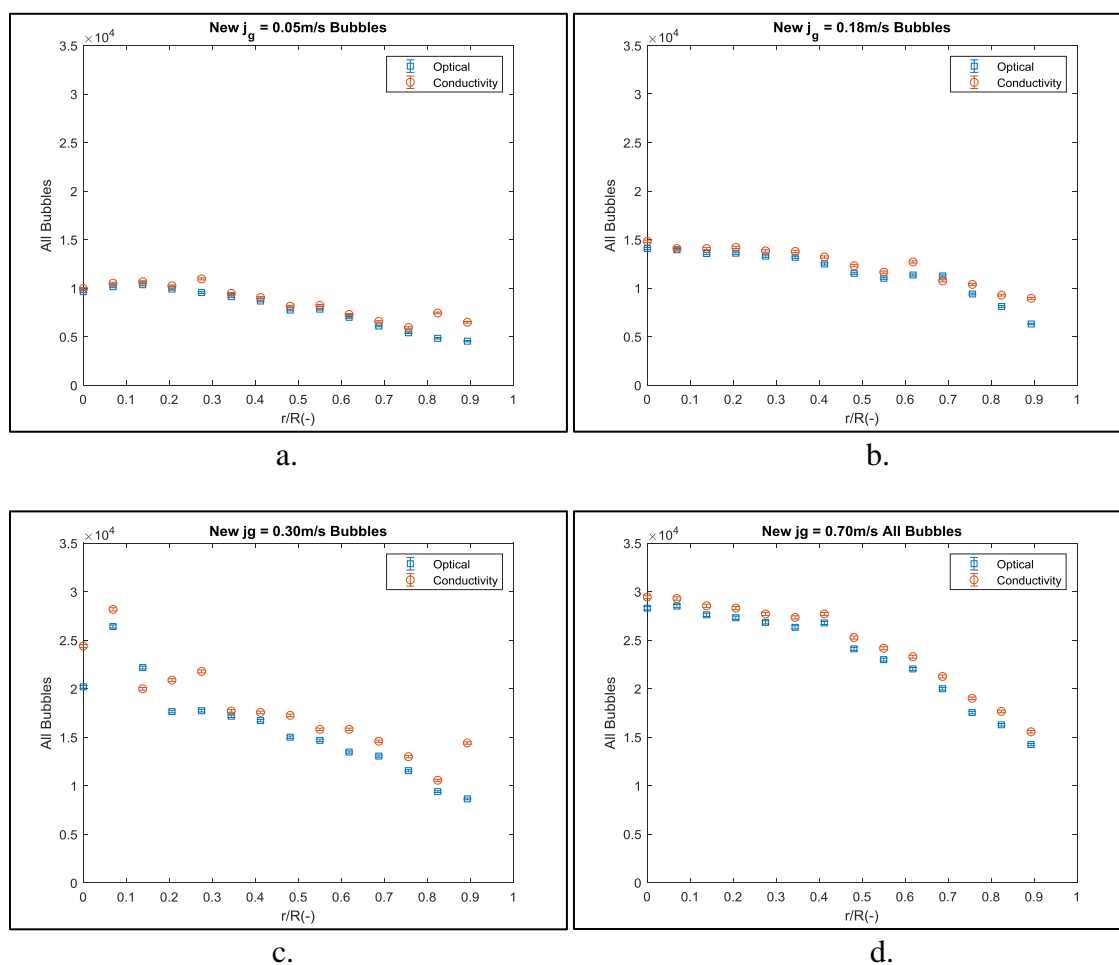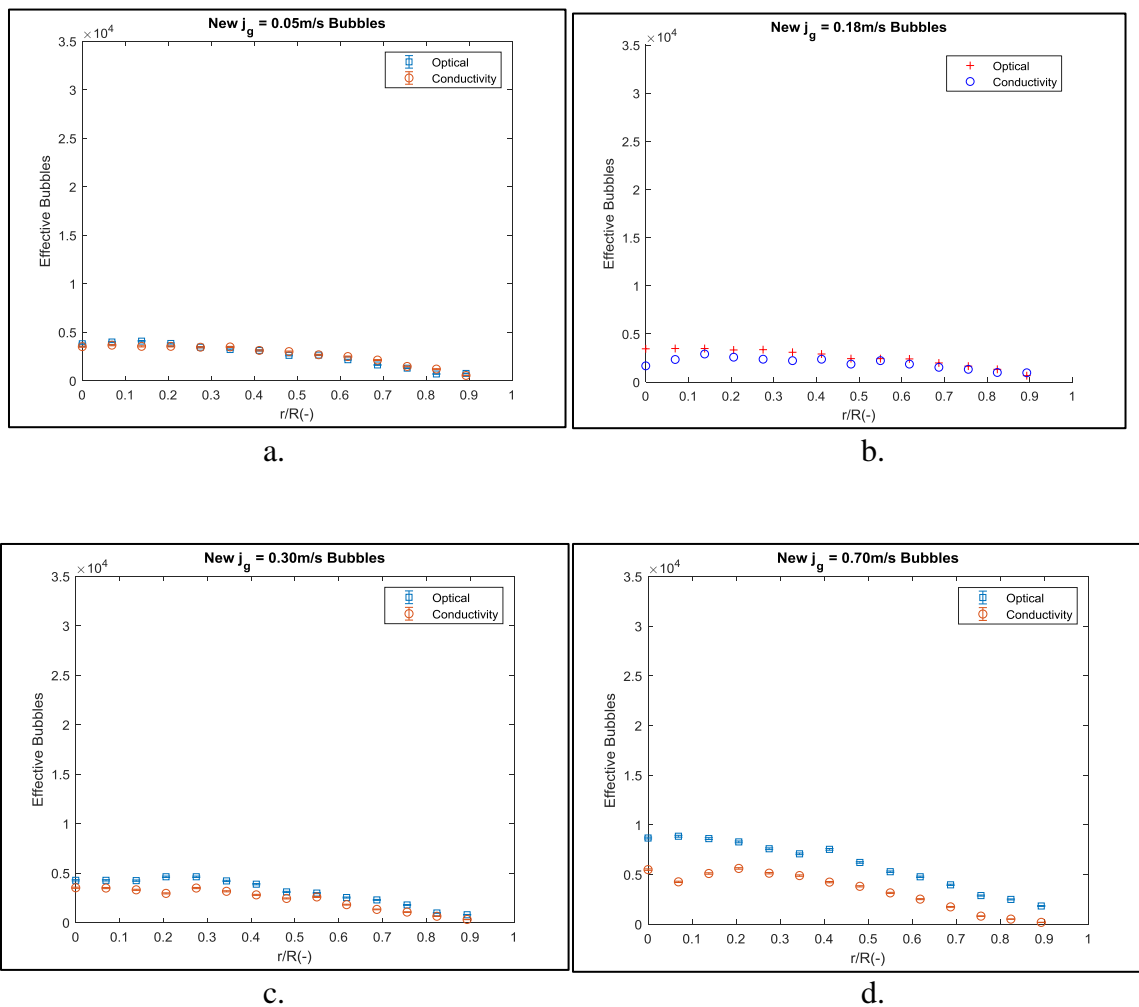

Figure 5.11. Optical and Conductivity Effective Bubbles for Old and New Algorithm
0.05 (a), 0.18 (b), 0.30 (c), and 0.7 (d) m/s 300s

In Table 5.6 the optical probe has a larger amount of effective bubbles in almost every case and the gap between the effective bubbles increases as the bubble density increases in the bubble column. This indicates that the sample time of the system should be longer for the conductivity probe to give an accurate comparison of VF and IAC.

Table 5.6 Optical and Conductivity Effective Bubbles Old and New 0.05 (V1), 0.18 (V2), 0.30 (V3), and 0.7 (V4) m/s Percent Error

r/R	V1	V2	V3	V4
(-)	(%)	(%)	(%)	(%)
0	8.17	51.05	17.44	36.88
0.069	8.25	32.50	18.64	51.65
0.138	13.67	16.72	22.01	40.65
0.206	8.06	22.89	36.00	32.09
0.275	0.44	29.24	24.56	32.48
0.344	8.70	28.20	24.52	30.82
0.412	0.39	17.98	27.73	43.91
0.481	15.80	24.08	21.15	38.69
0.55	1.48	9.36	12.85	40.40
0.618	16.34	22.50	28.55	46.88
0.687	32.77	23.00	42.38	56.18
0.756	12.76	20.77	40.85	71.79
0.824	75.00	23.45	35.11	78.93
0.893	27.35	49.30	61.63	90.26

5.3. DIAMETER VS. CHORD LENGTH

After bubbles are placed into groups, the group 1 effective bubbles are processed through the TRDLM algorithm to determine which group each bubble belongs. Since the chord length should be smaller than the diameter there should be an increase in the number of group 2 bubbles. A comparison of the original algorithm of the code will be used as a benchmark for the results.

5.3.1. Old Version Optical and Conductivity Bubble Comparison. Figure 5.12 contains a comparison between the optical and conductivity probes for the old algorithm.
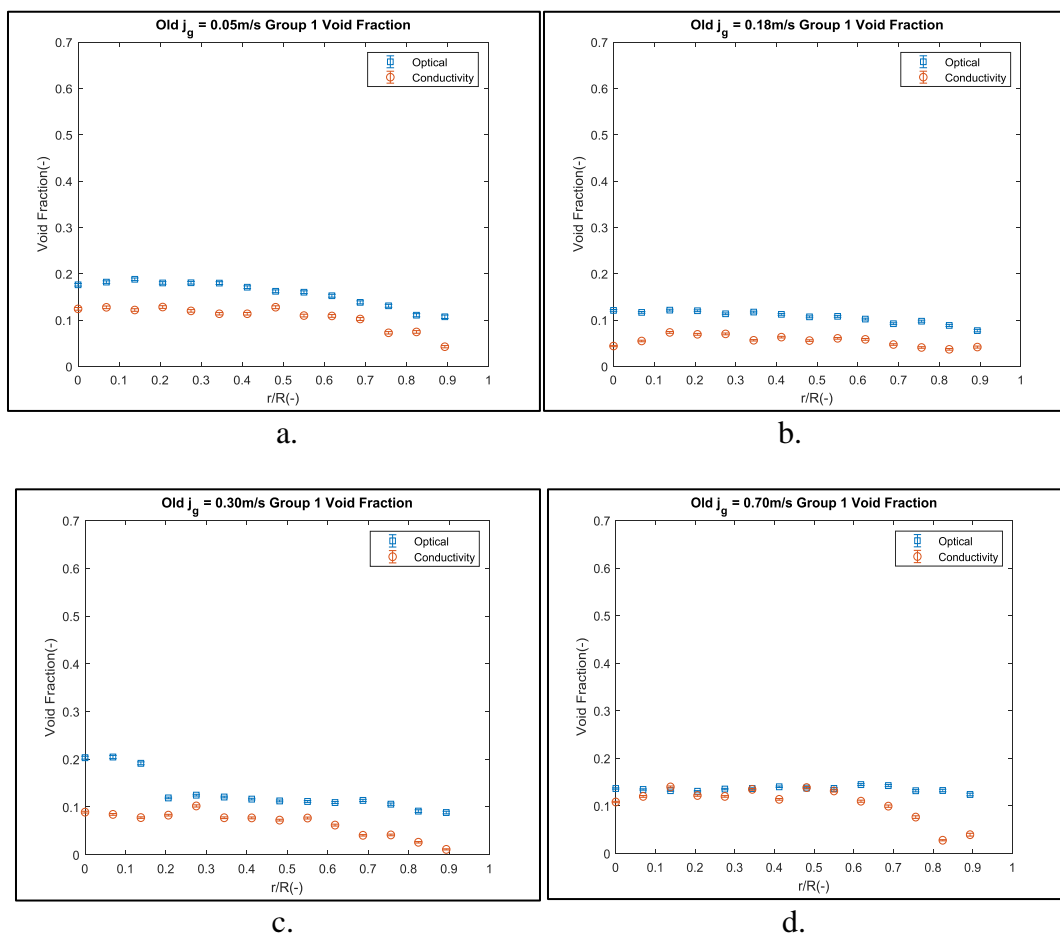
Figure 5.12 Original Optical and Conductivity Group 1 Void Fraction for Gas Velocities 0.05 (a), 0.18 (b), 0.30 (c), and 0.7 (d) m/s

There is a large variation between VF if many of the smaller bubbles are missed. In addition, breakup and coalescence will occur more often as the gas velocity increases. The percent error between the two methods are displayed in Table 5.7. There is normally around a 30% error between the two methods for group 1 VF.

Table 5.7. Original Optical and Conductivity Group 1 Void Fraction for jg of 0.05 (V1), 0.18 (V2), 0.30 (V3), and 0.7 (V4) m/s Percent Error

r/R	V1	V2	V3	V4
(-)	(%)	(%)	(%)	(%)
0	29.46	63.66	56.12	20.81
0.069	29.89	52.96	58.72	10.79
0.138	35.25	39.62	59.37	5.91
0.206	28.86	42.38	30.34	6.74
0.275	33.61	38.24	18.11	11.38
0.344	36.80	51.96	35.90	1.25
0.412	33.51	43.81	33.73	18.84
0.481	21.21	47.90	35.67	0.73
0.55	31.46	43.98	31.09	3.81
0.618	28.57	42.90	43.18	24.12
0.687	25.96	48.75	64.24	30.29
0.756	44.54	58.15	60.81	42.03
0.824	32.64	58.37	71.44	79.06
0.893	60.26	45.98	87.33	68.20

Figure 5.13 has a comparison between the four different gas velocities to demonstrate the difference between the two methods and the trend of the VF. For all four velocities, the optical probe measures a higher VF for group 1 bubbles. More of the group 1 bubbles are distinguished by the optical probe over the conductivity probe. Figure 5.13 contains the Group 2 VF for the four velocities. As the gas velocity increases there is an increase in the amount of Group 2 bubbles that are detected in the bubbles column.
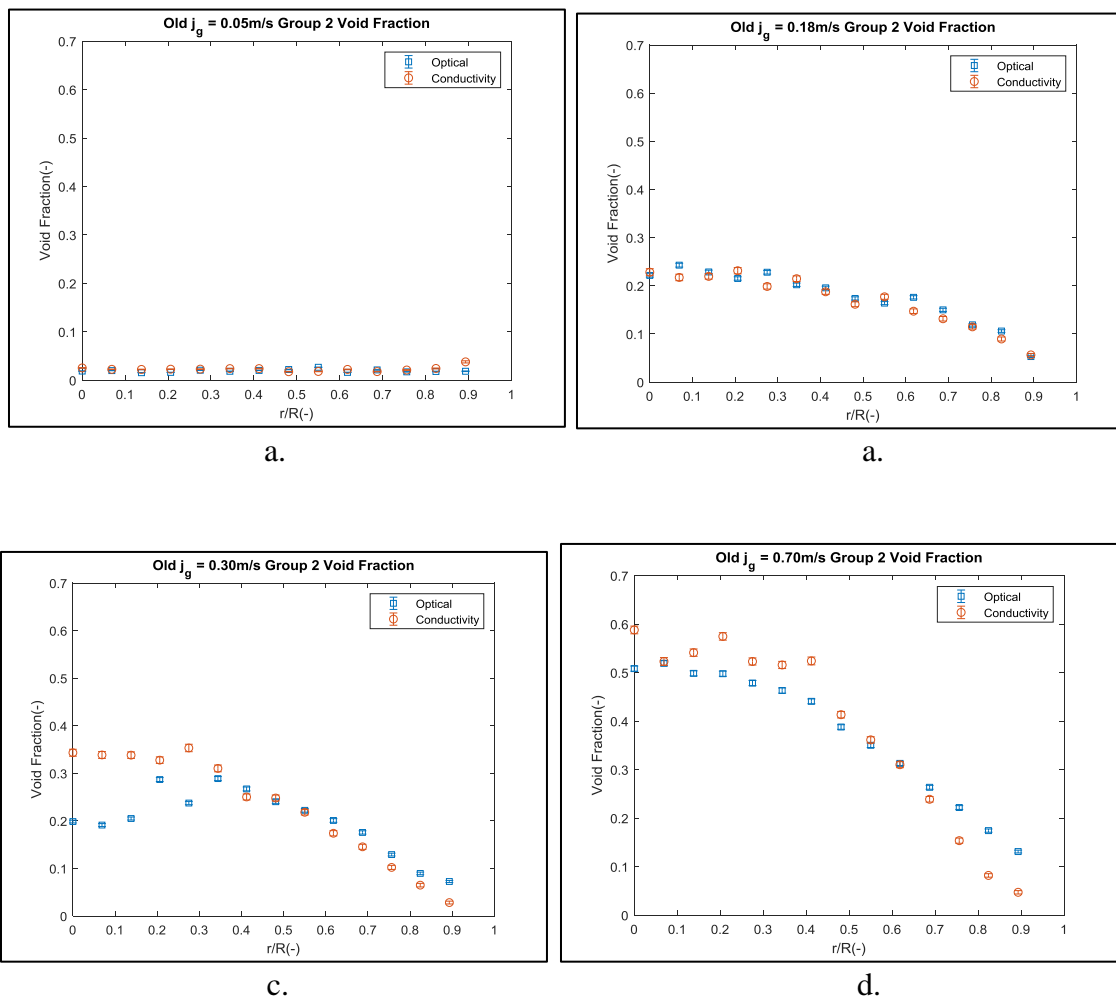
Figure 5.13. Original Optical and Conductivity Group 2 Void Fraction for jg of 0.05 (a), 0.18 (b), 0.30 (c), and 0.7 (d) m/s

The percent error between the different methods for group 2 bubbles are displayed in Table 5.8. The values for the group 2 bubbles are closer to one another than the group 1 bubbles indication that the conductivity probe is missing smaller bubbles.

Table 5.8. Original Optical and Conductivity Group 2 Void Fraction for jg of 0.05 (V1), 0.18 (V2), 0.30 (V3), and 0.7 (V4) m/s Percent Error

r/R	V1	V2	V3	V4
(-)	(%)	(%)	(%)	(%)
0	34.21	3.02	72.86	15.68
0.069	13.00	10.50	77.09	0.71
0.138	42.68	4.02	64.98	8.57
0.206	40.49	7.53	14.22	15.45
0.275	10.58	12.93	48.76	9.30
0.344	29.57	6.23	7.41	11.38
0.412	18.14	4.19	6.32	18.90
0.481	20.27	6.96	3.25	6.55
0.55	32.09	7.98	1.85	3.20
0.618	37.42	16.35	13.39	0.86
0.687	16.36	12.33	17.19	9.37
0.756	21.84	3.53	20.90	30.78
0.824	34.07	15.55	27.57	53.01
0.893	104.30	6.59	61.02	64.07

Figure 5.14 shows a comparison for the total VF in the system. The values for the total VF is further apart in the lower gas velocities that the higher. However, the missing group one bubbles from the signal will still affect the total VF in the system.

Figure 5.14. Original Optical and Conductivity Total Void Fraction for jg of 0.05 (a), 0.18 (b), 0.30 (c), and 0.7 (d) m/s

In almost all cases the optical probe shows a larger VF than the conductivity probe. The larger VF is due to the sensitivity of the optical probe allowing for the smaller bubbles

to be collected at the 22 kHz sample rate. Table 5.9 shows the total VF for all bubbles in the system. The total VF in the system is much closer to each other than the group 1 bubbles with an average difference of 22%. With the largest difference near the wall of the bubble column.

Table 5.9. Original Optical and Conductivity Total Void Fraction for jg of 0.05 (V1), 0.18 (V2), 0.30 (V3), and 0.7 (V4) m/s Percent Error

r/R	V1	V2	V3	V4
(-)	(%)	(%)	(%)	(%)
0	23.25	20.53	7.64	7.94
0.069	25.61	24.28	6.87	1.65
0.138	29.24	16.53	4.92	7.99
0.206	23.16	10.35	1.18	10.84
0.275	29.00	21.33	25.76	4.76
0.344	30.58	15.12	5.32	8.51
0.412	28.00	18.66	14.65	9.78
0.481	21.00	22.55	9.15	5.02
0.55	31.59	12.64	11.59	1.21
0.618	22.25	26.00	23.89	8.26
0.687	24.61	26.21	35.68	16.72
0.756	36.79	28.08	38.88	35.00
0.824	23.12	35.01	49.70	64.16
0.893	35.85	24.56	75.47	66.08

As the position of the optical and conductivity probes near the center of the bubble column the IAC of the system will increase. Figure 5.15 displays the IAC for spherical and distorted bubbles for both the optical and conductivity probe for the original code. Since the optical probe is picking up a larger amount of bubbles the IAC increases with the number of bubbles.
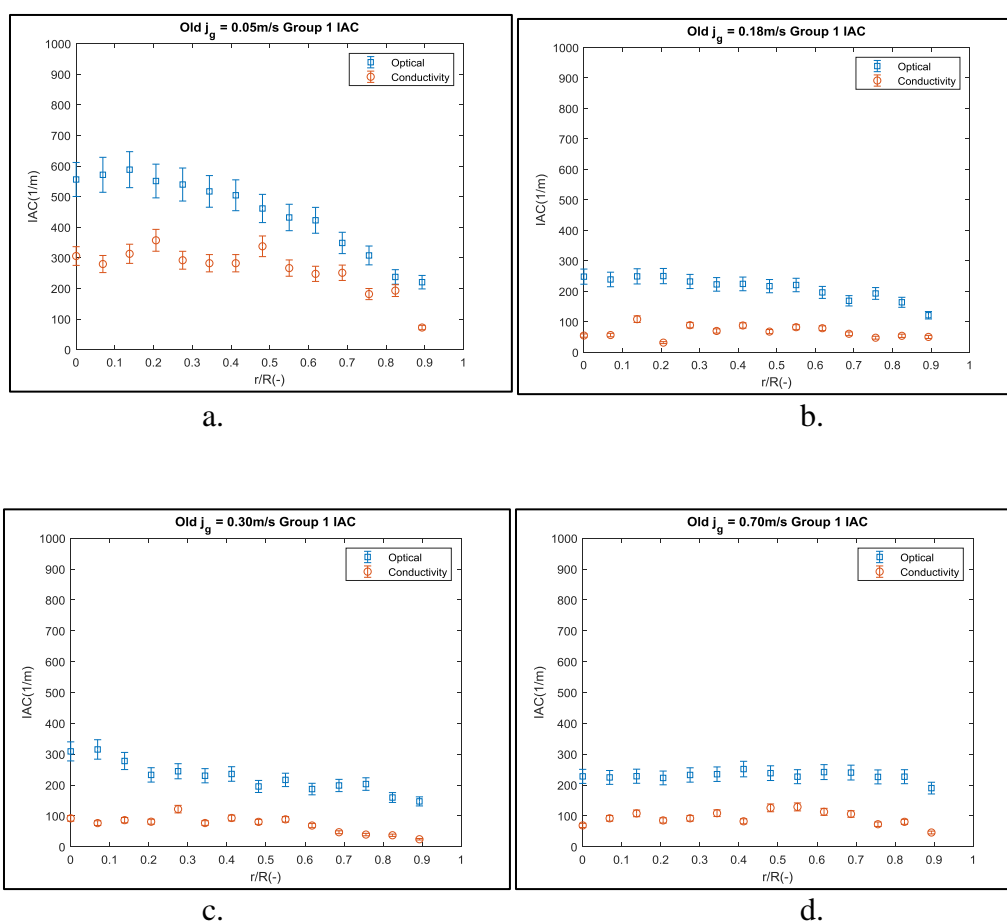
Figure 5.15. Original Optical and Conductivity Group 1 IAC for jg of 0.05 (a), 0.18 (b), 0.30 (c), and 0.7 (d) m/s

Table 5.10 contains the difference between the conductivity and optical probes. Since smaller bubbles are more likely be registered by the optical probe, more of these

bubbles are picked up. The increase in smaller bubbles increases the IAC in the system. The increases in bubbles will create a more accurate representation of the IAC in the bubble column.

Table 5.10. Original Optical and Conductivity Group 1 IAC for jg of 0.05 (V1), 0.18 (V2), 0.30 (V3), and 0.7 (V4) m/s Percent Error

r/R	V1	V2	V3	V4
(-)	(%)	(%)	(%)	(%)
0	44.99	77.85	70.22	69.75
0.069	51.05	76.29	75.73	59.00
0.138	46.76	56.39	69.00	52.71
0.206	35.16	87.31	65.20	61.78
0.275	45.86	61.68	50.19	60.41
0.344	45.39	68.55	66.63	53.77
0.412	44.02	60.78	60.51	67.29
0.481	26.80	68.72	58.76	47.17
0.55	38.30	62.68	59.05	43.16
0.618	41.41	59.79	63.25	53.25
0.687	27.97	64.03	76.36	55.84
0.756	41.01	75.19	80.60	67.79
0.824	18.80	67.00	76.72	64.46
0.893	67.24	58.49	83.49	75.77

Figure 5.16 displays the group 2 IAC for the original algorithm for both optical and conductivity probes. The values for the four velocities are similar in all cases. Figure 5.16 demonstrations that the group 2 bubbles are normally collected and therefore the IAC is similar to one another. Table 5.11 contains the percent error for group 2 IAC. Most of the values are around 10 % of each other with the largest deviation in the 0.05m/s gas velocity. The lowest velocity has the largest density of smaller bubbles in the system.
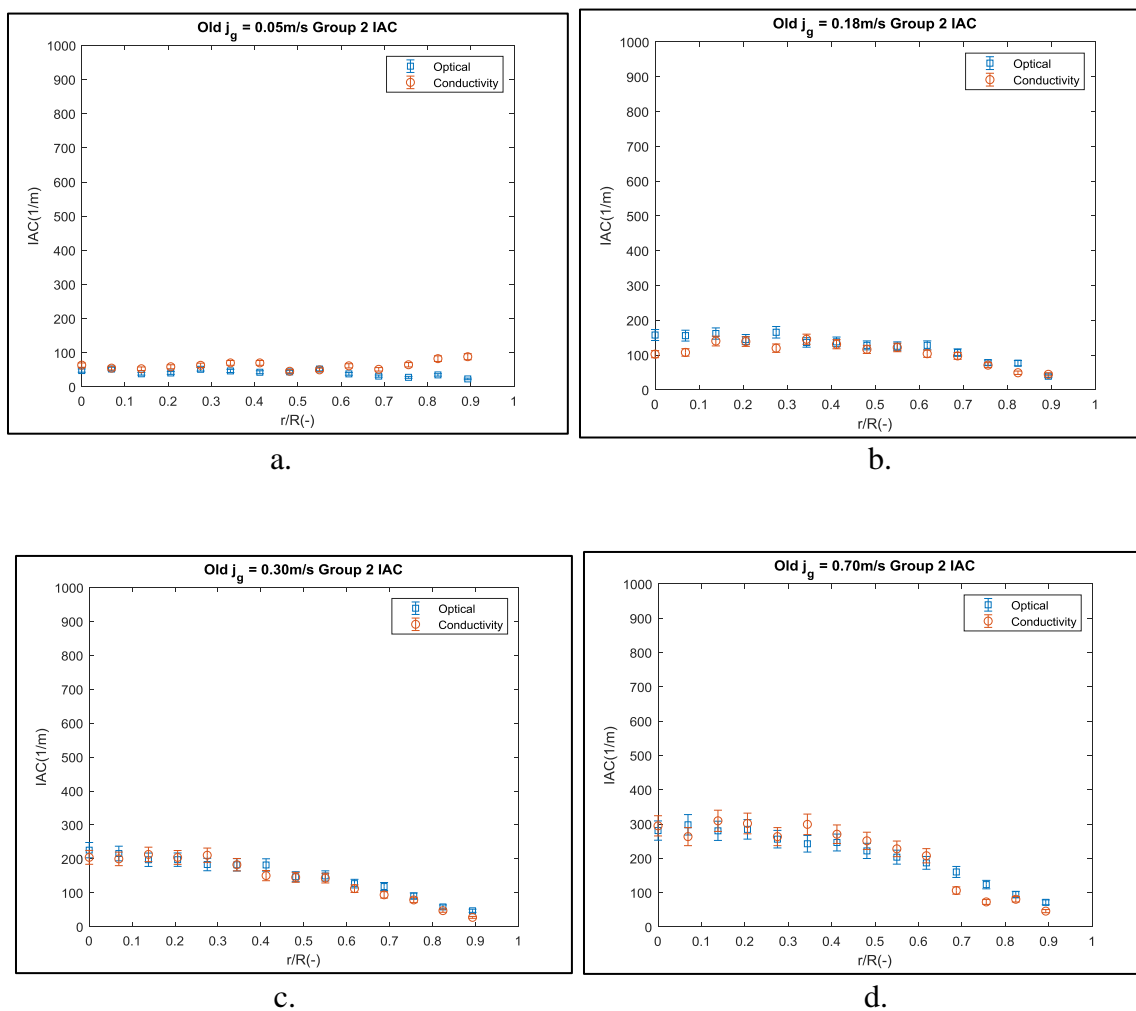
Figure 5.16. Original Optical and Conductivity Group 2 IAC for jg of 0.05 (a), 0.18 (b), 0.30 (c), and 0.7 (d) m/s

Figure 5.17 contains the total IAC for the original algorithm for both the conductivity and optical probes. For the optical probes, since a large amount of group 1 are registered, the total IAC reflects the increase. Therefore, for the 22 kHz sample rate, a large amount of data is missing for the conductivity probe and the optical probe should be used to benchmark the data for the new algorithm.

Table 5.11. Original Optical and Conductivity Group 2 IAC for jg of 0.05 (V1), 0.18 (V2), 0.30 (V3), and 0.7 (V4) m/s Percent Error

r/R	V1	V2	V3	V4
(-)	(%)	(%)	(%)	(%)
0	33.36	34.90	9.41	4.91
0.069	4.92	30.99	7.33	11.59
0.138	38.43	13.28	7.96	10.41
0.206	44.46	3.98	3.33	6.04
0.275	22.64	27.58	14.98	2.90
0.344	50.24	6.76	0.20	23.33
0.412	63.68	4.96	17.25	9.81
0.481	3.97	9.01	1.21	13.27
0.55	4.43	2.79	4.28	11.91
0.618	61.91	18.75	11.66	11.10
0.687	62.59	8.77	20.73	33.77
0.756	131.56	9.13	12.92	40.91
0.824	135.55	35.85	18.88	14.44
0.893	278.83	13.43	41.46	35.72

Table 5.12 contains the percent error between the optical and conductivity probes for the original algorithm. There is a large deviation for all velocities. The large deviations are due to the missing smaller bubbles that are not received by the conductivity probe at 22kHz.

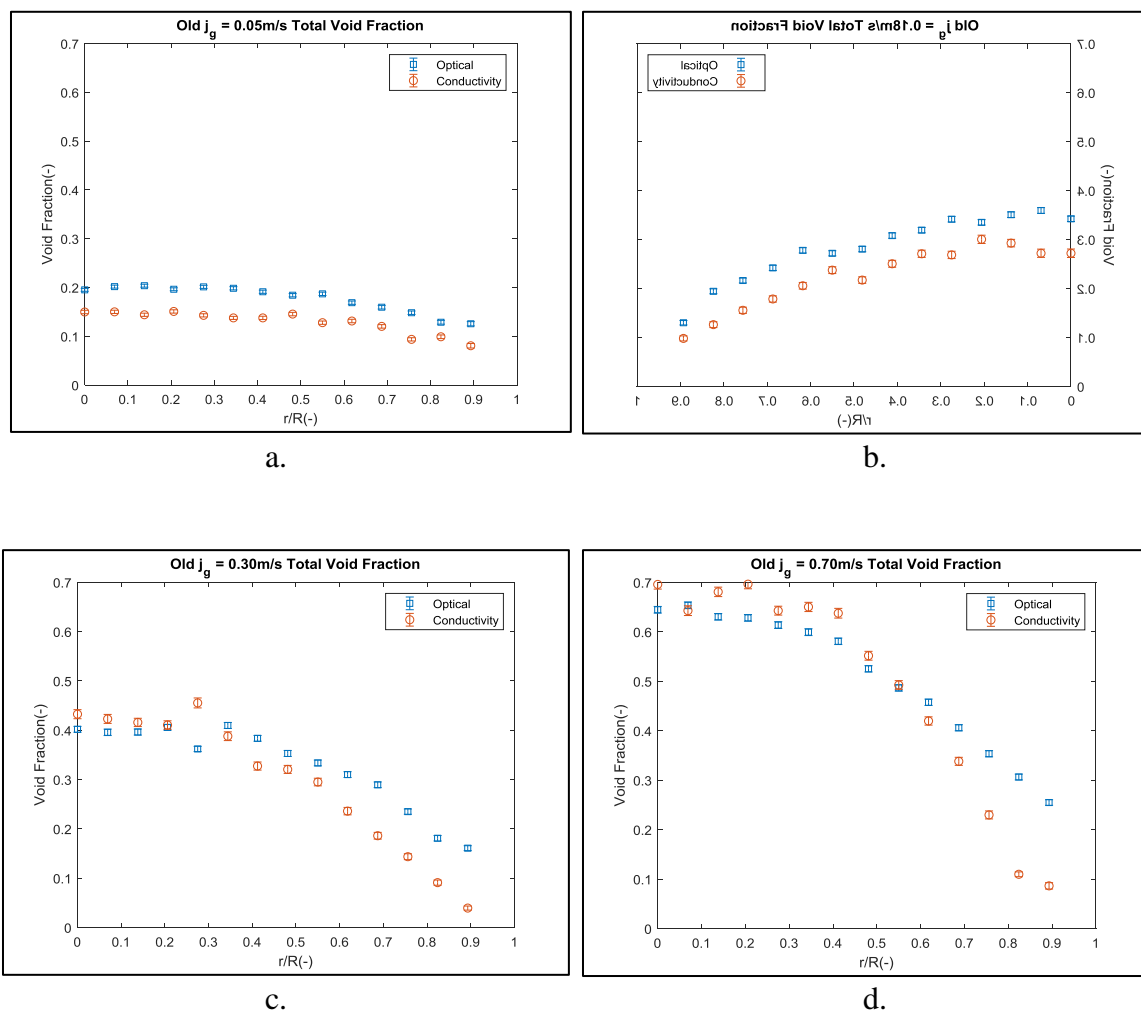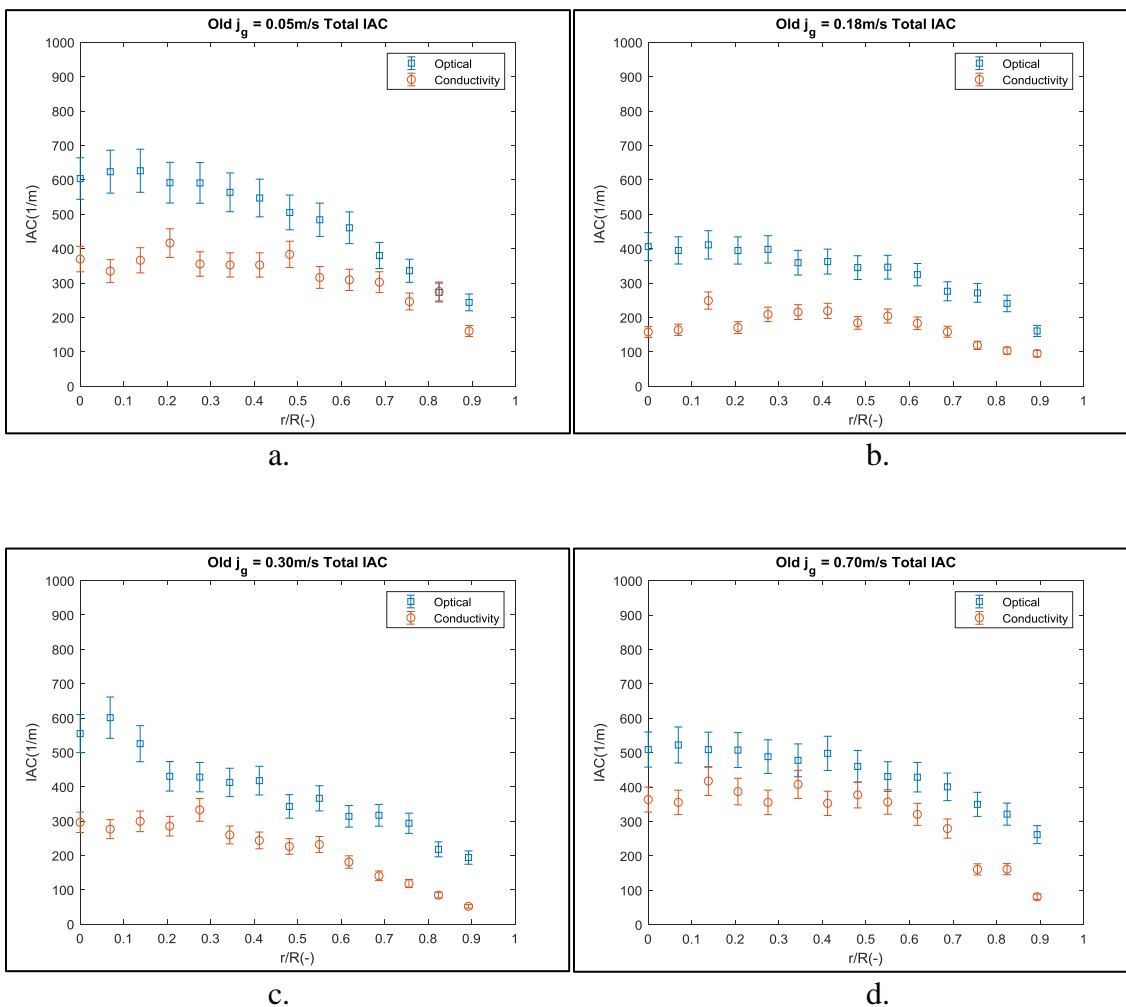Figure 5.17. Original Optical and Conductivity Total IAC for jg = 0.05 (a), 0.18 (b), 0.30 (c), and 0.7 (d) m/s

Table 5.12. Original Optical and Conductivity Total IAC for jg of 0.05 (V1), 0.18 (V2), 0.30 (V3), and 0.7 (V4) m/s Percent Error

r/R	V1	V2	V3	V4
(-)	(%)	(%)	(%)	(%)
0	38.79	61.17	46.55	28.54
0.069	46.34	58.41	54.00	31.98
0.138	41.54	39.42	43.03	17.94
0.206	29.67	56.78	33.73	23.76
0.275	39.89	47.49	22.28	27.25
0.344	37.46	39.97	37.07	14.62
0.412	35.58	39.53	41.67	29.17
0.481	24.12	46.59	34.02	18.05
0.55	34.65	40.99	36.67	17.14
0.618	32.87	43.61	42.38	25.21
0.687	20.44	42.60	55.57	30.29
0.756	26.62	56.14	59.73	54.05
0.824	1.07	57.08	61.24	49.77
0.893	34.12	40.94	73.32	69.03

5.3.2. Old and New Version Conductivity Bubble Comparison. To check the accuracy of the new algorithm a benchmark is necessary. There are a few modifications in the new algorithm that will change the IAC and in the system. For the conductivity probe, there should be an increase in the VF for the new algorithm. The grouping of bubbles based

on the diameter will be implemented. To determine the change in size of the bubbles,

Figure 5.18 displays all effective group 1 bubbles. For the first bubble velocity a

distinguishable shift is seen for all bubbles.
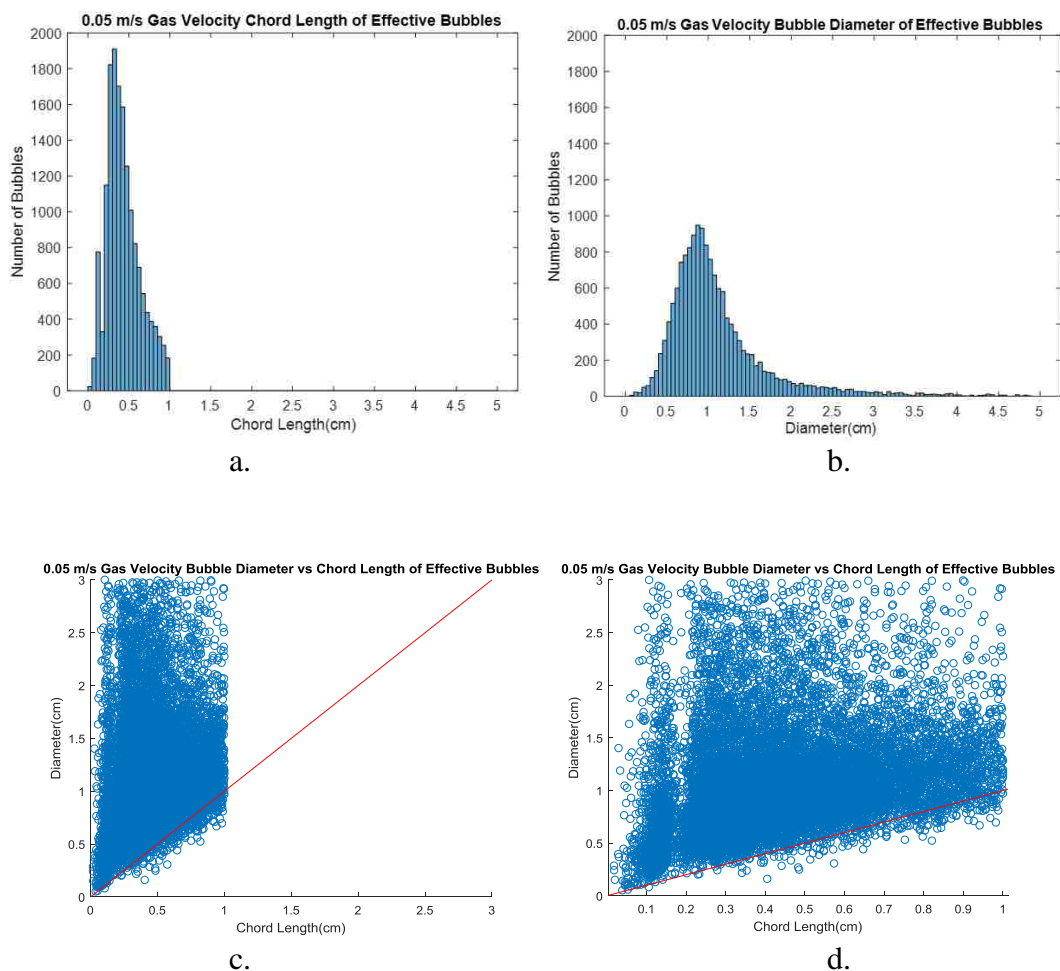
Figure 5.18. Conductivity Effective Group 1 Bubbles PDF Before (a) PDF After (b)
Bubble Diameter vs. Chord Length for jg of 0.05 m/s

In Figure 5.18c and Figure 5.18d There is a small amount of bubbles that fall below

the chord length. This reduction is due to a few item. First due to the estimation by using

the TRDLM there will be an error associated that can cause a fluctuation in the results. In

addition, since distorted bubbles are not spherical in shape even after averaging the three probes the wobble of the bubble will cause some to have a smaller diameter. Figure 5.19 contains the bubble diameter and chord length for a gas velocity of 0.18 m/s. A few additional bubbles fall below the chord length but are consistently distorted bubbles.
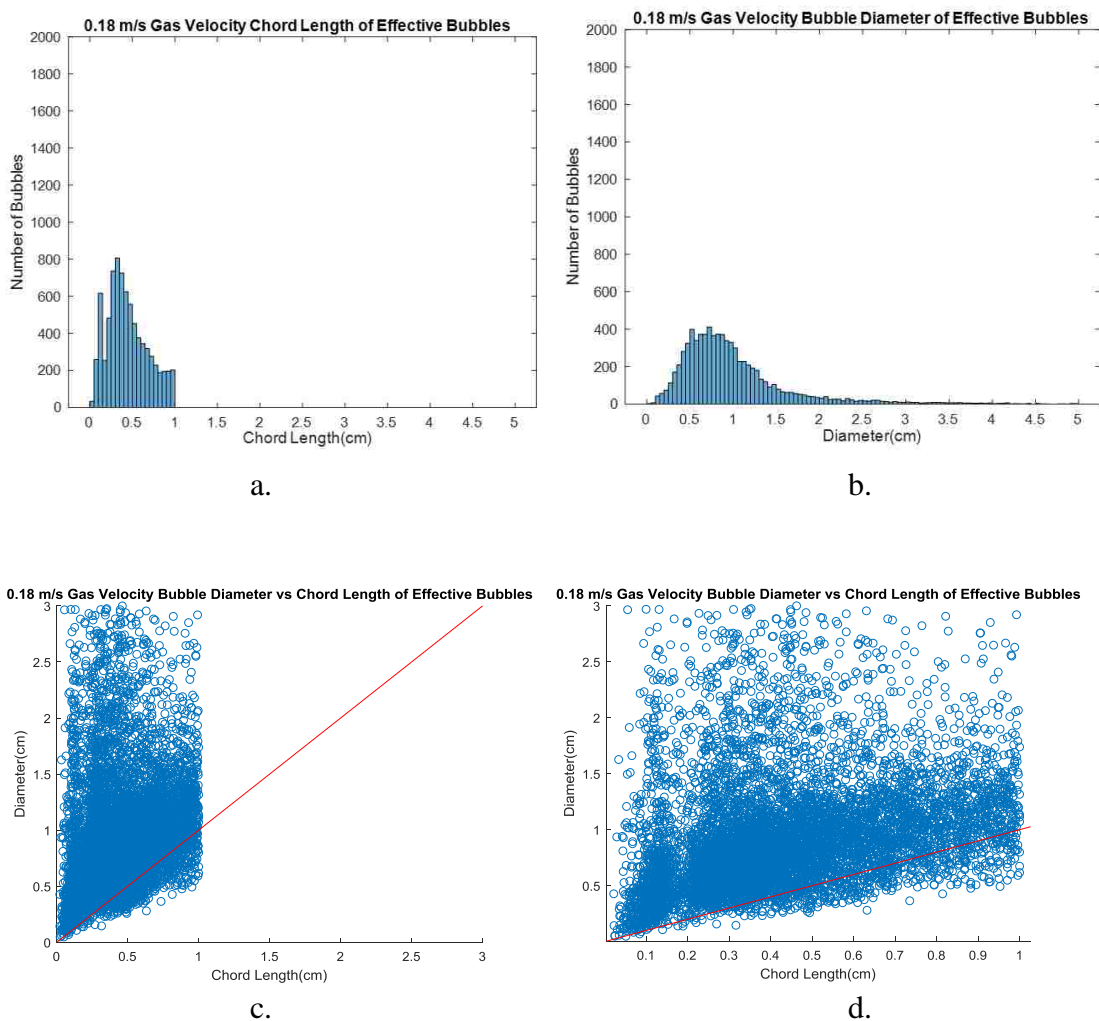
Figure 5.19. Conductivity Effective Group 1 Bubbles PDF Before (a) PDF After (b) Bubble Diameter vs. Chord Length for jg of 0.18 m/s

Figure 5.20 contains the bubble diameter and chord length for a gas velocity of 0.30 m/s. Figure 5.20 is similar to the previous chord length and bubble diameter figures.
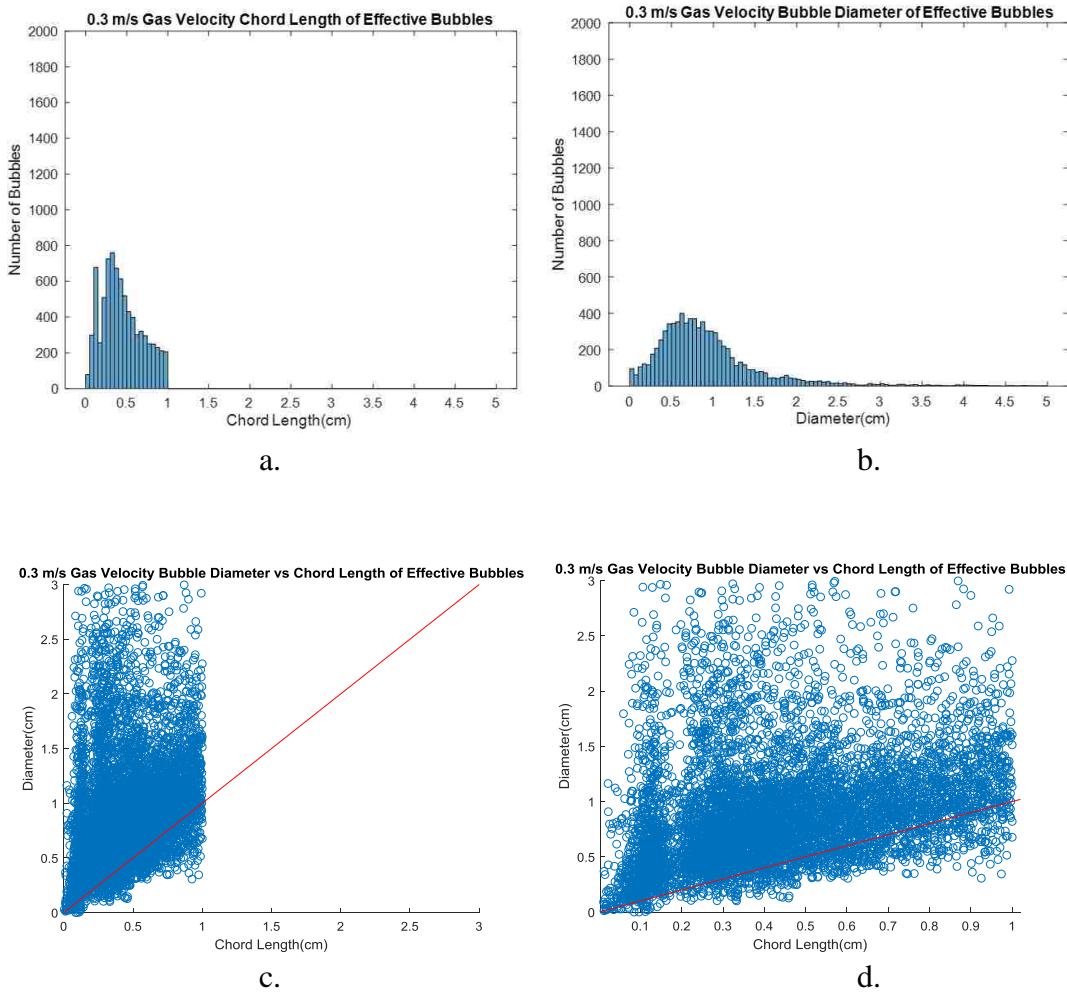
Figure 5.20. Conductivity Effective Group 1 Bubbles PDF Before (a) PDF After (b) Bubble Diameter vs. Chord Length for jg of 0.30 m/s

Figure 5.21 contains the final gas velocity of 0.7 m/s. The last graph is consistent with Figure 5.18-5.20.
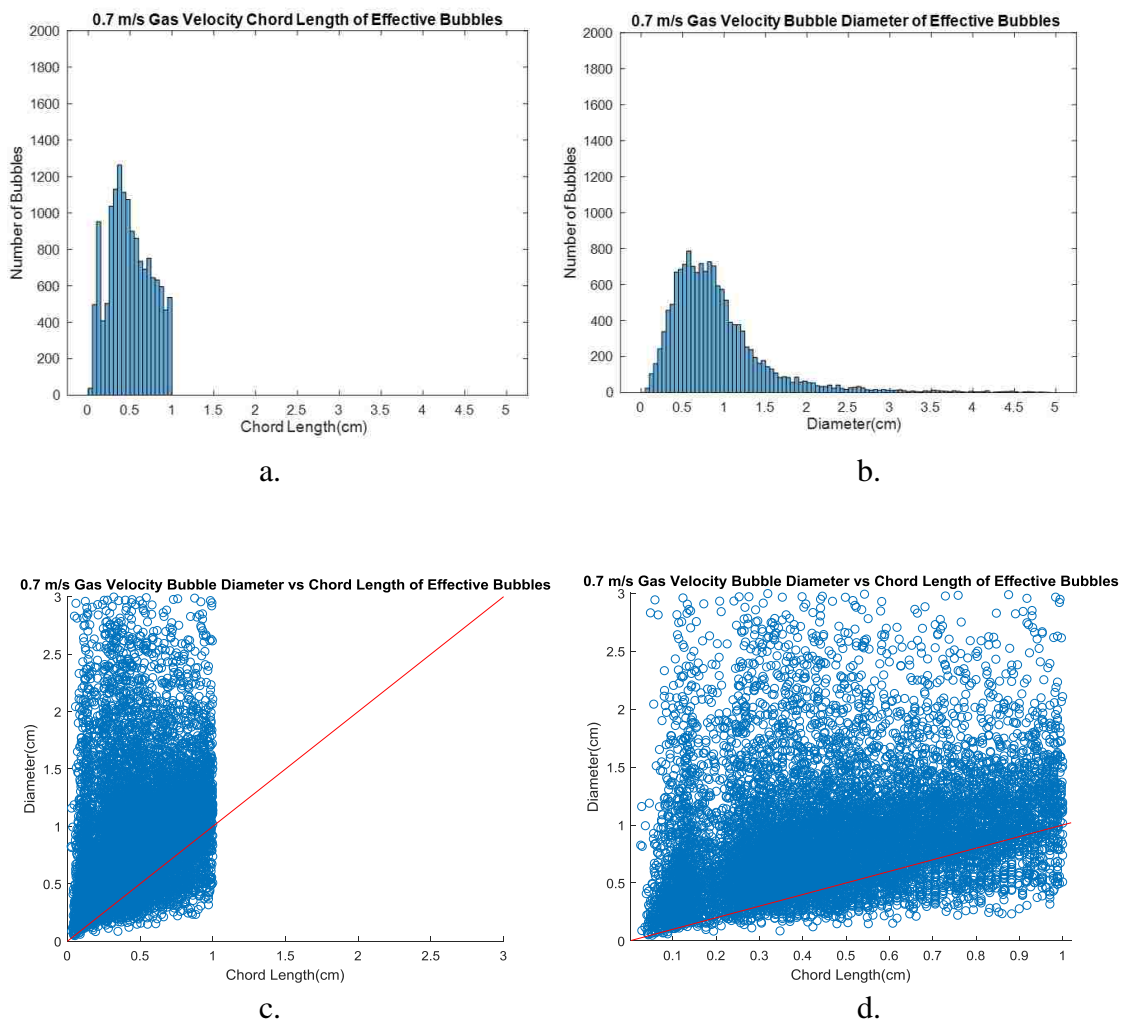
Figure 5.21. Conductivity Effective Group 1 Bubbles PDF Before (a) PDF After (b) Bubble Diameter vs. Chord Length for jg of 0.7 m/s

Table 5.13 contains the percent error of the bubbles as they are shifted into group 2. For Most cases at least 30% of group 1 bubbles are shifted into group 2. These new bubbles will cause a change in the average IAC used to calculate the IAC for the missing bubbles in the system. Therefore a change for the IAC will occur in the new version of the data processing algorithm.

Table 5.13. Conductivity Group 1 Bubbles Percent Error Chord vs. Diameter for jg of 0.05 (V1), 0.18 (V2), 0.30 (V3), and 0.7 (V4) m/s

r/R	V1	V2	V3	V4
(-)	(%)	(%)	(%)	(%)
0	41.94	32.27	48.69	27.60
0.069	43.80	34.80	34.36	44.14
0.138	45.36	33.41	40.52	29.93
0.206	46.48	35.79	37.01	38.25
0.275	46.32	36.30	28.68	35.33
0.344	44.13	28.59	35.78	29.47
0.412	47.59	55.81	33.84	29.66
0.481	47.63	41.79	34.90	31.83
0.55	47.95	38.66	37.95	32.68
0.618	52.08	39.21	36.47	35.53
0.687	52.93	41.79	35.55	35.29
0.756	48.14	40.33	37.10	40.70
0.824	54.10	35.17	43.18	36.16
0.893	36.07	70.37	37.50	38.36

Figure 5.22 is the comparison between the old and new algorithm for the conductivity probe. In Figure 5.22a, the group 1 VF is similar to each other. Figure 5.22b, the old code has a larger group 1 VF, and in Figure 5.22c the new code has a larger group

1 VF. Figure 5.22d the two algorithms are close to one another near the center however the

VF is smaller for the old algorithm as the probe nears the wall.

Figure 5.22. New and Old Conductivity Group 1 Void Fraction for Gas Velocities 0.05 (a), 0.18 (b), 0.30 (c), and 0.7 (d) m/s

Table 5.14 contains the percent error between the old and new algorithms for group

1 VF. The largest deviation between the two methods is near the wall where the number of

bubbles collected are reduced. The decrease in VF is due to the missed bubbles that are

near the wall. As the group 1 VF nears the center of the bubble column, the group 1 VF produce similar results.

Table 5.14. Conductivity Probe Group 1 VF for jg of 0.05, 0.18, 0.30 and 0.7 m/s Respectively Per Second Relative Error

r/R	V1	V2	V3	V4
(-)	(%)	(%)	(%)	(%)
0	7.48	52.59	51.79	14.52
0.069	10.97	38.15	54.20	13.34
0.138	3.20	26.48	48.59	9.30
0.206	9.91	28.14	59.47	11.08
0.275	6.17	28.98	38.55	14.01
0.344	7.30	39.14	76.52	8.76
0.412	2.20	34.41	52.85	8.09
0.481	11.19	33.13	33.10	15.03
0.55	1.09	34.59	43.56	22.15
0.618	0.46	35.93	63.77	38.62
0.687	4.30	43.34	115.72	46.98
0.756	26.72	43.65	120.00	69.24
0.824	13.56	48.17	178.93	329.96
0.893	76.29	49.82	445.54	136.55

Figure 5.23 contains the group 2 VF for the conductivity probe at the 14 radial positions for the gas velocity of 0.05, 0.18, 0.3, and 0.7 m/s. For Figure 5.23a, the VF is

much higher for group 2 bubbles due to the shift of bubbles from group 1 into group 2.

Figure 5.23b, Figure 5.23c, and Figure 5.23d produce similar results to one another in VF,

with fluctuation of lower and higher values in each of the figures. Changes in the group 2

bubbles are due to the bubbles placed into group 2 from group 1.

Figure 5.23. New and Old Conductivity Group 2 Void Fraction for jg of 0.05 (a), 0.18 (b), 0.30 (c), and 0.7 (d) m/s

Table 5.15 contains the percent error between the two algorithms. The largest deviations are at the gas velocity of 0.05 m/s where many group 1 bubbles appear and are pushed into group 2 from group 1 in the new algorithm.

Table 5.15. Conductivity Probe Group 2 VF for jg of 0.05 (V1), 0.18 (V2), 0.30 (V3), and 0.7 (V4) m/s Percent Error

r/R	V1	V2	V3	V4
(-)	(%)	(%)	(%)	(%)
0	145.49	14.63	15.09	24.68
0.069	210.18	3.96	12.85	16.54
0.138	220.98	7.06	8.22	13.51
0.206	222.71	9.85	12.45	14.53
0.275	180.43	6.39	18.96	18.49
0.344	188.38	12.43	10.80	19.19
0.412	185.89	7.04	1.44	25.24
0.481	281.92	23.69	6.73	9.77
0.55	258.24	6.15	12.15	16.71
0.618	213.84	13.44	6.32	16.73
0.687	297.77	24.16	17.32	1.93
0.756	206.13	35.89	19.86	8.40
0.824	146.72	27.01	65.02	55.80
0.893	79.21	59.89	265.02	119.11

Figure 5.24 contains the total VF for the system. For all four velocities near the wall the new algorithm has a much higher VF. As the probe near probe nears the center of the bubble column the difference decreases.

a.

b.

b.

c.

d.
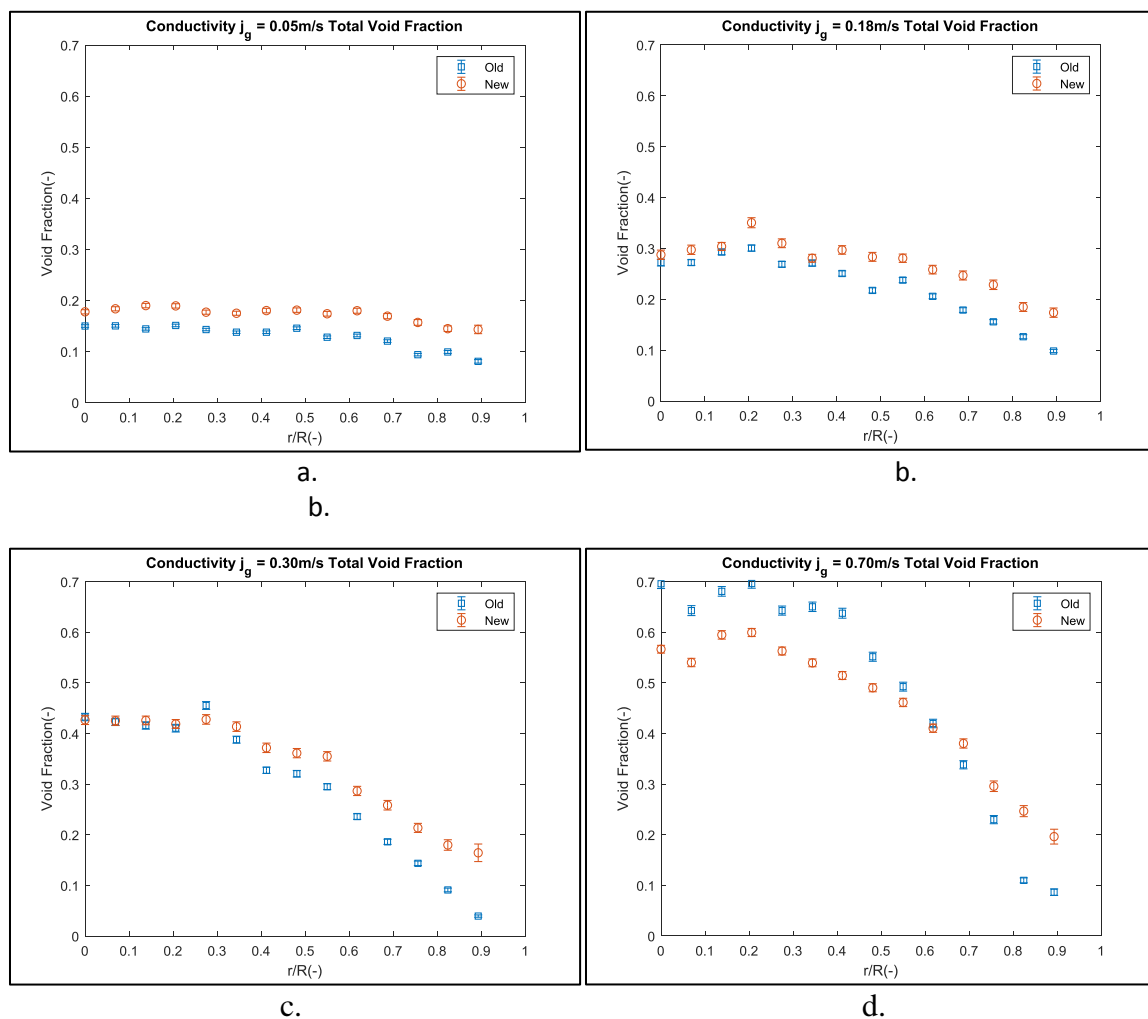
Figure 5.24. New and Old Conductivity Total Void Fraction for jg of 0.05 (a), 0.18 (b), 0.30 (c), and 0.7 (d) m/s

In Table 5.16 the percent error for the total VF for all four velocities is presented. To determine the accuracy of the VF for the new algorithm a comparison between the

optical probe is necessary. The fast response time of the optical probe will help determine if the new algorithm is picking up the right amount of bubbles in the system and if the bubbles that are collected are similar in size to the to the optical probe.

Table 5.16. Conductivity Probe Total VF for jg of 0.05 (V1), 0.18 (V2), 0.30 (V3), and 0.70 (V4) m/s Percent Error

r/R	V1	V2	V3	V4
(-)	(%)	(%)	(%)	(%)
0	18.55	5.62	1.32	18.58
0.069	22.24	9.22	0.54	15.96
0.138	31.69	3.72	2.40	12.63
0.206	25.36	16.60	2.02	13.90
0.275	23.78	15.36	6.04	12.43
0.344	26.92	3.54	6.65	17.03
0.412	30.70	18.47	13.56	19.30
0.481	24.31	30.36	12.69	11.11
0.55	35.86	18.09	20.33	6.33
0.618	36.83	25.51	21.43	2.21
0.687	40.53	38.03	38.83	12.44
0.756	67.27	46.76	48.71	28.71
0.824	46.01	46.20	97.48	124.48
0.893	77.45	76.70	316.46	126.94

Figure 5.25 contains the group 1 IAC for the conductivity probe for both algorithms the newer algorithm picks up a larger amount of bubbles and therefore the IAC is larger for the new algorithm. The IAC in the system for group 1 bubbles is around twice the amount of the previous algorithm.
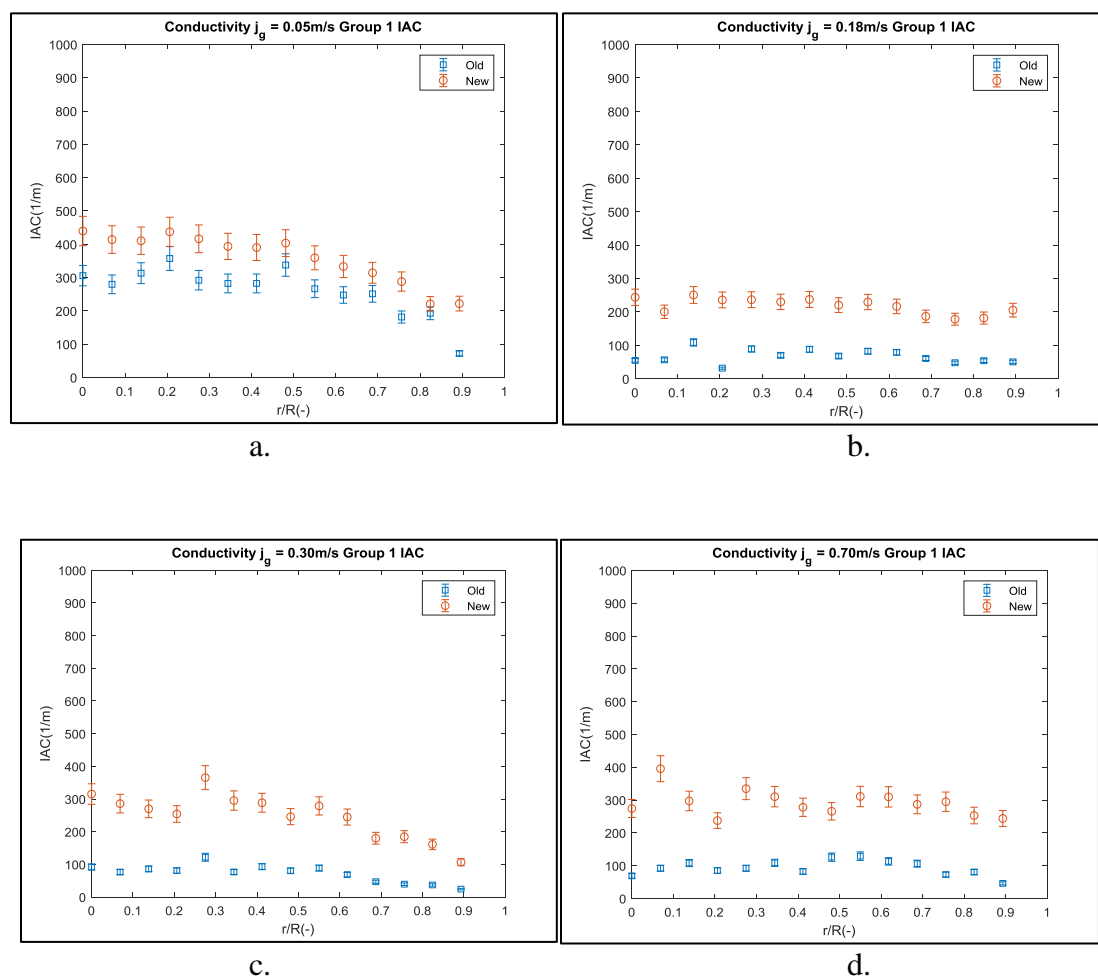
Figure 5.25. New and Old Conductivity Group 1 IAC for jg of 0.05 (a), 0.18 (b), 0.30 (c), and 0.7 (d) m/s

Table 5.17 contains the percent error for the conductivity probe comparison of group 1 IAC. The largest deviation to the two algorithms is near the wall of the bubble

column where fewer bubbles are present and therefore less smaller bubbles are picked up by the conductivity probe. Both algorithms however follows similar trends to one another based on the location of the probe.

Table 5.17. Conductivity Probe Group 1 IAC for jg of 0.05 (V1), 0.18 (V2), 0.30 (V3), and 0.7 (V4) m/s Percent Error

r/R	V1	V2	V3	V4
(-)	(%)	(%)	(%)	(%)
0	43.80	343.35	242.57	297.58
0.069	48.05	253.67	273.64	329.68
0.138	31.12	130.74	213.38	175.01
0.206	22.42	643.04	213.80	178.53
0.275	42.54	165.72	199.92	263.49
0.344	39.41	228.26	284.76	185.58
0.412	38.22	169.49	210.07	237.63
0.481	19.48	224.68	205.54	110.91
0.55	34.82	178.67	214.54	141.01
0.618	34.61	173.93	256.68	173.89
0.687	25.13	207.09	283.52	170.37
0.756	58.69	271.84	368.81	304.57
0.824	14.52	235.32	334.15	213.48
0.893	207.28	306.91	339.80	429.69

Figure 5.26 contains the group 2 IAC for the conductivity probe for the 14 radial positions for the gas velocity of 0.05, 0.18, 0.3, and 0.7 m/s. Each of the plots follow a similar pattern to the group 1 IAC. This is because a large portion of the bubbles are transferred to group 2 from group 1 and therefore the IAC in group 2 will increase.
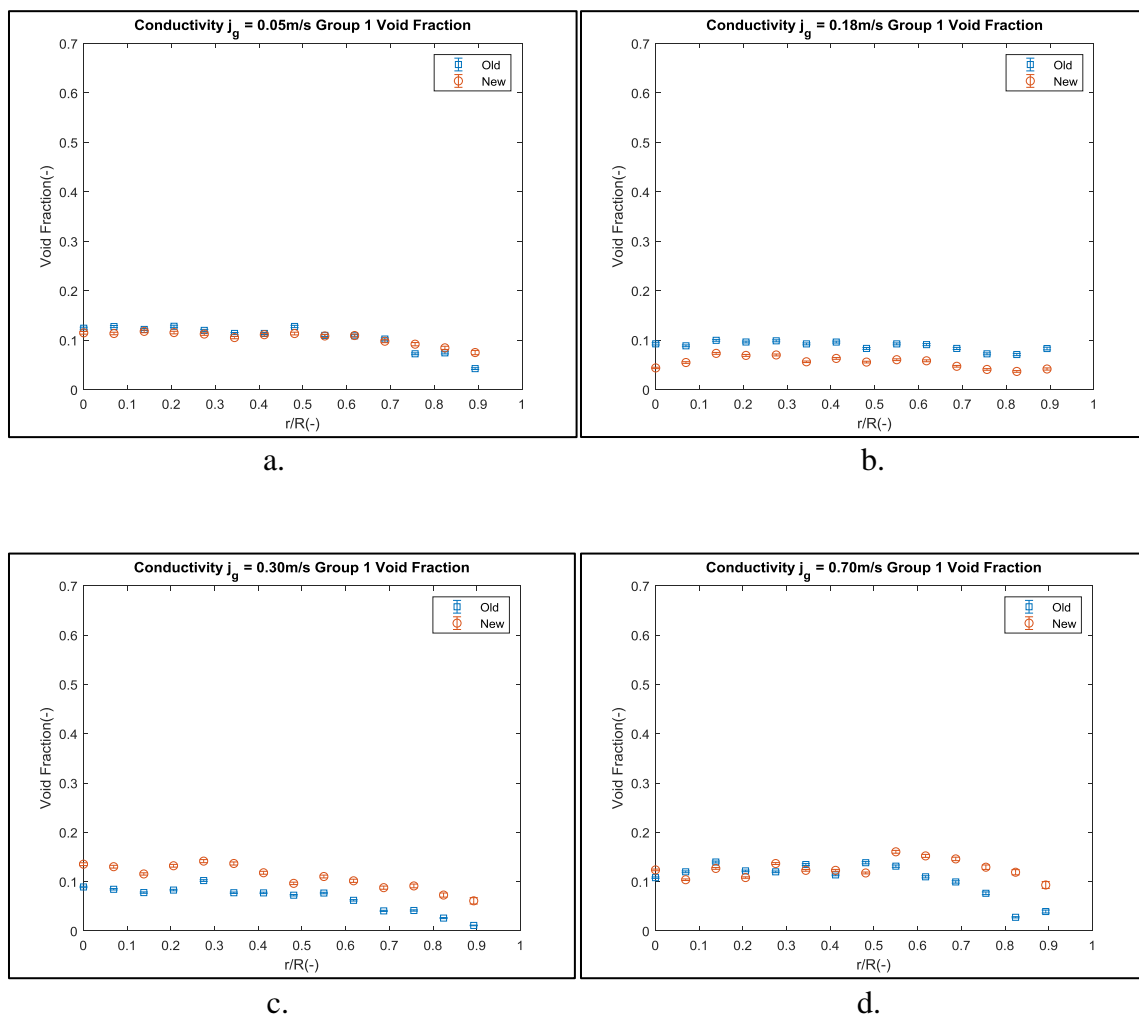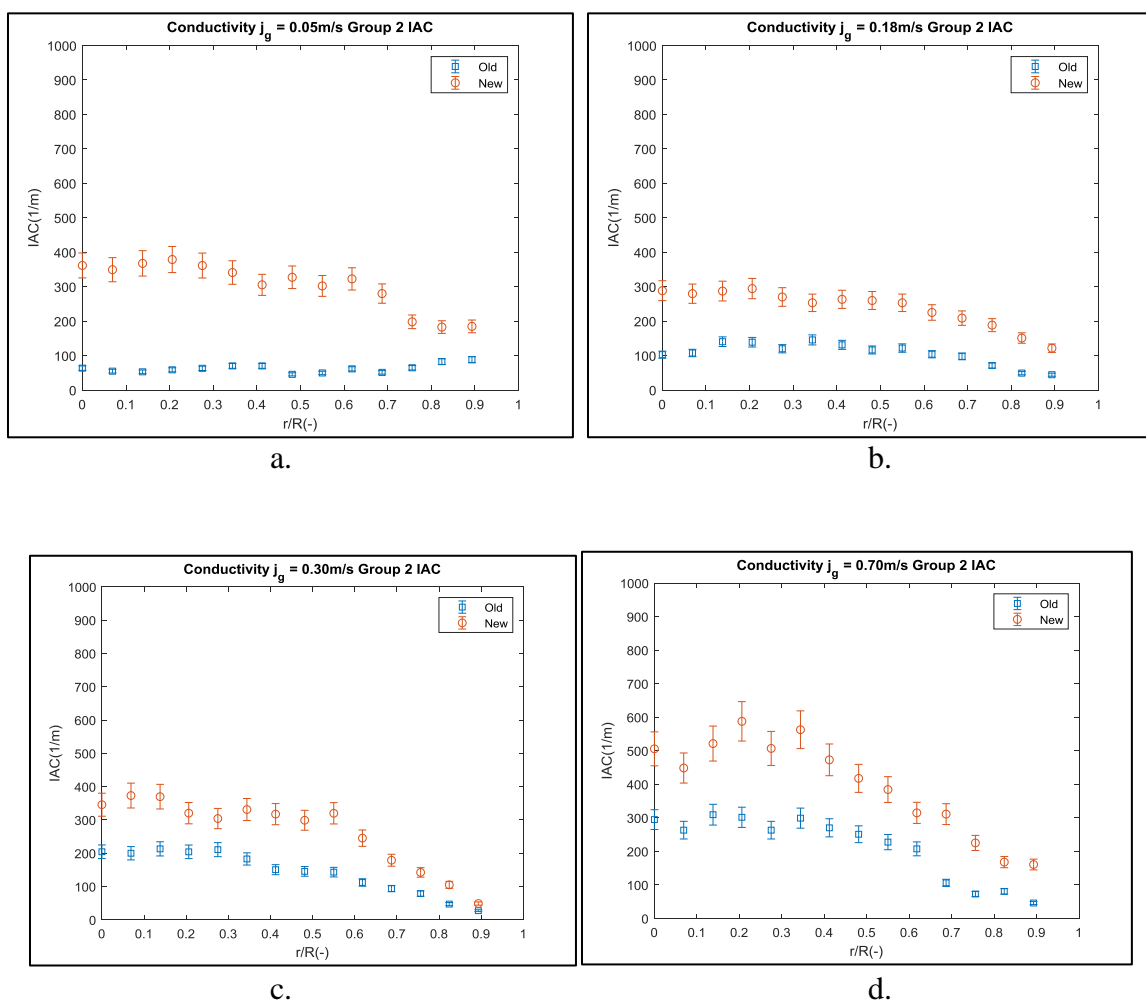

Figure 5.26. New and Old Conductivity Group 2 IAC for jg of 0.05 (a), 0.18 (b), 0.30 (c), and 0.7 (d) m/s

Table 5.18 contains the percent error for the conductivity probe group 2 IAC. The largest difference for the IAC is in the 0.05 m/s gas velocity where largest amount of

bubbles that are missed by the conductivity probe. The missed bubbles for both group 1 and group 2 will be transferred over to the total IAC and this will cause a large deviation between the two algorithms for the IAC in the bubble column.

Table 5.18. Conductivity Probe Group 2 IAC for jg of 0.05 (V1), 0.18 (V2), 0.30 (V3), and 0.7 (V4) m/s Percent Error

r/R	V1	V2	V3	V4
(-)	(%)	(%)	(%)	(%)
0	467.52	181.04	69.10	71.63
0.069	535.54	160.07	86.63	70.40
0.138	592.64	104.67	73.55	68.56
0.206	543.04	112.08	56.87	94.86
0.275	471.86	125.33	44.31	92.57
0.344	385.77	73.98	81.16	88.15
0.412	334.83	100.72	110.74	74.97
0.481	615.09	123.46	105.42	66.39
0.55	506.66	107.80	123.27	68.83
0.618	423.35	116.60	118.76	51.75
0.687	444.93	113.76	90.73	193.04
0.756	205.61	164.92	80.66	208.89
0.824	121.22	206.97	122.32	108.29
0.893	109.23	172.82	78.32	249.28

The total IAC for each of the bubble velocities are displayed in Figure 5.27. Each of the plots in Figure 5.27 have a large deviation between the IAC for each of the different gas velocities. This starts to display the importance on correct bubble size when calculating local parameters.
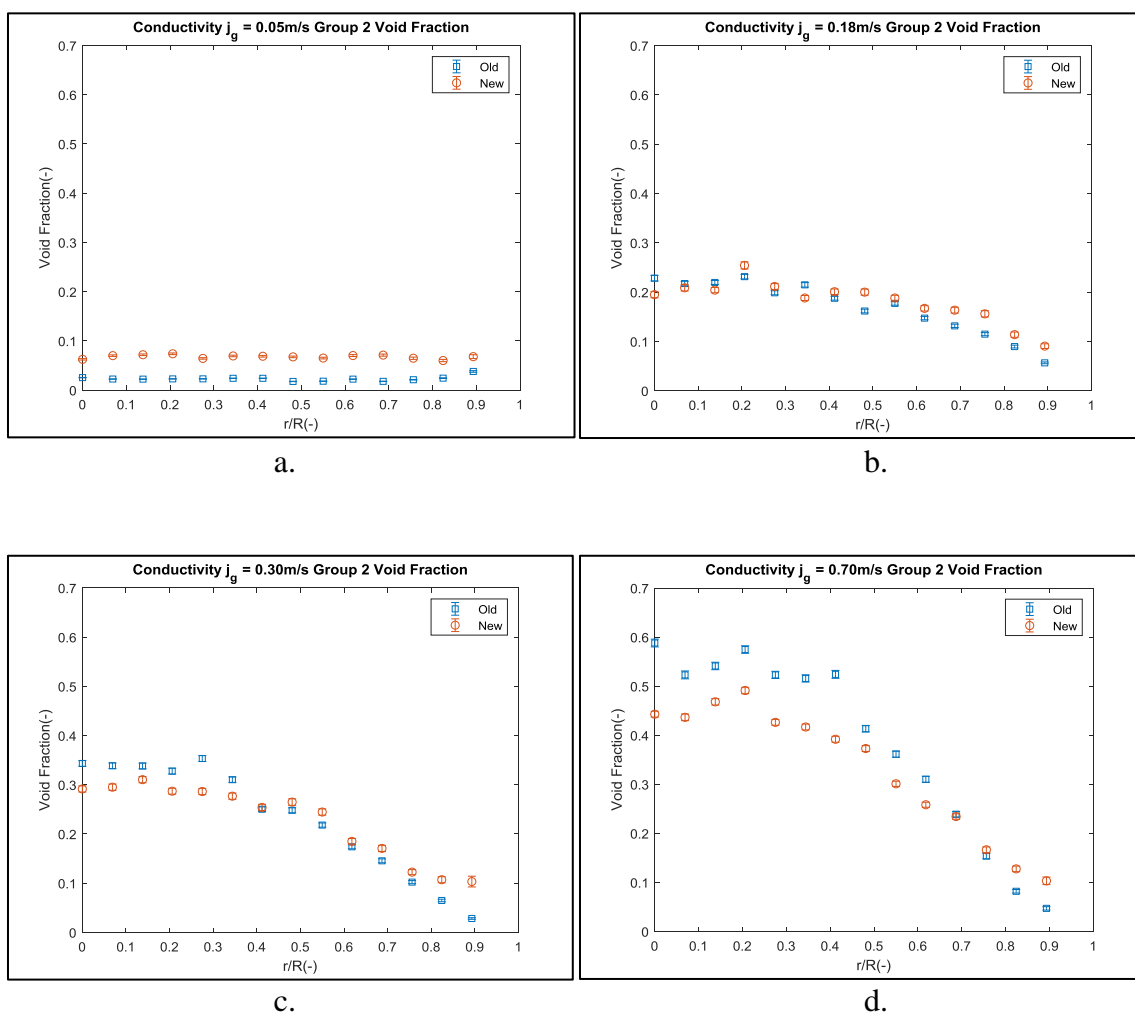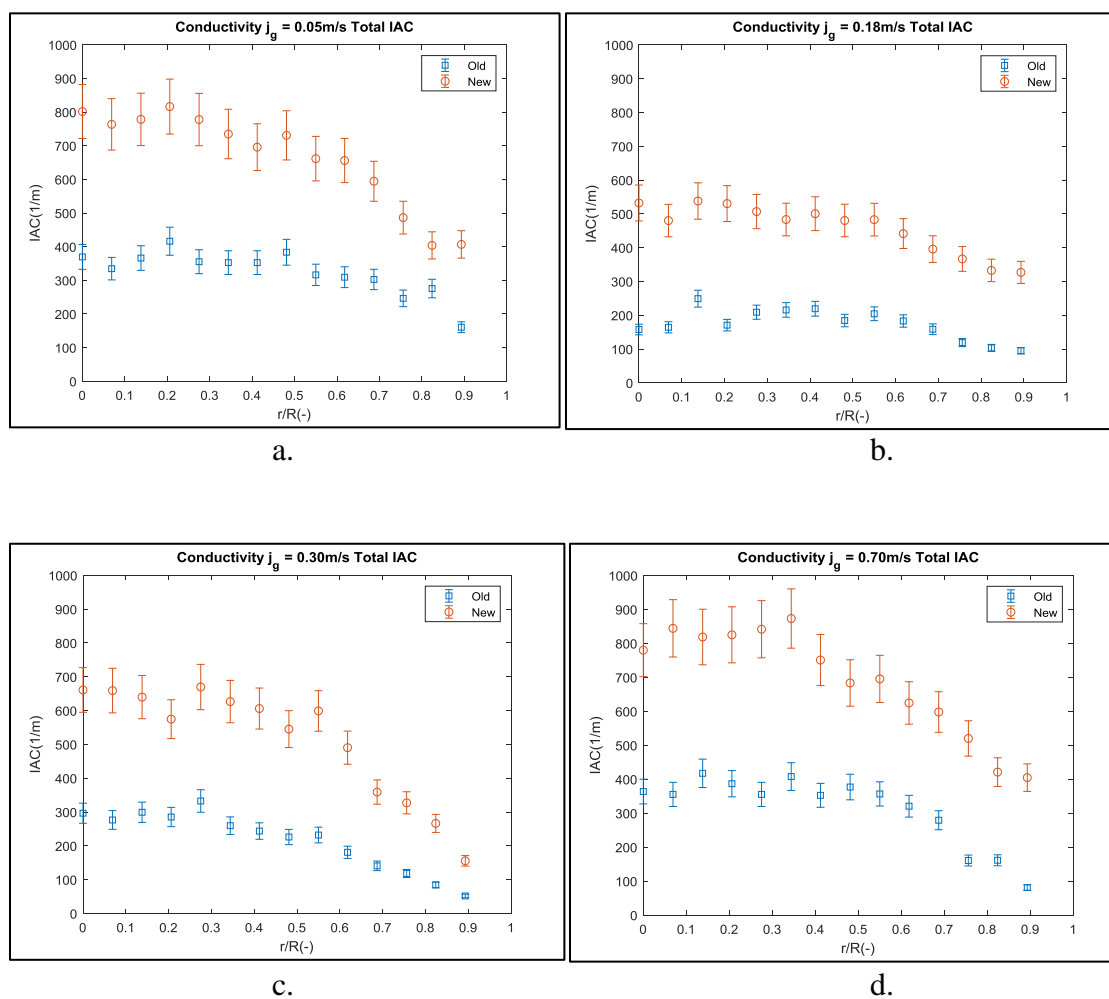

Figure 5.27. New and Old Conductivity Total IAC for jg of 0.05 (a), 0.18 (b), 0.30 (c), and 0.7 (d) m/s

Table 5.19 has the percent error between the old and new algorithm for the conductivity probe at each radial location. The largest difference in IAC is close to the wall

which is to be expected due to the large difference in the VF discovered. Locations away from the wall increase along with the number of bubbles at each location.

Table 5.19. Conductivity Probe Total IAC for jg of 0.05 (V1), 0.18 (V2), 0.30 (V3), and 0.7(V4) m/s Percent Error

r/R	V1	V2	V3	V4
(-)	(%)	(%)	(%)	(%)
0	116.90	237.65	122.93	114.48
0.069	128.14	192.37	138.40	137.61
0.138	112.54	116.05	113.79	96.12
0.206	96.15	210.89	101.45	113.30
0.275	118.93	142.55	101.33	136.88
0.344	108.41	124.13	141.37	114.12
0.412	97.32	128.34	148.68	112.95
0.481	90.61	160.77	141.09	81.26
0.55	109.18	136.40	158.16	94.95
0.618	112.12	141.36	171.14	94.84
0.687	96.47	149.59	154.99	114.13
0.756	97.37	207.97	176.70	223.69
0.824	46.55	221.80	215.51	160.87
0.893	153.32	244.05	200.99	399.42

5.3.3. Old and New Version Optical Bubble Comparison. To benchmark the new signal processing algorithm the optical probe will be the most accurate at 22kHz sampling

rate. Each of the values for the VF and IAC will be much closer to one another with the largest deviation found due to grouping the bubbles based upon chord length or bubble diameter. Figure 5.28 shows to chord length and diameter for the gas velocity of 0.05 m/s. The shift in bubbles follows a similar pattern to the conductivity probe. The large shift in bubble will not affect the VF in the calculations however it will affect the IAC.
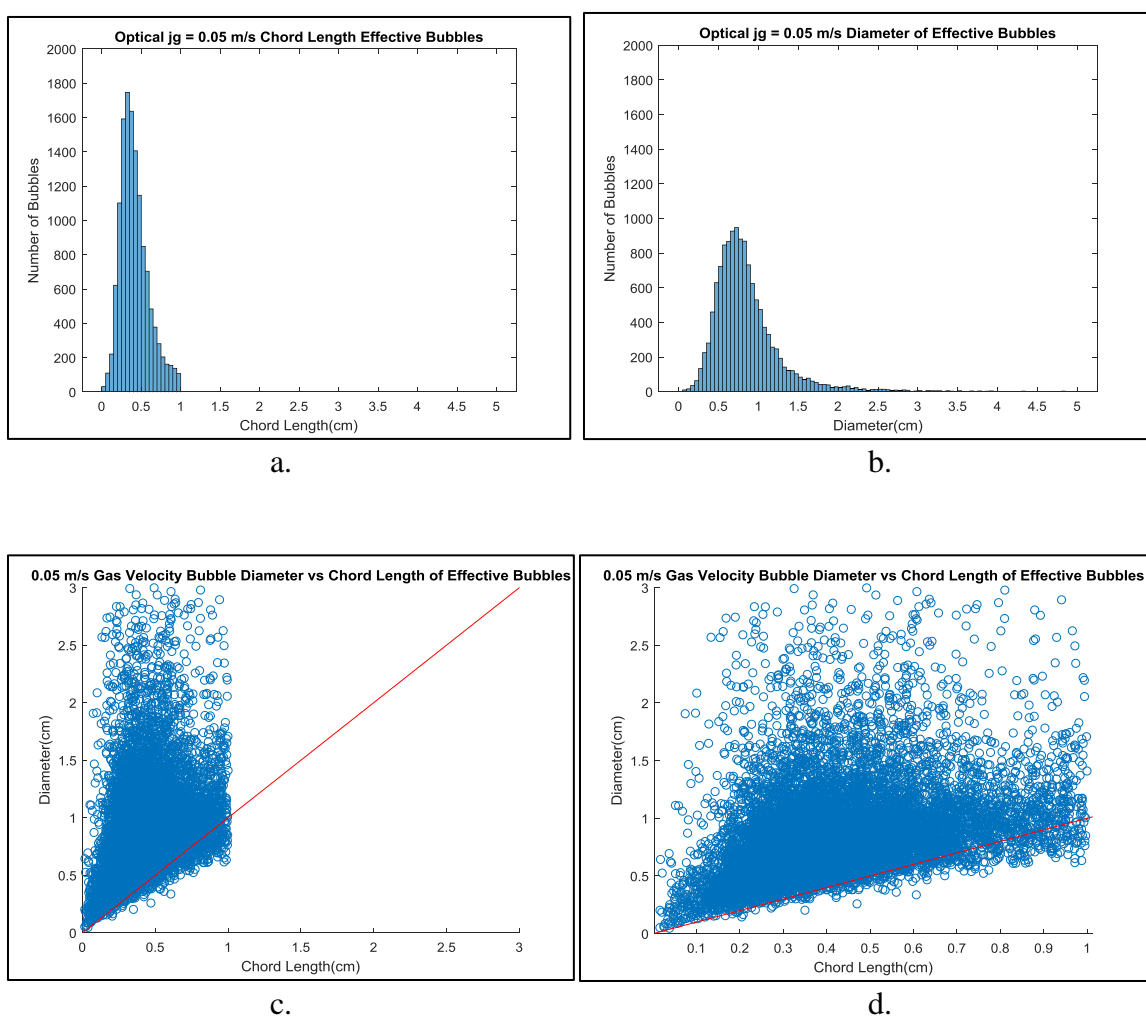
Figure 5.28. Optical Effective Group 1 Bubbles PDF Before (a) PDF After (b) Bubble Diameter vs. Chord Length for jg of 0.05 m/s

Figure 5.29 is the bubble diameter vs. chord length for all radial positions with the use of the optical probe at a gas velocity of 0.18 m/s. There is a larger amount of effective bubbles for the optical probe. However, a smaller amount of bubbles is placed in to group 2 from group 1. The bubble size distribution found from 29b is similar to the patterns found for all conductivity probe chord length vs. bubble diameter graphs.
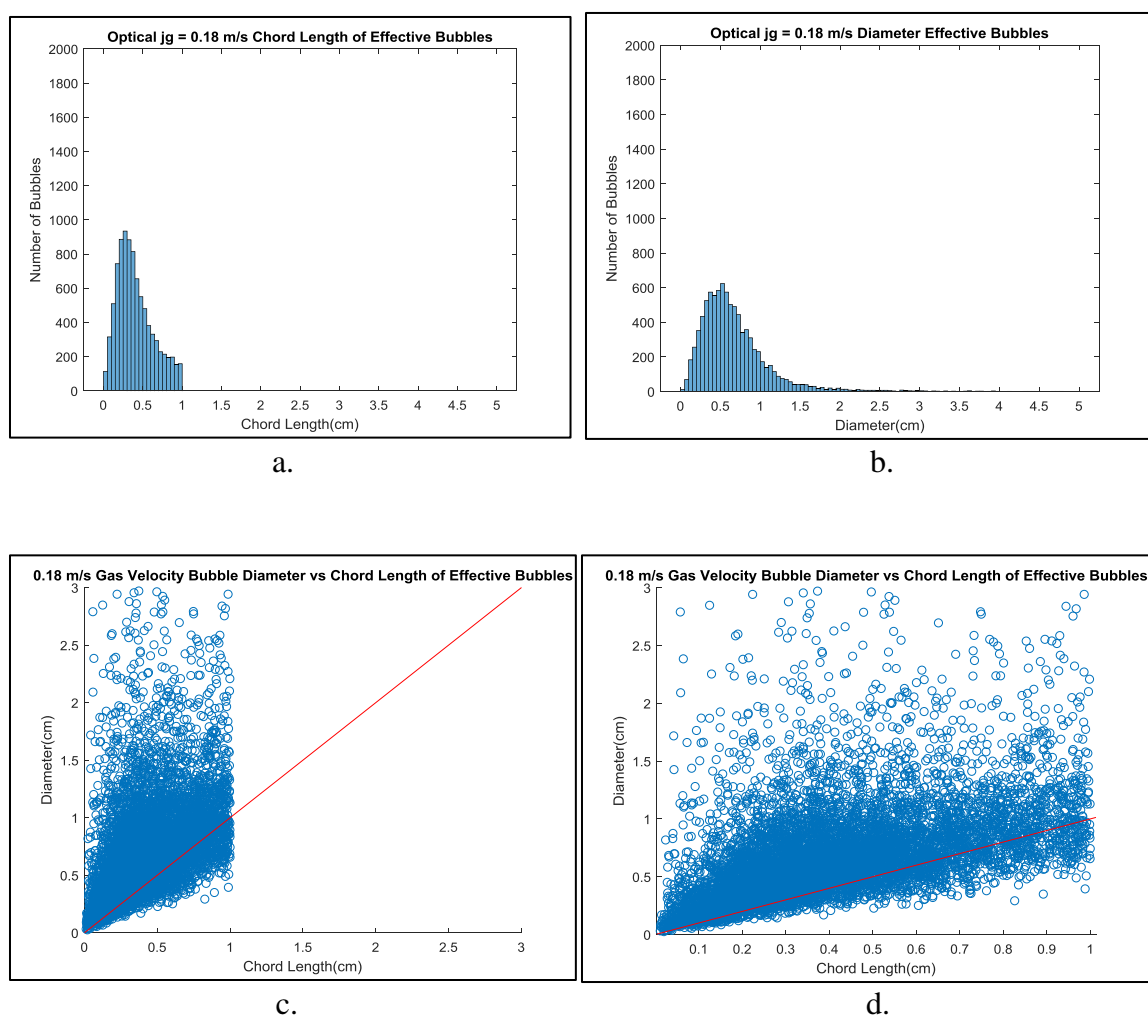
Figure 5.29. Optical Effective Group 1 Bubbles PDF Before (a) PDF After (b) Bubble Diameter vs. Chord Length for jg of 0.18 m/s

Figure 5.30 contains the bubble diameter vs. chord length for all radial positions with the use of the optical probe at a gas velocity of 0.30 m/s. Each of the plots follow a similar pattern to the previous 2 velocities with a smaller amount of bubbles shifting into group 2 from group 1. The bubbles that are distorted seem to have a larger amount falling under the chord length.

a.

b.

c.

a.
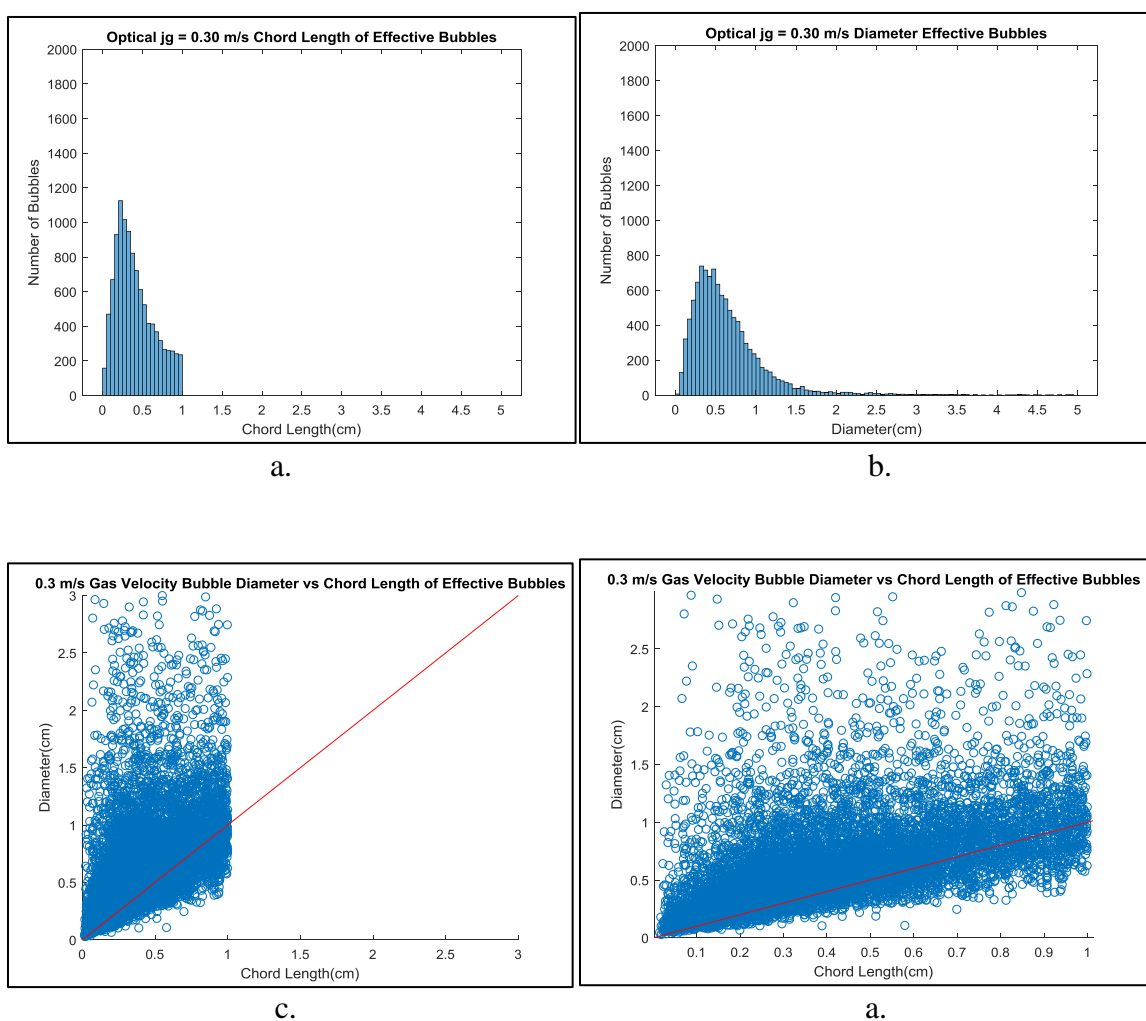
Figure 5.30. Optical Effective Group 1 Bubbles PDF Before (a) PDF After (b) Bubble Diameter vs. Chord Length for jg of 0.30 m/s

Figure 5.31 contains the bubble diameter vs. chord length for all radial positions with the use of the optical probe at a gas velocity of 0.30 m/s the shift for the bubbles in Figure 5.31 is similar to the previous two velocities.
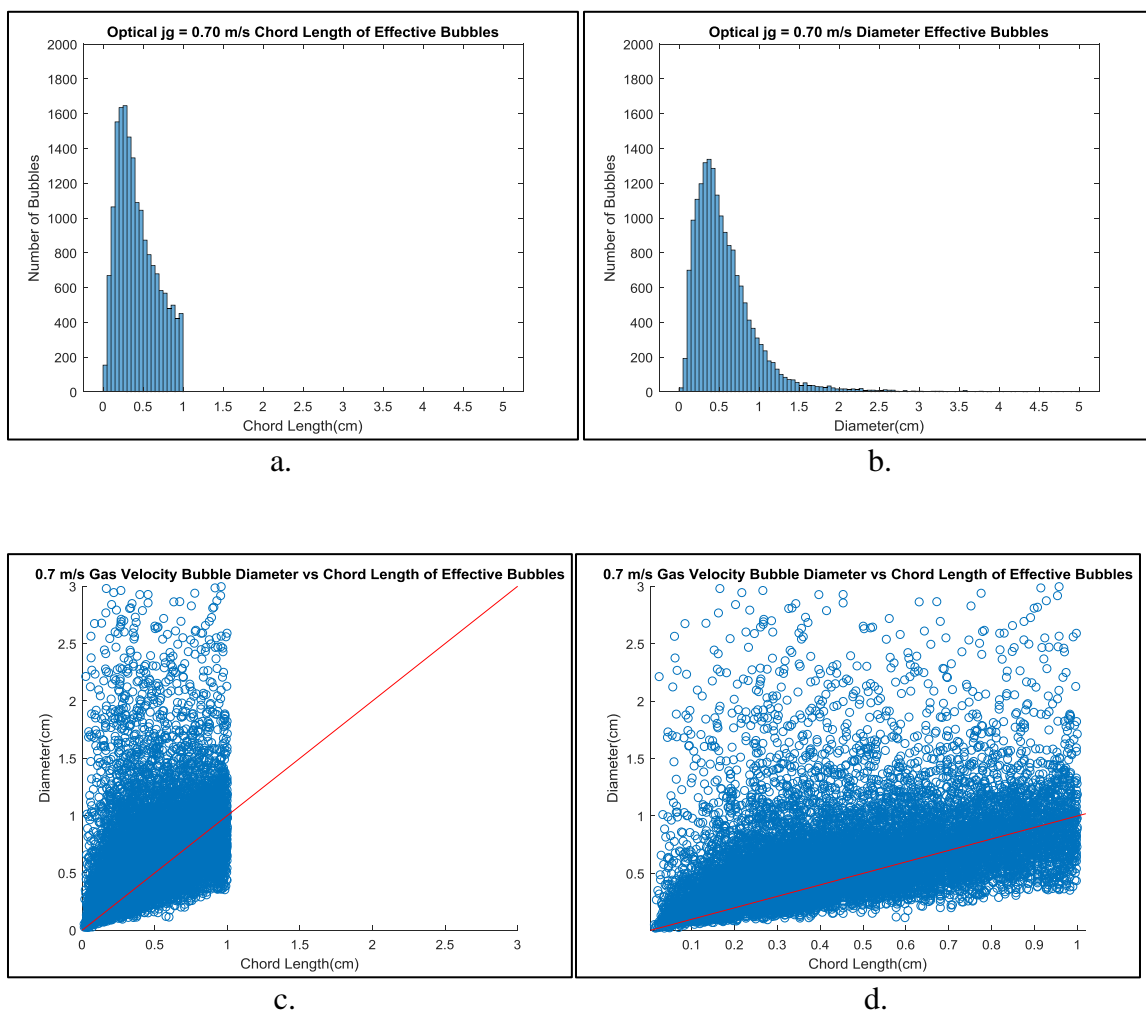
Figure 5.31. Optical Effective Group 1 Bubbles PDF Before (a) PDF After (b) Bubble Diameter vs. Chord Length for jg of 0.70 m/s

For Figures 5.28-5.31 the patters are similar to the conductivity probe with a much smaller deviation between to between algorithms. Table 5.20 contains the percent error between the four velocities for the chord length and bubble diameter. The largest transfer of bubbles is contained within the 0.05 m/s gas velocity and the smallest change is at the highest gas velocity where the most group 2 bubbles are present.

Table 5.20. Optical Group 1 Bubbles Percent Error Chord vs. Diameter for jg of 0.05 (V1), 0.18 (V2), 0.30 (V3), and 0.7 (V4) m/s

r/R	V1	V2	V3	V4
(-)	(%)	(%)	(%)	(%)
0	24.46	16.18	19.21	10.10
0.069	24.70	13.76	14.36	10.14
0.138	25.73	15.61	17.04	9.28
0.206	21.81	16.40	14.23	11.23
0.275	25.07	15.11	13.74	10.23
0.344	24.35	13.68	14.17	10.96
0.412	26.34	16.23	13.92	10.98
0.481	26.55	15.43	12.95	13.48
0.55	24.88	15.99	16.22	11.01
0.618	23.71	13.10	15.96	11.62
0.687	24.42	17.11	15.64	11.75
0.756	14.84	16.63	15.90	12.96
0.824	7.87	15.92	17.99	17.80
0.893	32.19	15.79	13.66	11.31

Figure 5.32 contains the VF for all group 1 bubbles for optical probe for the 14 radial positions at the gas velocities of 0.05, 0.18, 0.3, and 0.7 m/s. The difference between the two algorithms is much smaller. Since both algorithms collect the smaller bubbles effetely the VF should be similar for each case. The slight difference will be due to the small amount of trailing bubbles picked up by the new algorithm will slightly change the VF.
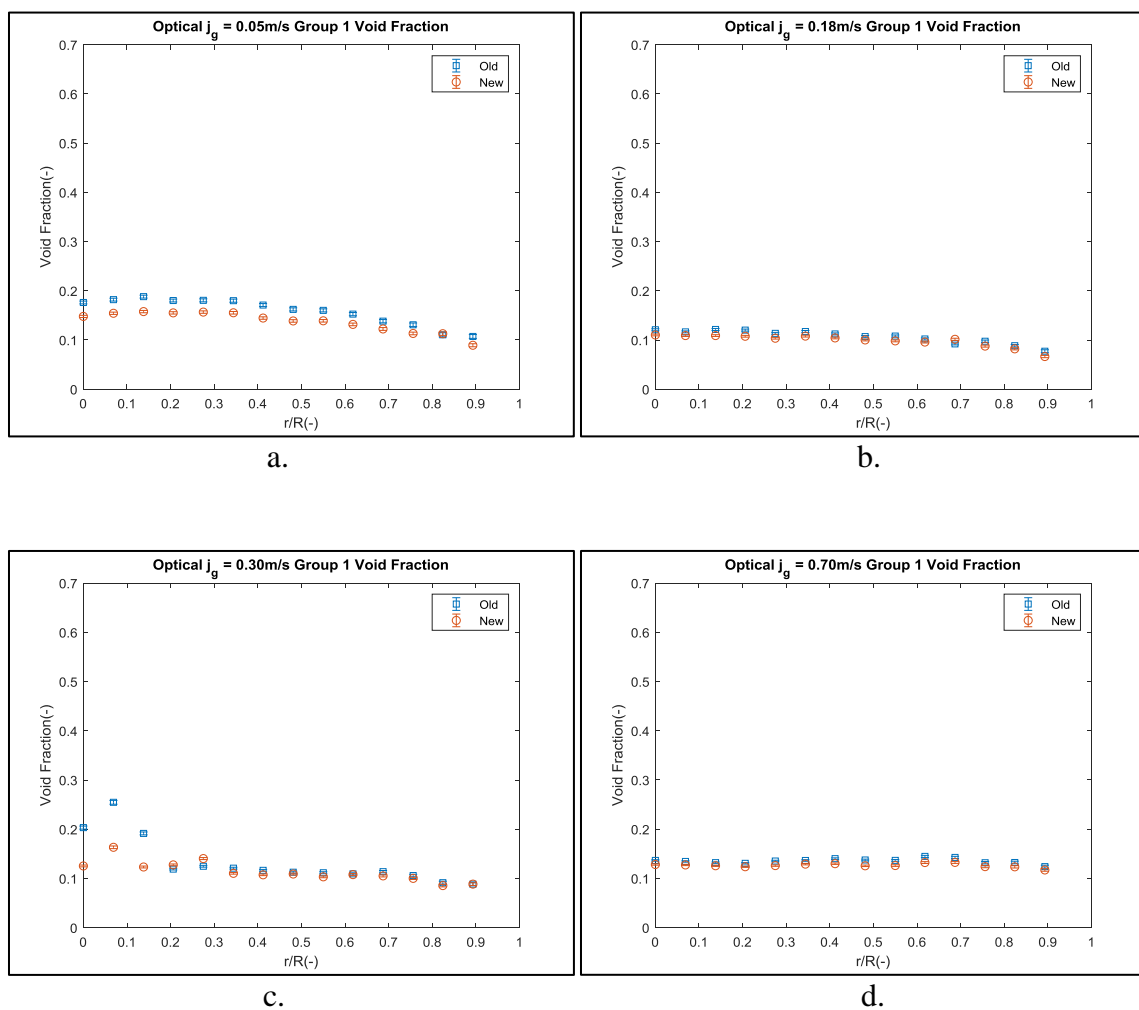

Figure 5.32. New and Old Optical Group 1 VF for jg of 0.05 (a), 0.18 (b), 0.30 (c), and 0.7 (d) m/s

Table 5.21 contains the percent error for group 1 VF. The percent error is around 10% for most values. Most of these deviations are due to the switch from bubble chord length to bubble diameter. The change is most relevant in the 0.05 m/s velocity where the VF is higher for the old algorithm.

Table 5.21. Optical Probe Group 1 VF for jg of 0.05 (V1), 0.18 (V2), 0.30 (V3), and 0.70 (V4) m/s Percent Error

r/R	V1	V2	V3	V4
(-)	(%)	(%)	(%)	(%)
0	16.06	8.77	38.32	6.08
0.069	15.22	6.44	35.89	5.28
0.138	16.16	10.21	35.61	4.77
0.206	13.93	10.41	7.23	5.28
0.275	13.23	8.72	12.50	6.87
0.344	13.67	7.94	8.68	5.43
0.412	15.44	7.21	7.81	7.28
0.481	14.49	6.36	3.28	8.59
0.55	13.23	9.07	7.44	7.69
0.618	13.70	6.17	1.37	8.64
0.687	11.50	10.10	7.56	7.08
0.756	13.45	10.15	5.38	5.99
0.824	1.99	7.24	6.46	6.65
0.893	16.70	13.99	0.11	5.49

Figure 5.33 contains the group 2 VF for the optical probe comparison. The values for each of the plots are similar to one another with the 0.05 m/s gas velocity showing a larger change from group 1 into group 2 for the new algorithm.

a.

b.

c.

d.
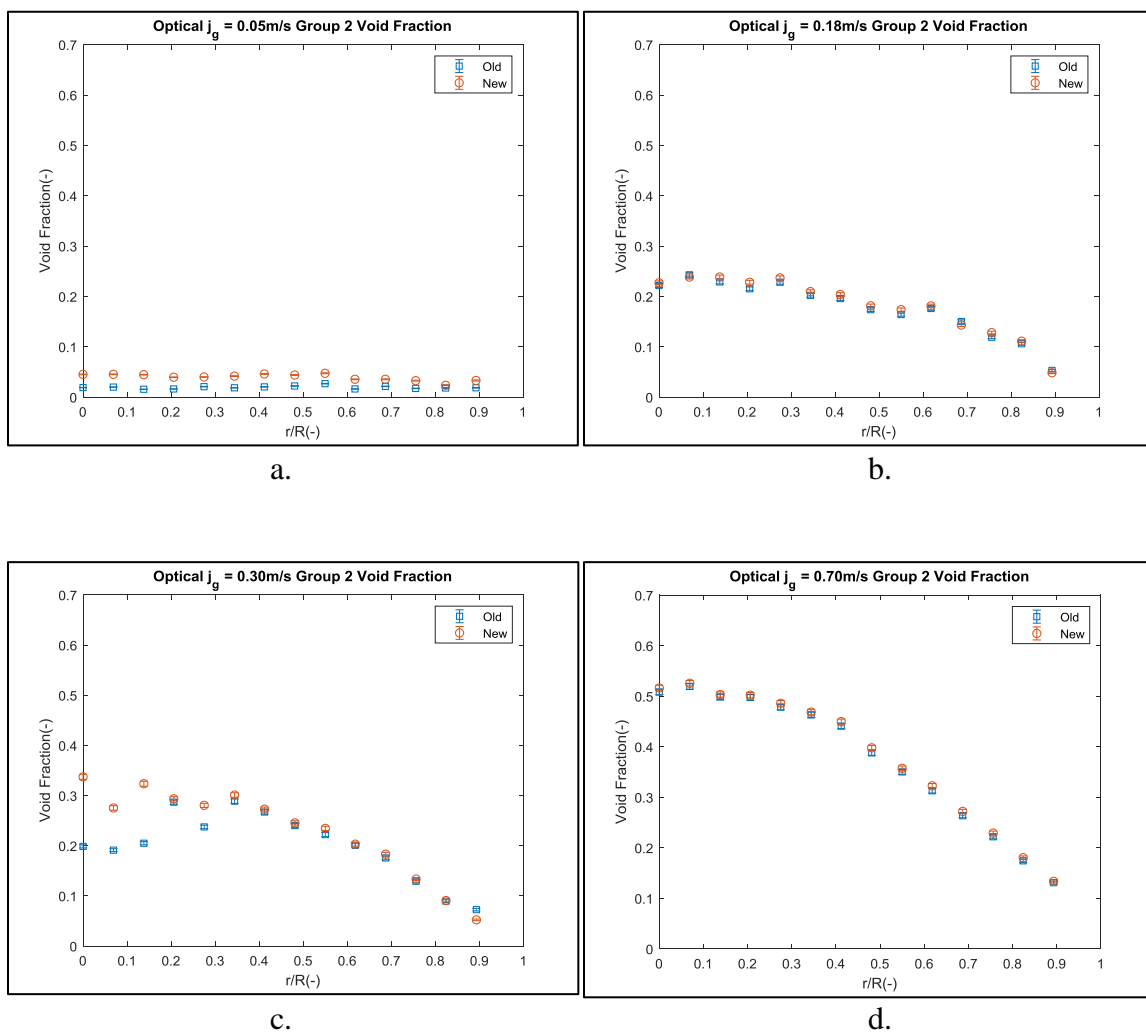
Figure 5.33. New and Old Optical Group 2 VF for jg of 0.05 (a), 0.18 (b), 0.30 (c), and 0.7 (d) m/s

Table 5.22 contains the percent error for group 2 VF. There is a difference in group 2 VF for the 0.05 m/s gas velocity due to the transfer of bubbles. For the 0.18, 0.30, and

0.70 m/s gas velocity there is a much smaller difference due to less bubbles transferred from group 1 to group 2.

Table 5.22. Optical Probe Group 2 VF for jg of 0.05 (V1), 0.18 (V2), 0.30 (V3), and 0.70 (V4) m/s Percent Error

r/R	V1	V2	V3	V4
(-)	(%)	(%)	(%)	(%)
0	137.89	2.48	69.84	1.57
0.069	127.00	1.81	43.99	1.21
0.138	184.08	4.24	57.85	0.94
0.206	142.94	6.04	2.34	0.84
0.275	92.31	3.81	18.11	1.57
0.344	124.73	3.66	4.26	1.19
0.412	125.98	4.14	2.13	2.02
0.481	98.20	4.32	2.21	2.55
0.55	76.87	5.91	5.63	2.03
0.618	117.79	2.90	1.14	3.13
0.687	65.89	4.60	4.27	3.19
0.756	88.51	7.65	3.41	3.24
0.824	29.67	4.81	1.34	3.56
0.893	77.96	8.85	27.96	1.98

Figure 5.34 contains the total VF for the optical probe comparison. For each case the total VF is similar to one another. The major difference between the two method deals

with the way in which the bubbles were categorized. The categorization method will not change the total VF but will change the group VF.
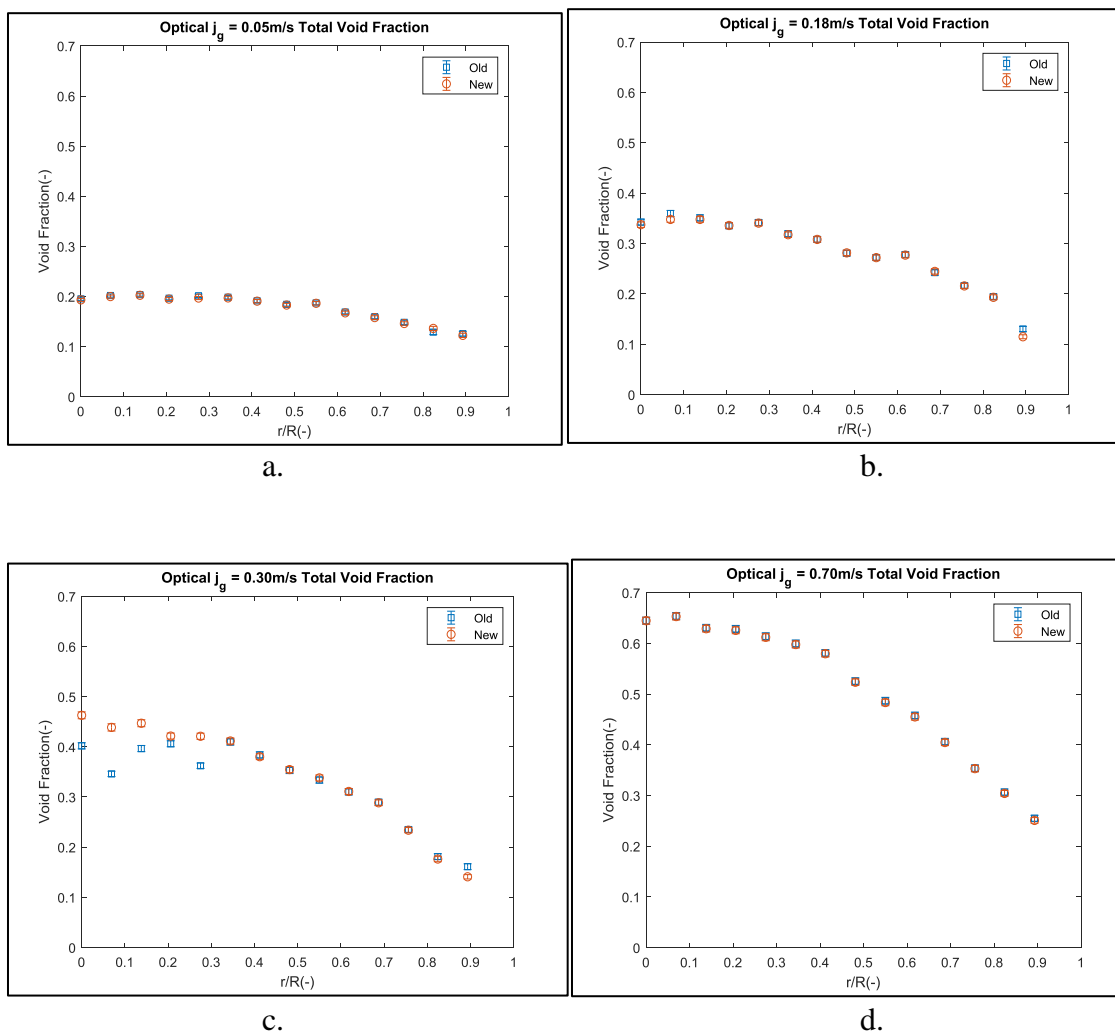
Figure 5.34. New and Old Optical Total VF for jg of 0.05 (a), 0.18 (b), 0.30 (c), and 0.7 (d) m/s

Table 5.23 contains the percent error for total VF. The majority of values are within 1% of each other. This will allow for a demonstration on how bubble grouping effects the IAC in the signal processing algorithm.

Table 5.23. Optical Probe Total VF for jg of 0.05 (V1), 0.18 (V2), 0.30 (V3), and 0.7 (V4) m/s Percent Error

r/R	V1	V2	V3	V4
(-)	(%)	(%)	(%)	(%)
0	1.08	1.49	15.12	0.02
0.069	1.04	3.25	26.79	0.14
0.138	0.69	0.88	12.74	0.27
0.206	0.87	0.15	3.77	0.43
0.275	2.23	0.35	16.23	0.29
0.344	0.71	0.59	0.44	0.30
0.412	0.37	0.03	0.91	0.24
0.481	0.76	0.25	0.45	0.38
0.55	0.37	0.04	1.26	0.70
0.618	1.01	0.40	0.26	0.59
0.687	1.13	0.95	0.38	0.42
0.756	1.55	0.32	0.55	0.20
0.824	5.74	0.67	2.70	0.82
0.893	2.70	11.82	12.54	1.61

Figure 5.35 contains the group 1 IAC in the system. Since additional bubbles are collected at many locations, the lost IAC from the grouping of bubbles is not as obvious in group 1 bubble.
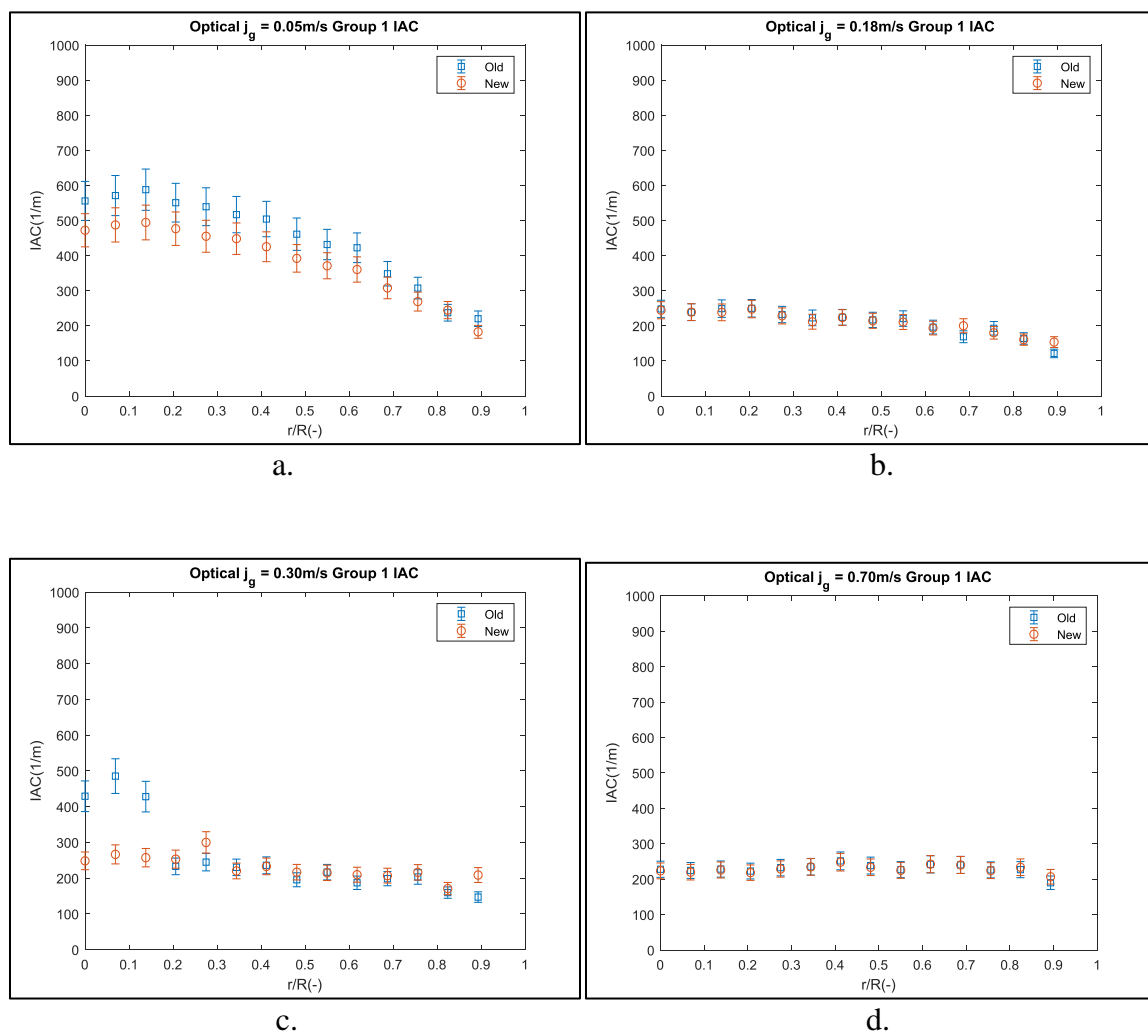
Figure 5.35. New and Old Optical Group 1 IAC for jg of 0.05 (a), 0.18 (b), 0.30 (c), and 0.7 (d) m/s

Table 5.24 contains the percent error for group 1 bubbles. The majority of the values are similar to one another. The optical probe is very close to one another however, some of the group 1 bubbles that are present in the old algorithm are shifter over into group 2 and some smaller bubbles replace the bubbles that are now in group 2.

Table 5.24. Optical Probe Group 1 IAC for jg of 0.05 (V1), 0.18 (V2), 0.30 (V3), and 0.70 (V4) m/s Percent Error

r/R	V1	V2	V3	V4
(-)	(%)	(%)	(%)	(%)
0	15.03	1.50	42.12	1.99
0.069	14.64	0.12	45.12	2.14
0.138	15.90	4.27	39.91	1.07
0.206	13.44	0.87	8.66	2.02
0.275	15.60	1.70	22.53	1.62
0.344	13.27	4.94	4.40	0.16
0.412	15.65	0.27	1.28	1.47
0.481	14.92	1.19	10.88	1.99
0.55	14.01	4.49	0.85	0.91
0.618	14.66	1.45	12.08	0.24
0.687	11.61	18.52	4.24	0.10
0.756	12.51	6.57	6.41	0.92
0.824	3.14	1.99	7.02	2.99
0.893	16.93	26.55	41.95	8.89

Figure 5.36 contains the group 2 IAC for the optical probes. There is a visible increase in the group 2 IAC. The increase is from the shift of group 1 bubbles. This is best displayed by the gas velocity of 0.05 m/s where the increase in IAC is most relevant.
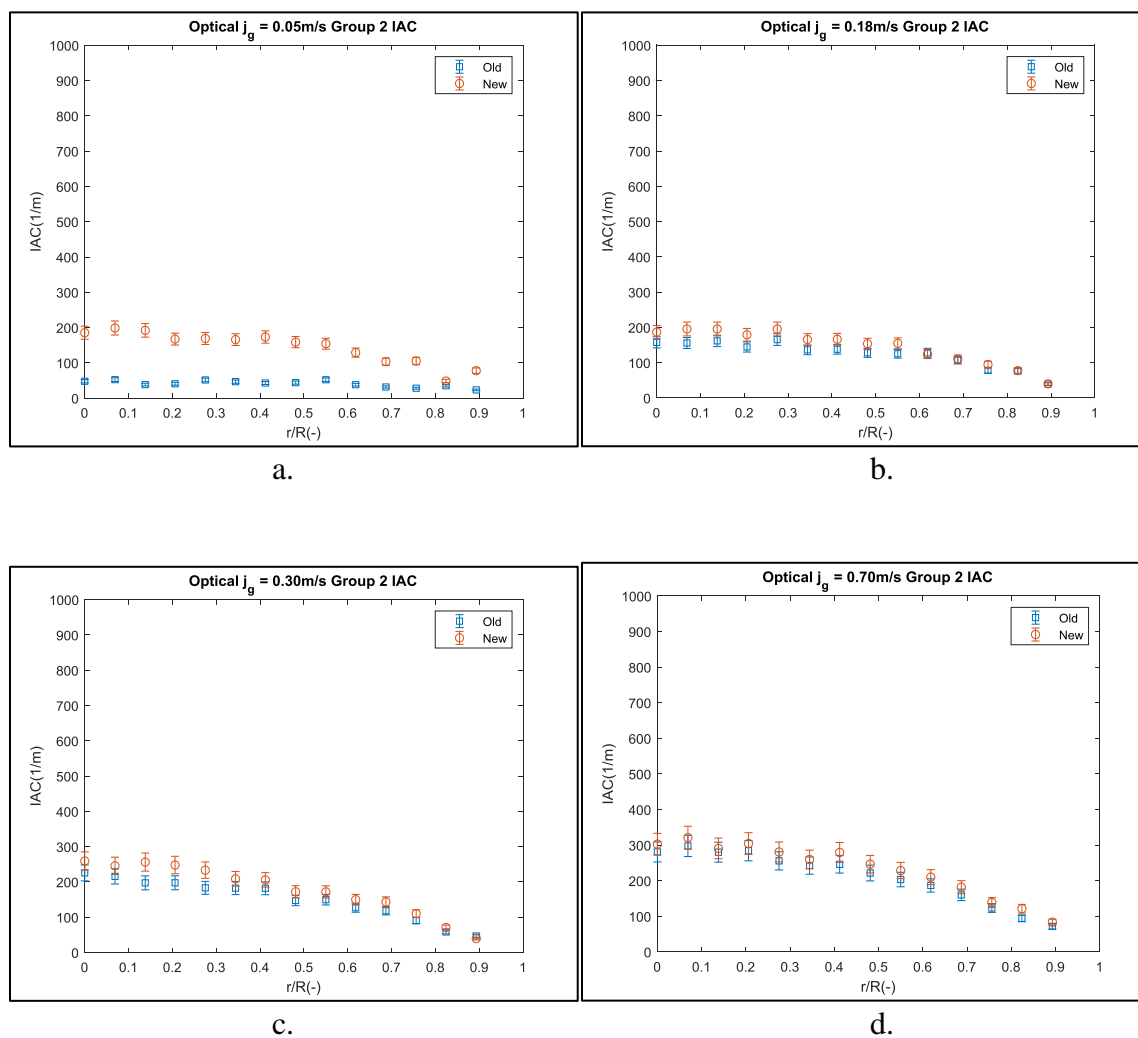
Figure 5.36. New and Old Optical Group 2 IAC for jg of 0.05 (a), 0.18 (b), 0.30 (c), and 0.7 (d) m/s

The percent error for group 2 IAC for the optical probe comparison is shown in Table 5.25. The change of bubbles into different groups will affect the IAC in the system. The largest change is in the first velocity and the other three gas velocities have less of an increase in the interfacial area concentration. The largest difference in the IAC is near the center of the bubble column where the largest amount of bubbles is present.

Table 5.25. Optical Probe Group 2 IAC for jg of 0.05 (V1), 0.18 (V2), 0.30 (V3), and 0.7 (V4) m/s Percent Error

r/R	V1	V2	V3	V4
(-)	(%)	(%)	(%)	(%)
0	287.95	18.42	14.91	7.79
0.069	279.37	25.49	13.85	7.82
0.138	400.83	20.84	29.84	3.83
0.206	310.07	23.91	25.46	7.07
0.275	227.86	18.12	27.32	9.72
0.344	254.83	21.56	14.47	7.13
0.412	303.94	20.53	13.09	13.53
0.481	260.69	20.31	16.90	11.23
0.55	195.82	23.59	14.87	12.40
0.618	238.99	2.99	18.05	12.49
0.687	226.85	3.23	21.13	13.45
0.756	275.79	21.08	21.78	12.48
0.824	38.17	1.06	21.64	28.77
0.893	233.52	2.17	15.95	16.52

Figure 5.37 contains the total IAC for the comparison between the two versions of the data processing algorithm. The collection of additional bubbles can increase to total IAC as the bubble density increases in the system. However, the IAC for larger VF where

more larger bubbles are present does not seem to increase the total IAC as much as in the lower gas velocities.
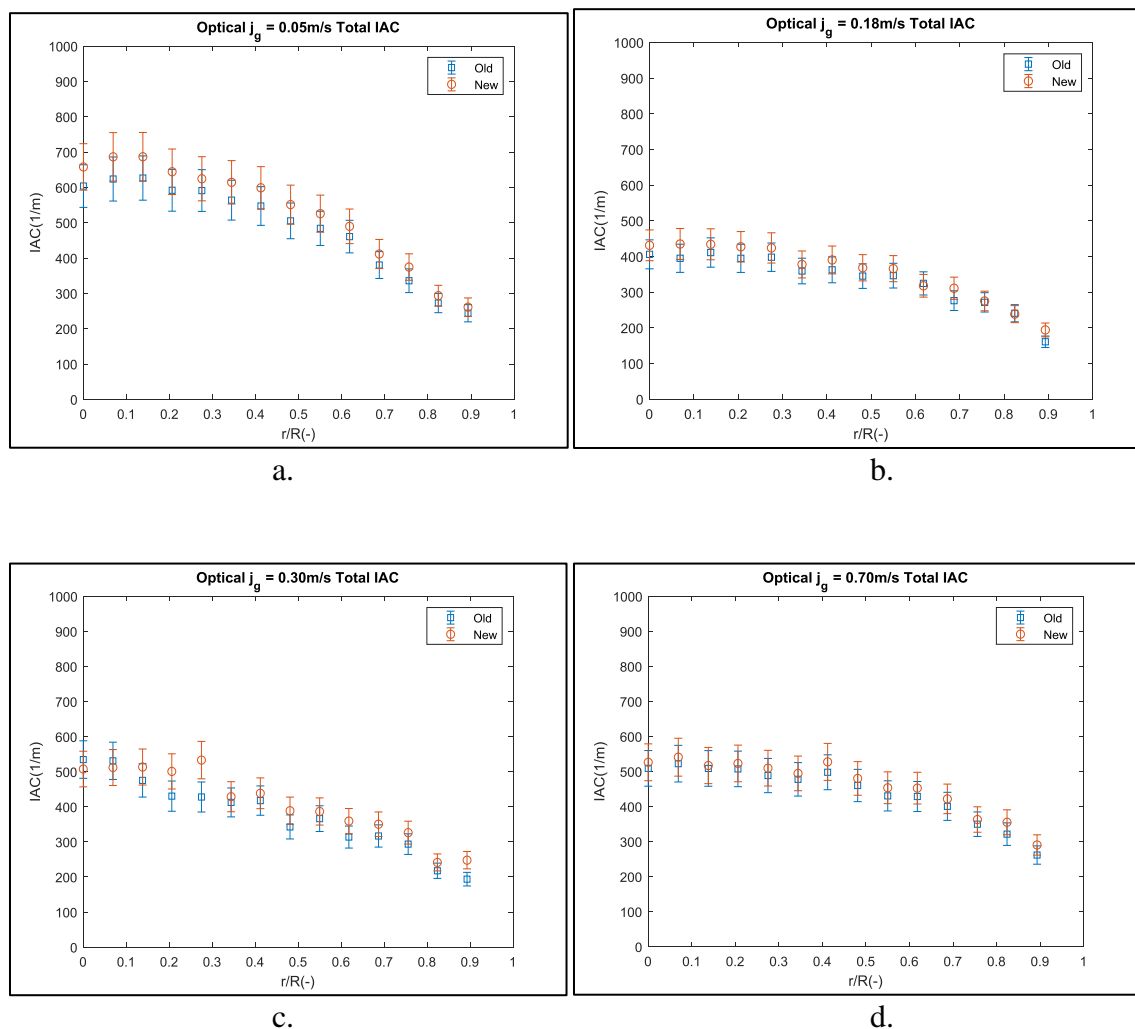

Figure 5.37. New and Old Optical Total IAC for Gas Velocities 0.05 (a), 0.18 (b), 0.30 (c), and 0.7 (d) m/s

Table 5.26 contains the percent error for the total IAC in the system. The largest deviations in the total IAC is for the lowest velocity where a large density of smaller

bubbles are present in the system. The other 3 velocities produce results that are much closer to one another and are in many cases within 10% of one another.

Table 5.26. Optical Probe Total IAC for jg of 0.05 (V1), 0.18 (V2), 0.30 (V3), and 0.7 (V4) m/s Percent Error

r/R	V1	V2	V3	V4
(-)	(%)	(%)	(%)	(%)
0	8.96	6.24	5.06	3.41
0.069	10.07	10.13	3.59	3.54
0.138	9.62	5.62	8.03	1.63
0.206	8.86	8.21	16.37	3.07
0.275	5.64	6.55	24.59	4.32
0.344	8.97	5.12	3.95	3.54
0.412	9.41	7.65	4.98	5.94
0.481	9.10	6.78	13.47	4.38
0.55	8.60	5.68	5.57	5.38
0.618	6.32	2.05	14.50	5.58
0.687	8.22	12.59	10.55	5.32
0.756	11.54	1.41	11.15	3.81
0.824	7.65	1.03	10.93	10.56
0.893	7.05	20.60	27.94	10.97

5.3.4. New Version Conductivity and Optical Bubble Comparison. Since the optical probe results are much closer to one another, the optical probe and the conductivity probe in the new algorithm should be close to one another to show the validity of the results. This portion will compare the optical and conductivity probe for the new algorithm and will show the results that were produced. Figure 5.38 displays the group 1 optical and conductivity probes for the new version of the data processing algorithm.

Figure 5.38. New Optical and Conductivity Group 1 VF for Gas Velocities 0.05 (a), 0.18 (b), 0.30 (c), and 0.7 (d) m/s

The conductivity probe for group 1 VF in the four velocities is much smaller than the optical probe for most cases. The optical and conductivity probe for the higher velocity however, is much closer to one another. Table 5.27 contains the percent error between the optical and conductivity probes for group 1 VF.

Table 5.27. New Optical and Conductivity Probe Group 1 VF for jg of 0.05 (V1), 0.18 (V2), 0.30 (V3), and 0.7 (V4) m/s Percent Error

r/R	V1	V2	V3	V4
(-)	(%)	(%)	(%)	(%)
0	22.24	60.16	7.97	3.43
0.069	26.38	49.72	20.21	18.38
0.138	25.24	32.75	6.24	0.88
0.206	25.53	35.69	3.61	12.45
0.275	28.21	32.34	0.85	8.49
0.344	32.13	47.82	23.91	4.73
0.412	23.10	39.44	9.87	5.39
0.481	18.17	44.36	11.47	6.37
0.55	21.87	38.39	6.87	27.28
0.618	16.86	39.14	5.66	15.13
0.687	19.93	53.45	16.54	10.26
0.756	18.80	53.42	8.88	4.36
0.824	25.00	55.12	14.85	3.56
0.893	15.90	37.20	30.96	20.41

The largest error is in the second velocity where the bubble density is the smallest. The second largest deviation is in the first velocity where the largest amount of group 1 bubbles are present. These two velocities are around the transition point between bubbly and churn turbulent flows. Figure 5.39 contains the group 2 VF for the comparison for the optical and conductivity probes.
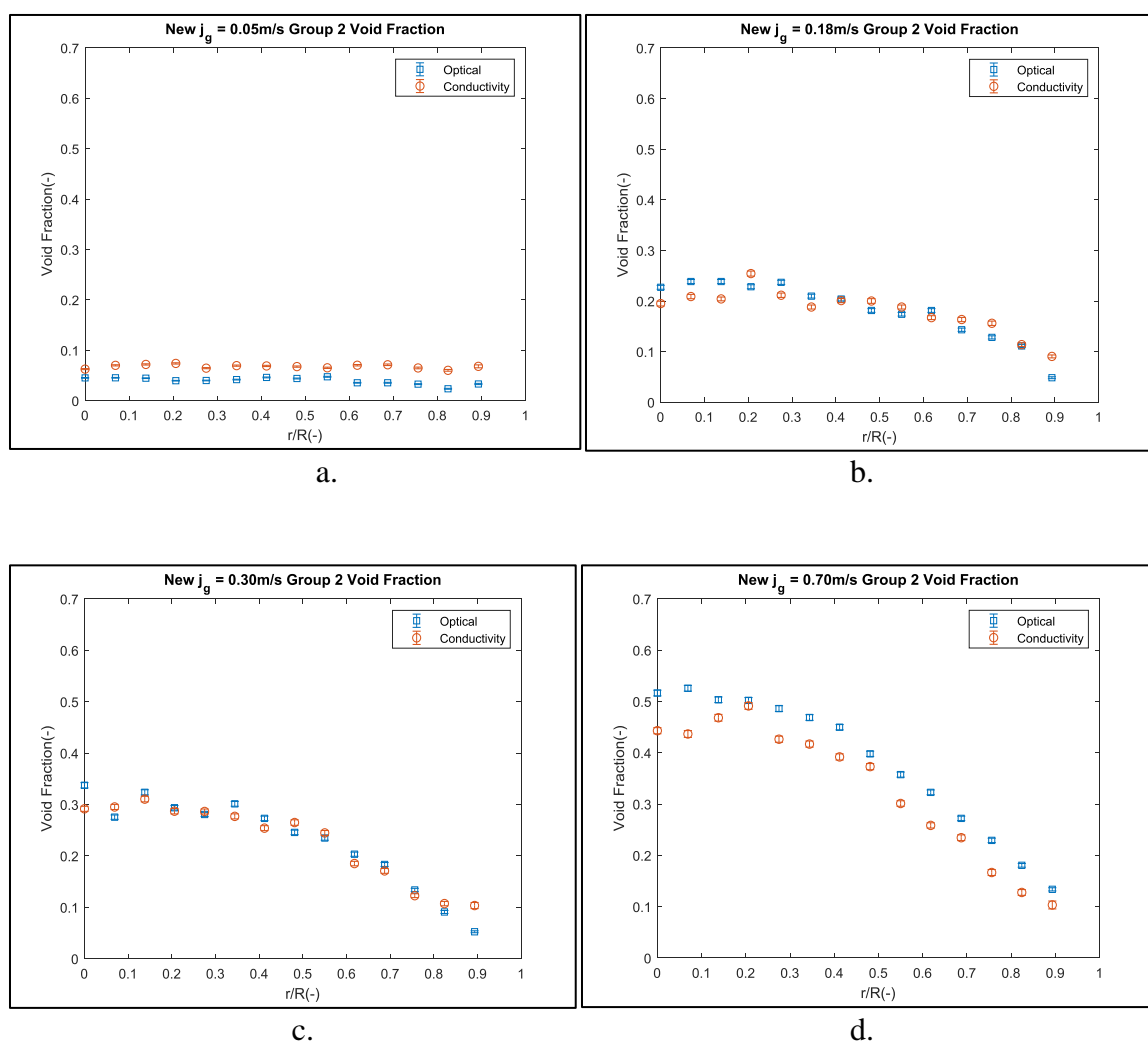
Figure 5.39. New Optical and Conductivity Group 2 VF for jg of 0.05 (a), 0.18 (b), 0.30 (c), and 0.7 (d) m/s

The conductivity probe has a larger shift in the first velocity and the therefore more group 2 bubbles. The optical probe and conductivity probe group 2 VF for the 2nd and 3rd velocities are much closer to one another. The final velocity has more group 2 bubbles in the system compared to the conductivity probe.

Table 5.28. New Optical and Conductivity Probe Group 2 VF for jg of 0.05 (V1), 0.18 (V2), 0.30 (V3), and 0.7 (V4) m/s Percent Error

r/R	V1	V2	V3	V4
(-)	(%)	(%)	(%)	(%)
0	38.50	14.18	13.58	14.22
0.069	54.41	12.45	7.19	16.95
0.138	61.21	14.42	4.08	6.98
0.206	86.62	11.39	2.28	2.15
0.275	61.25	10.76	2.07	12.28
0.344	66.27	10.26	8.10	11.05
0.412	49.46	1.52	6.96	12.88
0.481	53.64	10.31	7.82	6.26
0.55	37.55	8.23	4.22	15.76
0.618	98.03	7.78	8.96	19.96
0.687	100.56	14.11	6.82	13.86
0.756	97.87	21.78	8.31	27.32
0.824	155.08	2.34	17.95	29.31
0.893	105.74	86.98	97.51	22.81

Table 5.28 contains the VF for all group 2 bubbles for comparing the optical and conductivity probes with one another. Figure 5.40 contains the total VF for the comparison of the optical and conductivity probes. The total VF for the optical and conductivity probes are close to one another for the first three velocities. In the fourth velocity, the optical probe is picking up a slightly larger amount of VF for the system.
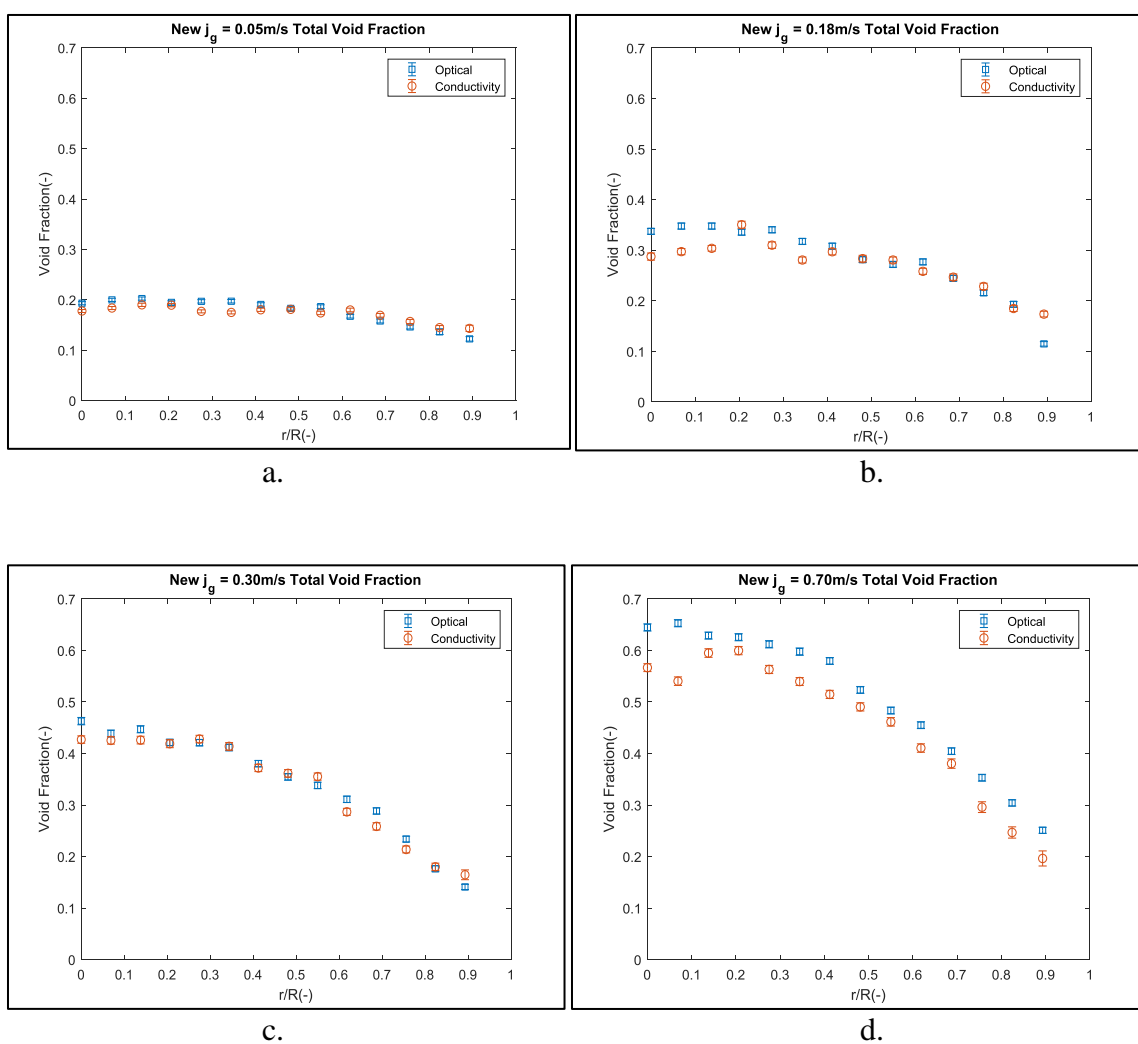
Figure 5.40. New Optical and Conductivity Total VF for Gas Velocities 0.05 (a), 0.18 (b), 0.30 (c), and 0.7 (d) m/s

Table 5.29 contains the percent error for the total VF for the new algorithm for the optical and conductivity probes. Most values for all four velocities are within 10% of one another with the largest deviations near the center of the bubble column and the smallest deviations in the second velocity with the smallest amount of bubbles.

Table 5.29. New Optical and Conductivity Probe Total VF for jg of 0.05 (V1), 0.18 (V2), 0.30 (V3), and 0.7 (V4) m/s Percent Error

r/R	V1	V2	V3	V4
(-)	(%)	(%)	(%)	(%)
0	8.02	14.79	7.74	12.10
0.069	8.11	14.52	3.03	17.23
0.138	6.18	12.65	4.70	5.39
0.206	2.82	4.38	0.57	4.16
0.275	10.11	8.93	1.66	7.99
0.344	11.26	11.59	0.53	9.70
0.412	5.56	3.60	2.21	11.20
0.481	1.04	0.71	1.92	6.29
0.55	6.71	3.20	5.06	4.53
0.618	7.47	6.75	7.81	9.76
0.687	7.16	0.90	10.37	5.96
0.756	7.39	5.89	8.60	16.18
0.824	6.16	4.35	2.04	18.88
0.893	16.99	51.17	16.75	21.76

Figure 5.41 contains the group 1 IAC for the new algorithm for both the conductivity and optical probe for the four gas velocities. The group 1 IAC for all four gas velocities are similar to one another in shape. The largest variation between the two is the fourth velocity.
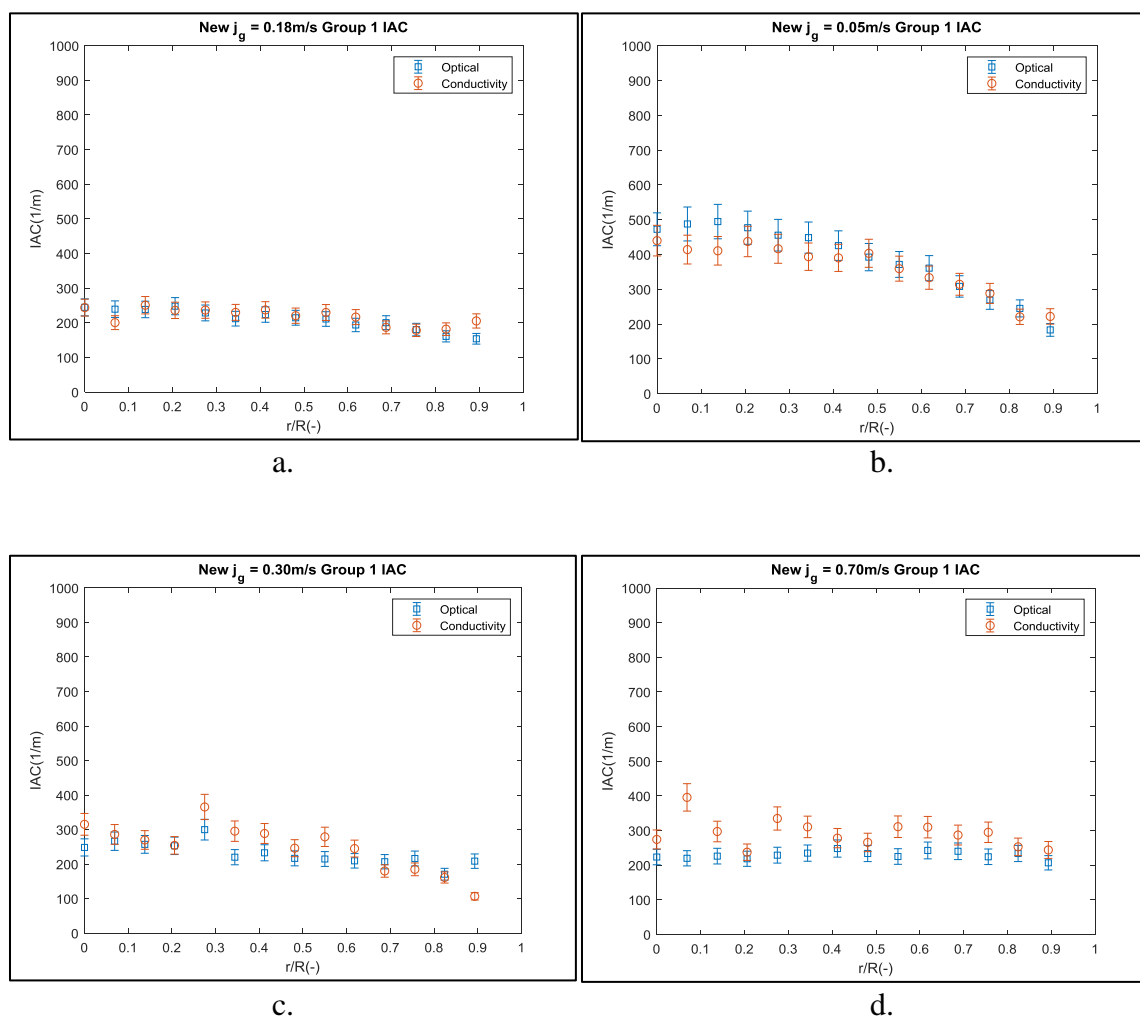
Figure 5.41. New Optical and Conductivity Group 1 IAC for jg of 0.05 (a), 0.18 (b), 0.30 (c), and 0.7 (d) m/s

Table 5.30 contains the percent error for the group 1 IAC for the new algorithm comparison for optical and conductivity probes. For the group 1 IAC most values for the first 2 velocities are within 15% of one another. The deviation between the IAC for group 1 in the last two velocities are further apart from one another than the first two velocities.

Table 5.30. New Optical and Conductivity Probe Group 1 IAC for jg of 0.05 (V1), 0.18 (V2), 0.30 (V3), and 0.7 (V4) m/s Percent Error

r/R	V1	V2	V3	V4
(-)	(%)	(%)	(%)	(%)
0	6.91	0.31	26.95	22.72
0.069	15.10	16.24	7.36	80.03
0.138	16.99	5.11	4.98	31.47
0.206	8.30	4.84	0.51	8.67
0.275	8.57	3.59	21.92	46.29
0.344	12.23	8.59	34.29	32.24
0.412	8.27	5.98	24.02	12.09
0.481	2.80	2.79	13.63	13.69
0.55	3.26	8.91	29.90	38.24
0.618	7.59	11.75	16.93	27.74
0.687	1.98	6.79	13.01	19.50
0.756	6.99	1.25	14.52	31.53
0.824	9.84	12.92	5.55	8.19
0.893	21.16	33.46	48.83	17.90

Figure 5.42 contains the group 2 IAC for the new algorithm comparison of the optical and conductivity probes. The conductivity probe has the largest values. This is from a combination of the shifted bubbles from the conductivity probe and some misaligned interfaces due to the low sample rate in the system. Some of the misalign bubbles cause the size of the bubbles to read as larger or smaller than the actual size. The interface location can cause large deviations in the IAC.
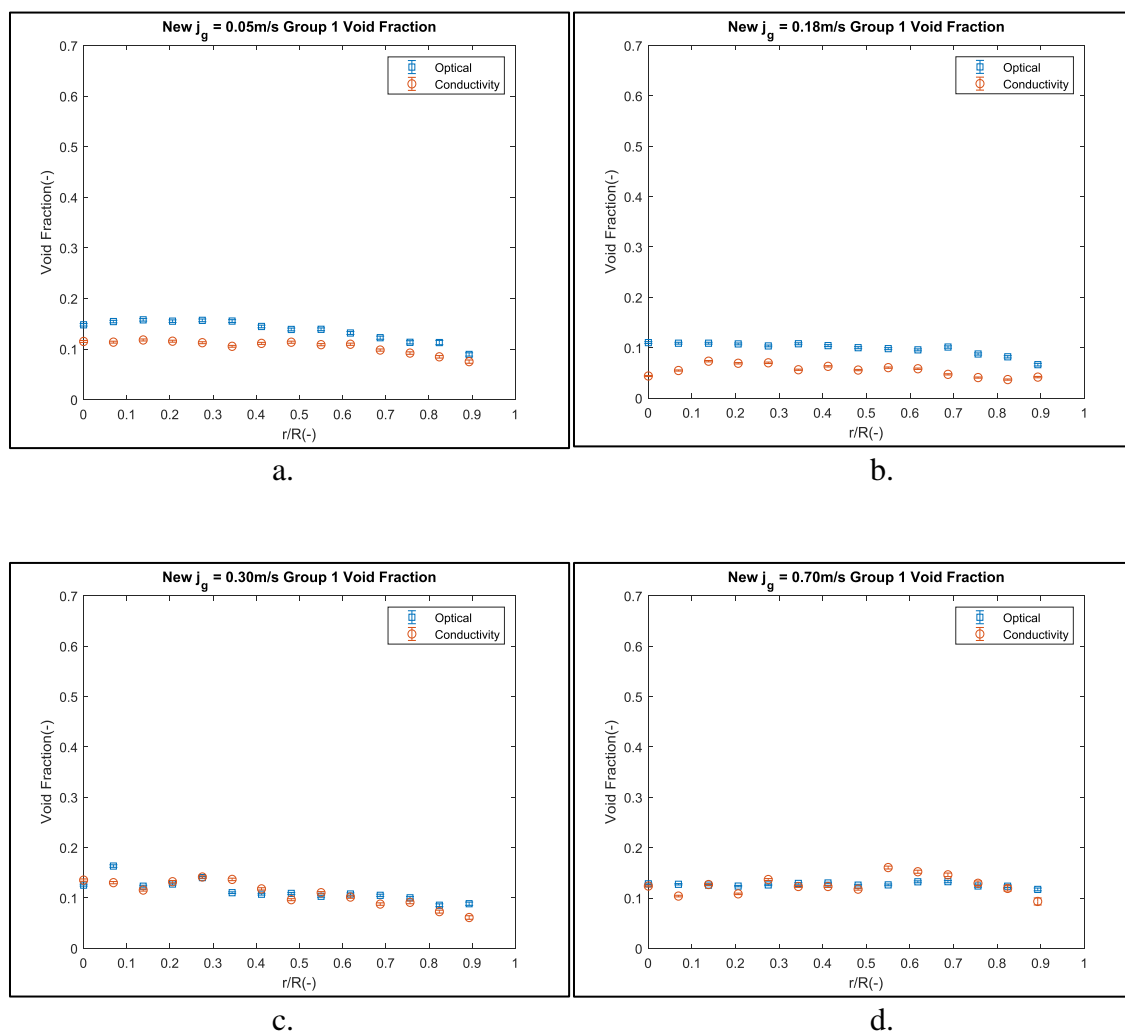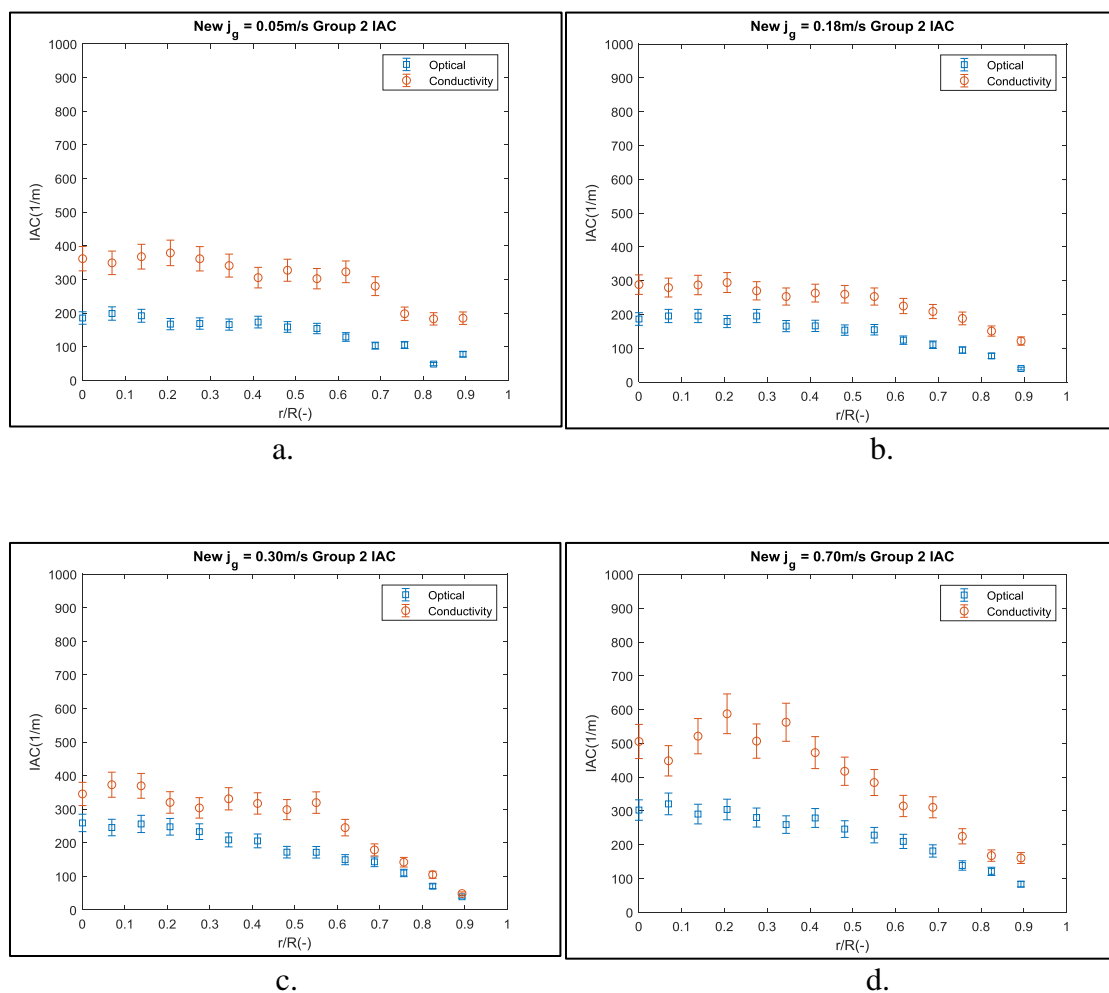

Figure 5.42. New Optical and Conductivity Group 2 IAC for Gas Velocities 0.05 (a), 0.18 (b), 0.30 (c), and 0.7 (d) m/s

Table 5.31 contains the percent error for the group 1 IAC for the new algorithm comparison for optical and conductivity probes. All places in the group 2 IAC are consistently off by 50% from one another. The large deviation on the results is due to the smaller bubbles in the system.

Table 5.31. New Optical and Conductivity Probe Group 2 IAC for jg of 0.05 (V1), 0.18 (V2), 0.30 (V3), and 0.7 (V4) m/s Percent Error

r/R	V1	V2	V3	V4
(-)	(%)	(%)	(%)	(%)
0	95.09	54.49	33.30	67.04
0.069	75.77	43.01	51.91	39.72
0.138	91.44	46.89	44.30	79.24
0.206	126.53	64.34	29.20	92.99
0.275	113.91	38.16	30.32	80.60
0.344	105.67	52.79	58.56	116.59
0.412	76.20	58.27	54.20	69.25
0.481	106.13	69.01	73.60	69.44
0.55	95.99	63.43	86.04	68.10
0.618	149.96	81.41	63.71	49.87
0.687	171.07	88.91	24.81	71.08
0.756	88.31	98.84	29.18	62.26
0.824	277.14	94.85	48.26	38.41
0.893	137.66	202.89	24.21	92.70

Figure 5.43 contains the total IAC for the new algorithm comparison for optical and conductivity probes. The conductivity probe consistently gives a larger IAC for the for the system. The total IAC is larger due to the large deviation of group 2 bubbles. This increase is due to the large variation from the bubbles that were shifted into group 2 from group 1 and these bubbles cause differing results.
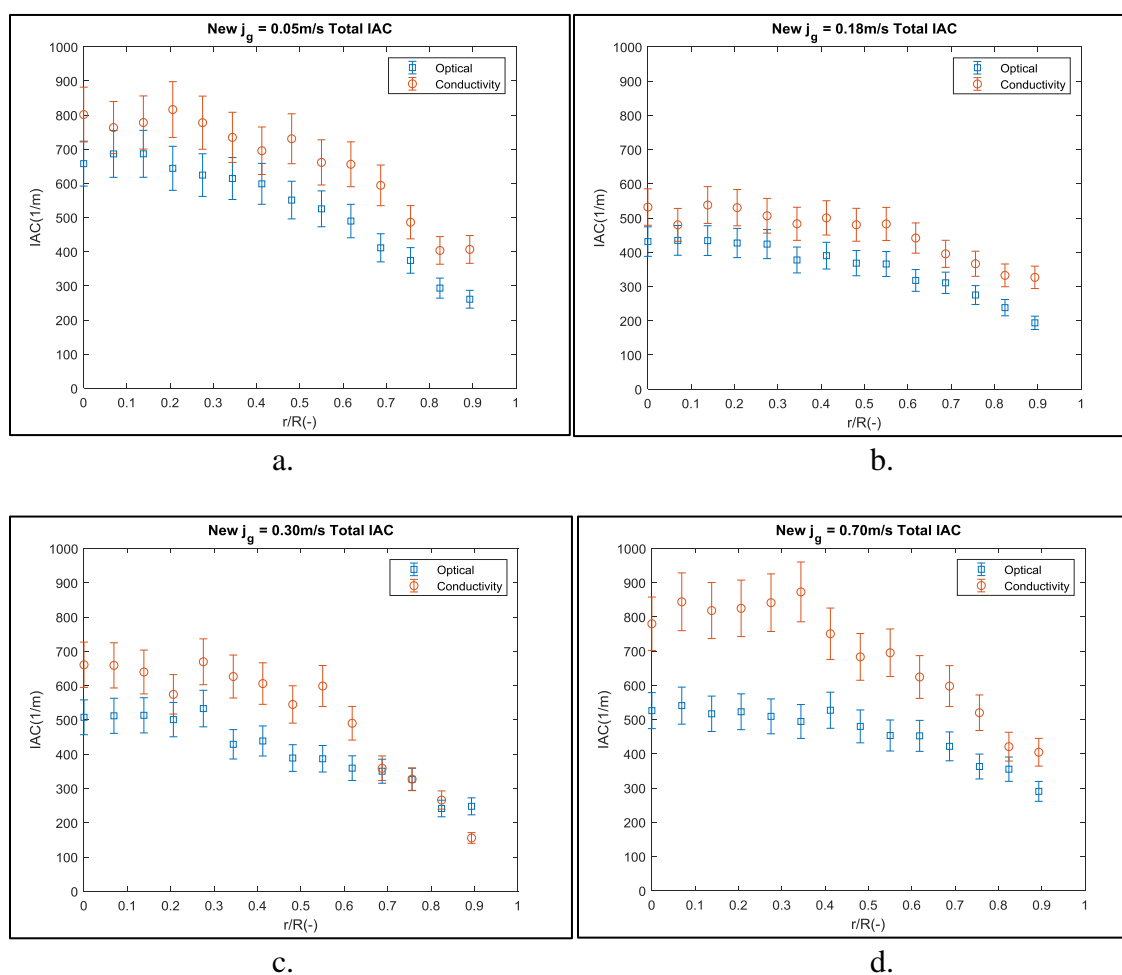
Figure 5.43. New Optical and Conductivity Total IAC for Gas Velocities 0.05 (a), 0.18 (b), 0.30 (c), and 0.7 (d) m/s

Table 5.32 contains the percent error between the conductivity and optical probes for the new algorithm. Most values are around 35% from each other with the biggest deviation in the fourth velocity where there is a large amount bubbles in the bubble column.

Table 5.32. New Optical and Conductivity Probe Total IAC for jg of 0.05 (V1), 0.18 (V2), 0.30 (V3), and 0.7 (V4) m/s Percent Error

r/R	V1	V2	V3	V4
(-)	(%)	(%)	(%)	(%)
0	21.84	23.41	30.19	48.22
0.069	11.22	10.41	28.73	56.10
0.138	13.34	23.93	24.61	58.35
0.206	26.72	24.18	14.71	57.77
0.275	24.58	19.53	25.60	65.19
0.344	19.61	27.99	46.11	76.55
0.412	16.18	28.27	38.18	42.37
0.481	32.58	30.44	40.20	42.31
0.55	25.87	32.00	54.87	53.29
0.618	33.95	38.95	36.44	38.01
0.687	44.45	27.23	2.48	41.73
0.756	29.85	33.21	0.24	43.28
0.824	37.60	39.56	10.24	18.52
0.893	55.91	68.48	37.23	39.40

A few items to take note of in the comparison of the two results is the VF at 22kHz is around 10% of each other for the new algorithm, while the IAC for the conductivity probe is much larger. This means that the bubbles are being picked up by the new algorithm but the interface location at 22 kHz causes deviation in the IAC.

5.4. CONCLUSIONS

This study explores the importance of grouping bubbles and the changes to the IAC and VF when trailing bubble are missed. To determine the differences in the two methods, a new algorithm to collect trailing bubbles and to categorize bubbles based on chord length was developed. The new algorithm was benchmarked with the current method to determine the IAC and VF in the system. There are three main areas of study in the measurement of IAC and VF. These areas were in signal conditioning, the pairing process, and the grouping of bubbles. Signal conditioning at 22kHz produces a large number of missed bubbles due to the short response time of the conductivity probe.

The missed bubbles are due to the threshold values used to remove the noise in the system. The previous code misses small trailing bubbles that are extremely close to a large bubble. To collect the trailing bubbles and bubbles with a short response time, a moving comparison algorithm was implemented into the code. The moving comparison results in four different velocities, showing an increase in the amount of bubbles collected by the algorithm when the conductivity probe is used. After the bubbles are collected, an increase in the total number of bubbles are discovered in the data processing algorithm.

However, to ensure that the new bubbles picked up are not noise, the effective bubble are counted. The difference in the amount of bubbles in the new algorithm for both

the optical and conductivity probes are similar. The optical probe will pick up more of the

smaller bubbles due to the fast response time. The optical probe is therefore more accurate

at the lower sampling rates. The optical probe will still miss some trailing bubbles. The

trailing bubbles are very small compared to the first bubble and will not strongly affect the

VF in the system. However, the trailing bubbles will affect the IAC in the system. When

comparing the bubble diameter with the chord length calculated, the bubble diameter is

found to be larger. There are a few bubbles that will fall below the chord length, these

bubbles are normally due to the distortions within the bubbles or the computational error

when using the TRM. At 22kHz, the old version of the conductivity probe code will pick

up fewer bubbles than the optical probe code. The conductivity probe in the new algorithm

will pick up more bubbles than the previous version. Additionally, the optical probe for

both algorithms will produce similar results. To determine the validity of the two

algorithms, the optical probe was used as a benchmark to check the differences between

the two algorithms. The VF was the same in both algorithms, but the IAC increased in the

new algorithm for all four velocities with up to a 24% increase in the total IAC. When

comparing the new algorithm for the optical and conductivity probes, the new algorithm

produced similar result in the total VF except for a few outliers, most results were within

10% of one another. The optical probe demonstrated a large variation in IAC depending of

the number of bubbles transferred between groups.

As the bubbles change groups the IAC in the system increased in all cases. When

comparing the optical and conductivity probe for group 1, group 2, and total IAC for the

new algorithm; the conductivity probe has a larger IAC for each case. This can be due to

the slow response time of the conductivity probe creating paired bubbles with interfaces

slightly skewed from one another. However, for both the conductivity and optical probes the IAC is larger than the results from the previous version of the code. A few Recommendations for this work include testing the new algorithm at higher sample rates, a longer duration to remove the outliers, and to test the new algorithm at different gas velocities. This will ensure the interfaces for the conductivity probe are in the correct location for more accurate results.

This study establishes that the IAC is directly related to the categorization of bubbles. As bubbles change group the IAC in the system will change as well. The new algorithm changes the conventional method for categorizing bubbles by using the diameter for all group 1 bubbles. The new algorithm also shows an increase in the number of bubbles and these bubbles are mainly trailing bubbles that will not strongly affect the VF.

APPENDIX

SUPPLEMETAL RESULTS TABLES

Table A1. Conductivity Probe Lead Sensor All Bubbles for jg of 0.05 (V1), 0.18 (V2), 0.30 (V3), and 0.7 (V4) m/s per 300s

r/R	V1 Old	V1 New	V2 Old	V2 New	V3 Old	V3 New	V4 Old	V4 New
(-)	(#)	(#)	(#)	(#)	(#)	(#)	(#)	(#)
0	5430	9930	5280	14670	9810	22200	19290	33420
0.069	5640	10230	5580	14640	9480	21870	17460	32490
0.138	5340	9840	6420	16170	8910	17580	18750	31770
0.206	5520	9810	6570	15360	9240	21240	17940	28860
0.275	5460	9990	6120	15270	10140	30150	17460	32880
0.344	4890	9540	6000	13980	8730	22260	16770	30660
0.412	4890	9300	5550	14880	7470	18720	13890	29700
0.481	5070	8970	4770	12480	7020	17460	14280	27840
0.55	4350	8640	5100	13980	6810	17190	12840	25980
0.618	4200	8430	4590	12690	5310	14820	10890	23580
0.687	3720	7590	4020	10590	4110	11280	8580	21030
0.756	2760	6600	3450	9540	3420	11100	5880	16320
0.824	2520	6240	2940	9180	2250	8940	4590	13980
0.893	1650	4110	2430	8340	1110	6270	2430	10830

Table A2. Optical Probe Lead Sensor All Bubbles for jg of 0.05 (V1), 0.18 (V2), 0.30 (V3), and 0.7 (V4) m/s per 300s

r/R	V1	V1	V2	V2	V3	V3	V4	V4
	Old	New	Old	New	Old	New	Old	New
(-)	(#)	(#)	(#)	(#)	(#)	(#)	(#)	(#)
0	9630	9960	14070	14820	20190	24390	28290	29430
0.069	10140	10500	13950	14070	26400	28170	28500	29280
0.138	10350	10650	13560	14070	22170	19980	27600	28530
0.206	9900	10230	13590	14190	17640	20880	27300	28290
0.275	9540	10950	13290	13830	17730	21780	26820	27690
0.344	9120	9450	13170	13770	17160	17700	26310	27330
0.412	8670	9030	12480	13200	16710	17550	26760	27690
0.481	7740	8130	11520	12300	15000	17250	24090	25260
0.55	7830	8220	11010	11640	14670	15810	22980	24150
0.618	6990	7290	11340	12690	13470	15810	22020	23280
0.687	6090	6570	11250	10740	13050	14580	19980	21240
0.756	5400	5940	9390	10380	11550	12990	17520	18990
0.824	4830	7440	8100	9270	9390	10560	16260	17640
0.893	4530	6480	6300	8940	8640	14400	14220	15540

Table A3. Optical Probe (OP) and Conductivity Probe (CP) New Lead Sensor All Bubbles for jg of 0.05 (V1), 0.18 (V2), 0.30 (V3), and 0.7 (V4) for 300s

r/R	V1	V1	V2	V2	V3	V3	V4	V4
	OP	CP	OP	CP	OP	CP	OP	CP
(-)	(#)	(#)	(#)	(#)	(#)	(#)	(#)	(#)
0	9630	9960	14070	14820	20190	24390	28290	29430
0.069	10140	10500	13950	14070	26400	28170	28500	29280
0.138	10350	10650	13560	14070	22170	19980	27600	28530
0.206	9900	10230	13590	14190	17640	20880	27300	28290
0.275	9540	10950	13290	13830	17730	21780	26820	27690
0.344	9120	9450	13170	13770	17160	17700	26310	27330
0.412	8670	9030	12480	13200	16710	17550	26760	27690
0.481	7740	8130	11520	12300	15000	17250	24090	25260
0.55	7830	8220	11010	11640	14670	15810	22980	24150
0.618	6990	7290	11340	12690	13470	15810	22020	23280
0.687	6090	6570	11250	10740	13050	14580	19980	21240
0.756	5400	5940	9390	10380	11550	12990	17520	18990
0.824	4830	7440	8100	9270	9390	10560	16260	17640
0.893	4530	6480	6300	8940	8640	14400	14220	15540

Table A4. Conductivity Probe 4-Sensor Effective Bubbles for jg of 0.05 (V1), 0.18 (V2), 0.30 (V3), and 0.7 (V4) for 300s

r/R	V1	V1	V2	V2	V3	V3	V4	V4
	Old	New	Old	New	Old	New	Old	New
(-)	(#)	(#)	(#)	(#)	(#)	(#)	(#)	(#)
0	1830	3510	990	1680	2220	3510	5490	5940
0.069	2010	3660	1050	2340	2160	3480	4260	5190
0.138	1920	3540	1470	2910	2460	3300	5100	5850
0.206	1950	3540	1260	2580	2280	2940	5610	5940
0.275	1890	3450	1290	2370	2040	3480	5130	5820
0.344	1920	3480	1350	2220	1920	3150	4890	5850
0.412	1650	3120	1260	2370	1590	2790	4230	5010
0.481	1710	3000	1050	1860	1560	2430	3810	4470
0.55	1410	2670	1170	2220	1470	2580	3150	4050
0.618	1350	2490	930	1860	990	1800	2520	3120
0.687	1110	2130	780	1530	750	1320	1740	2700
0.756	780	1470	600	1320	570	1050	810	1560
0.824	690	1200	450	990	300	630	510	1110
0.893	300	540	360	960	90	300	180	810

Table A5. Optical Probe 4-Sensor Effective Bubbles for jg of 0.05 (V1), 0.18 (V2), 0.30 (V3), and 0.7 (V4) for 300s

r/R	V1	V1	V2	V2	V3	V3	V4	V4
	Old	New	Old	New	Old	New	Old	New
(-)	(#)	(#)	(#)	(#)	(#)	(#)	(#)	(#)
0	4260	4200	3840	3780	4560	5370	9270	9540
0.069	4410	4410	3810	3840	3690	4530	9450	9720
0.138	4530	4500	3810	3840	4140	4650	9180	9480
0.206	4260	4230	3690	3690	4920	5070	8790	9090
0.275	4050	3780	3630	3690	4710	5070	8010	8340
0.344	3570	3540	3420	3390	4590	4620	7590	7800
0.412	3450	3420	3210	3210	4320	4260	7890	8310
0.481	2940	2850	2700	2700	3360	3390	6780	6840
0.55	2940	2880	2700	2670	3270	3270	5700	5790
0.618	2430	2370	2670	2550	2760	2790	5070	5220
0.687	1830	1770	2130	2070	2550	2490	4290	4350
0.756	1770	1680	1920	1800	1950	1920	3210	3150
0.824	1080	960	1530	1440	1080	1050	2730	2730
0.893	840	810	840	720	1050	840	2070	2010

Table A6. Optical Probe (OP) and Conductivity Probe (CP) 4-Sensor Effective Bubbles
for jg of 0.05 (V1), 0.18 (V2), 0.30 (V3), and 0.7 (V4) for 300s

r/R	V1	V1	V1	V1	V1	V1	V1	V1
	OP	CP	OP	CP	OP	CP	OP	CP
(-)	(#)	(#)	(#)	(#)	(#)	(#)	(#)	(#)
0	3810	3510	3450	1680	4260	3510	8670	5490
0.069	3990	3660	3480	2340	4260	3480	8850	4260
0.138	4080	3540	3480	2910	4230	3300	8610	5100
0.206	3840	3540	3330	2580	4620	2940	8280	5610
0.275	3450	3450	3360	2370	4620	3480	7590	5130
0.344	3210	3480	3090	2220	4200	3150	7080	4890
0.412	3120	3120	2910	2370	3870	2790	7530	4230
0.481	2610	3000	2430	1860	3090	2430	6210	3810
0.55	2640	2670	2430	2220	2970	2580	5280	3150
0.618	2160	2490	2400	1860	2520	1800	4770	2520
0.687	1620	2130	1980	1530	2280	1320	3960	1740
0.756	1290	1470	1650	1320	1770	1050	2880	810
0.824	690	1200	1320	990	960	630	2490	510
0.893	750	540	660	960	780	300	1830	180

Table A7. Old Version Optical Probe (OP) and Conductivity Probe (CP) Group 1 VF for jg of 0.05 (V1), 0.18 (V2), 0.30 (V3), and 0.7 (V4) Per Second

r/R	V1	V1	V2	V2	V3	V3	V4	V4
	OP	CP	OP	CP	OP	CP	OP	CP
(-)	(-)	(-)	(-)	(-)	(-)	(-)	(-)	(-)
0	0.1762	0.1243	0.1208	0.0439	0.2033	0.0892	0.1365	0.1081
0.069	0.1820	0.1276	0.1165	0.0548	0.2047	0.0845	0.1344	0.1199
0.138	0.1881	0.1218	0.1214	0.0733	0.1915	0.0778	0.1320	0.1398
0.206	0.1802	0.1282	0.1201	0.0692	0.1190	0.0829	0.1306	0.1218
0.275	0.1806	0.1199	0.1135	0.0701	0.1248	0.1022	0.1353	0.1199
0.344	0.1799	0.1137	0.1172	0.0563	0.1209	0.0775	0.1364	0.1347
0.412	0.1710	0.1137	0.1123	0.0631	0.1165	0.0772	0.1401	0.1137
0.481	0.1622	0.1278	0.1069	0.0557	0.1127	0.0725	0.1374	0.1384
0.55	0.1602	0.1098	0.1080	0.0605	0.1116	0.0769	0.1366	0.1314
0.618	0.1526	0.1090	0.1021	0.0583	0.1093	0.0621	0.1447	0.1098
0.687	0.1383	0.1024	0.0921	0.0472	0.1138	0.0407	0.1426	0.0994
0.756	0.1309	0.0726	0.0975	0.0408	0.1059	0.0415	0.1318	0.0764
0.824	0.1106	0.0745	0.0884	0.0368	0.0914	0.0261	0.1323	0.0277
0.893	0.1072	0.0426	0.0772	0.0417	0.0884	0.0112	0.1239	0.0394

Table A8. Old Version Optical Probe (OP) and Conductivity Probe (CP) Group 2 VF for jg of 0.05 (V1), 0.18 (V2), 0.30 (V3), and 0.7 (V4) Per Second

r/R	V1	V1	V2	V2	V3	V3	V4	V4
	OP	CP	OP	CP	OP	CP	OP	CP
(-)	(-)	(-)	(-)	(-)	(-)	(-)	(-)	(-)
0	0.0190	0.0255	0.2216	0.2283	0.1986	0.3433	0.5083	0.5880
0.069	0.0200	0.0226	0.2429	0.2174	0.1912	0.3386	0.5193	0.5230
0.138	0.0157	0.0224	0.2288	0.2196	0.2050	0.3382	0.4985	0.5412
0.206	0.0163	0.0229	0.2152	0.2314	0.2869	0.3277	0.4978	0.5747
0.275	0.0208	0.0230	0.2282	0.1987	0.2375	0.3533	0.4785	0.5230
0.344	0.0186	0.0241	0.2022	0.2148	0.2889	0.3103	0.4631	0.5158
0.412	0.0204	0.0241	0.1958	0.1876	0.2672	0.2503	0.4408	0.5241
0.481	0.0222	0.0177	0.1738	0.1617	0.2403	0.2481	0.3879	0.4133
0.55	0.0268	0.0182	0.1641	0.1772	0.2222	0.2181	0.3502	0.3614
0.618	0.0163	0.0224	0.1761	0.1473	0.2009	0.1740	0.3129	0.3102
0.687	0.0214	0.0179	0.1501	0.1316	0.1757	0.1455	0.2636	0.2389
0.756	0.0174	0.0212	0.1190	0.1148	0.1292	0.1022	0.2219	0.1536
0.824	0.0182	0.0244	0.1061	0.0896	0.0896	0.0649	0.1743	0.0819
0.893	0.0186	0.0380	0.0531	0.0566	0.0726	0.0283	0.1311	0.0471

Table A9. Old Version Optical Probe (OP) and Conductivity Probe (CP) Total VF for jg of 0.05 (V1), 0.18 (V2), 0.30 (V3), and 0.7 (V4) Per Second

r/R	V1 OP	V1 CP	V2 OP	V2 CP	V3 OP	V3 CP	V4 OP	V4 CP
(-)	(-)	(-)	(-)	(-)	(-)	(-)	(-)	(-)
0	0.1953	0.1499	0.3425	0.2722	0.4020	0.4327	0.6448	0.6960
0.069	0.2019	0.1502	0.3595	0.2722	0.3959	0.4231	0.6538	0.6430
0.138	0.2038	0.1442	0.3509	0.2929	0.3965	0.4160	0.6306	0.6810
0.206	0.1965	0.1510	0.3353	0.3006	0.4059	0.4107	0.6284	0.6965
0.275	0.2014	0.1430	0.3417	0.2688	0.3622	0.4555	0.6138	0.6430
0.344	0.1985	0.1378	0.3194	0.2711	0.4098	0.3880	0.5995	0.6505
0.412	0.1914	0.1378	0.3082	0.2507	0.3837	0.3275	0.5810	0.6378
0.481	0.1843	0.1456	0.2807	0.2174	0.3530	0.3207	0.5254	0.5518
0.55	0.1871	0.1280	0.2721	0.2377	0.3338	0.2951	0.4868	0.4927
0.618	0.1690	0.1314	0.2781	0.2058	0.3102	0.2361	0.4577	0.4199
0.687	0.1597	0.1204	0.2423	0.1788	0.2895	0.1862	0.4062	0.3383
0.756	0.1484	0.0938	0.2165	0.1557	0.2351	0.1437	0.3537	0.2299
0.824	0.1289	0.0991	0.1945	0.1264	0.1811	0.0911	0.3066	0.1099
0.893	0.1258	0.0807	0.1303	0.0983	0.1610	0.0395	0.2550	0.0865

Table A10. Old Version Optical Probe (OP) and Conductivity Probe (CP) Group 1 IAC for jg of 0.05 (V1), 0.18 (V2), 0.30 (V3), and 0.7 (V4) Per Second

r/R	V1 OP	V1 CP	V2 OP	V2 CP	V3 OP	V3 CP	V4 OP	V4 CP
(-)	(1/m)	(1/m)	(1/m)	(1/m)	(1/m)	(1/m)	(1/m)	(1/m)
0	556.00	305.83	248.28	54.99	308.98	92.01	228.01	68.98
0.069	571.31	279.68	238.99	56.67	315.28	76.53	224.60	92.09
0.138	588.08	313.12	249.16	108.66	277.87	86.13	228.51	108.07
0.206	550.99	357.25	250.10	31.75	232.80	81.02	222.97	85.23
0.275	539.52	292.09	232.38	89.05	244.65	121.86	232.59	92.09
0.344	517.03	282.33	222.86	70.08	230.08	76.77	235.11	108.70
0.412	504.37	282.33	224.44	88.02	235.75	93.09	251.70	82.33
0.481	461.22	337.63	217.06	67.90	195.33	80.55	238.41	125.95
0.55	431.83	266.43	220.82	82.42	216.59	88.69	227.02	129.03
0.618	422.60	247.61	196.54	79.02	186.88	68.67	241.86	113.07
0.687	348.60	251.11	169.04	60.81	198.49	46.93	240.33	106.12
0.756	307.75	181.53	193.09	47.91	203.13	39.41	226.27	72.89
0.824	237.47	192.82	164.10	54.16	159.49	37.13	226.96	80.67
0.893	220.39	72.19	121.57	50.46	146.91	24.26	189.97	46.04

Table A11. Old Version Optical Probe (OP) and Conductivity Probe (CP) Group 2 IAC for jg of 0.05 (V1), 0.18 (V2), 0.30 (V3), and 0.7 (V4) Per Second

r/R	V1	V1	V2	V2	V3	V3	V4	V4
	OP	CP	OP	CP	OP	CP	OP	CP
(-)	(1/m)	(1/m)	(1/m)	(1/m)	(1/m)	(1/m)	(1/m)	(1/m)
0	47.81	63.76	157.62	102.61	225.68	204.44	280.89	294.67
0.069	52.40	54.98	155.84	107.54	215.77	199.95	297.73	263.22
0.138	38.36	53.10	161.84	140.35	197.42	213.13	280.18	309.35
0.206	40.80	58.94	144.60	138.85	197.62	204.21	284.40	301.58
0.275	51.55	63.22	165.50	119.86	183.29	210.75	255.81	263.22
0.344	46.76	70.25	136.30	145.51	182.47	182.83	242.49	299.06
0.412	42.92	70.25	138.02	131.17	182.00	150.60	246.10	270.25
0.481	44.04	45.79	127.84	116.32	147.34	145.56	221.62	251.02
0.55	52.15	49.84	125.33	121.83	149.69	143.28	203.37	227.60
0.618	38.09	61.67	127.91	103.93	126.95	112.15	186.74	207.46
0.687	31.62	51.41	107.06	97.67	118.41	93.86	160.22	106.12
0.756	28.01	64.86	78.24	71.10	90.54	78.84	123.36	72.89
0.824	35.11	82.70	76.67	49.18	58.27	47.27	94.28	80.67
0.893	23.33	88.38	39.25	44.52	46.89	27.45	71.62	46.04

Table A12. Old Version Optical Probe (OP) and Conductivity Probe (CP) Total IAC for jg of 0.05 (V1), 0.18 (V2), 0.30 (V3), and 0.7 (V4) Per Second

r/R	V1	V1	V2	V2	V3	V3	V4	V4
	OP	CP	OP	CP	OP	CP	OP	CP
(-)	(1/m)	(1/m)	(1/m)	(1/m)	(1/m)	(1/m)	(1/m)	(1/m)
0	603.81	369.59	405.91	157.61	554.66	296.46	508.89	363.66
0.069	623.71	334.66	394.84	164.21	601.05	276.48	522.33	355.30
0.138	626.44	366.22	411.01	249.01	525.28	299.26	508.69	417.42
0.206	591.79	416.19	394.70	170.60	430.42	285.23	507.37	386.81
0.275	591.07	355.30	397.88	208.91	427.93	332.60	488.40	355.30
0.344	563.80	352.58	359.16	215.59	412.55	259.60	477.61	407.76
0.412	547.29	352.58	362.47	219.19	417.75	243.69	497.80	352.58
0.481	505.26	383.41	344.90	184.22	342.68	226.11	460.02	376.97
0.55	483.98	316.27	346.15	204.25	366.28	231.97	430.40	356.63
0.618	460.69	309.28	324.45	182.95	313.83	180.82	428.60	320.53
0.687	380.22	302.52	276.09	158.47	316.89	140.79	400.55	279.22
0.756	335.76	246.39	271.32	119.01	293.67	118.25	349.63	160.66
0.824	272.59	275.52	240.78	103.35	217.76	84.40	321.24	161.35
0.893	243.72	160.57	160.82	94.98	193.80	51.71	261.59	81.03

Table A13. Conductivity Probe Group 14-Sensor Effective bubbles Before (B) and After (A) Diameter for jg of 0.05 (V1), 0.18 (V2), 0.30 (V3), and 0.7 (V4) per 300s

r/R	V1 B	V1 A	V2 B	V2 A	V3 B	V3 A	V4 B	V4 A
(-)	(#)	(#)	(#)	(#)	(#)	(#)	(#)	(#)
0	3150	1830	930	630	2040	1050	3060	2220
0.069	3240	1830	1320	870	1950	1290	2850	1590
0.138	3180	1740	1770	1170	1710	1020	3090	2160
0.206	3150	1680	1500	960	2580	1620	2670	1650
0.275	3090	1650	1410	900	2310	1650	3210	2070
0.344	3150	1740	1350	960	1980	1260	3060	2160
0.412	2760	1440	1500	660	1710	1140	2760	1950
0.481	2820	1470	1140	660	1560	1020	2520	1710
0.55	2400	1260	1350	810	1590	990	2400	1620
0.618	2250	1080	1260	750	1140	720	2010	1290
0.687	1860	870	990	570	750	480	1620	1050
0.756	1260	660	780	480	750	480	1110	660
0.824	960	450	690	450	480	270	780	510
0.893	390	240	750	210	270	150	660	390

Table A14. Conductivity Probe Group 1 VF Old and New Algorithm for jg of 0.05 (V1), 0.18 (V2), 0.30 (V3), and 0.7 (V4) Per Second

r/R	V1 Old	V1 New	V2 Old	V2 New	V3 Old	V3 New	V4 Old	V4 New
(-)	(-)	(-)	(-)	(-)	(-)	(-)	(-)	(-)
0	0.1243	0.1150	0.0926	0.0439	0.0892	0.1354	0.1081	0.1238
0.069	0.1276	0.1136	0.0886	0.0548	0.0845	0.1303	0.1199	0.1039
0.138	0.1218	0.1179	0.0997	0.0733	0.0778	0.1156	0.1398	0.1268
0.206	0.1282	0.1155	0.0963	0.0692	0.0829	0.1322	0.1218	0.1083
0.275	0.1199	0.1125	0.0987	0.0701	0.1022	0.1416	0.1199	0.1367
0.344	0.1137	0.1054	0.0925	0.0563	0.0775	0.1368	0.1347	0.1229
0.412	0.1137	0.1112	0.0962	0.0631	0.0772	0.1180	0.1137	0.1229
0.481	0.1278	0.1135	0.0833	0.0557	0.0725	0.0965	0.1384	0.1176
0.55	0.1098	0.1086	0.0925	0.0605	0.0769	0.1104	0.1314	0.1605
0.618	0.1090	0.1095	0.0910	0.0583	0.0621	0.1017	0.1098	0.1522
0.687	0.1024	0.0980	0.0833	0.0472	0.0407	0.0878	0.0994	0.1461
0.756	0.0726	0.0920	0.0724	0.0408	0.0415	0.0913	0.0764	0.1293
0.824	0.0745	0.0846	0.0710	0.0368	0.0261	0.0728	0.0277	0.1191
0.893	0.0426	0.0751	0.0831	0.0417	0.0112	0.0611	0.0394	0.0932

Table A15. Conductivity Probe Group 2 VF Old and New Algorithm for jg = 0.05 (V1), 0.18 (V2), 0.30 (V3), and 0.7 (V4) Per Second

r/R	V1	V1	V2	V2	V3	V3	V4	V4
	Old	New	Old	New	Old	New	Old	New
(-)	(-)	(-)	(-)	(-)	(-)	(-)	(-)	(-)
0	0.0255	0.0626	0.2283	0.1949	0.3433	0.2915	0.5880	0.4429
0.069	0.0226	0.0701	0.2174	0.2088	0.3386	0.2951	0.5230	0.4365
0.138	0.0224	0.0719	0.2196	0.2041	0.3382	0.3104	0.5412	0.4681
0.206	0.0229	0.0739	0.2314	0.2542	0.3277	0.2869	0.5747	0.4912
0.275	0.0230	0.0645	0.1987	0.2114	0.3533	0.2863	0.5230	0.4263
0.344	0.0241	0.0695	0.2148	0.1881	0.3103	0.2768	0.5158	0.4168
0.412	0.0241	0.0689	0.1876	0.2008	0.2503	0.2539	0.5241	0.3918
0.481	0.0177	0.0676	0.1617	0.2000	0.2481	0.2648	0.4133	0.3729
0.55	0.0182	0.0652	0.1772	0.1881	0.2181	0.2446	0.3614	0.3010
0.618	0.0224	0.0703	0.1473	0.1671	0.1740	0.1850	0.3102	0.2583
0.687	0.0179	0.0712	0.1316	0.1634	0.1455	0.1707	0.2389	0.2343
0.756	0.0212	0.0649	0.1148	0.1560	0.1022	0.1225	0.1536	0.1665
0.824	0.0244	0.0602	0.0896	0.1138	0.0649	0.1071	0.0819	0.1276
0.893	0.0380	0.0681	0.0566	0.0905	0.0283	0.1033	0.0471	0.1032

Table A16. Conductivity Probe Total VF Old and New Algorithm for jg of 0.05 (V1), 0.18 (V2), 0.30 (V3), and 0.7 (V4) Per Second

r/R	V1 Old	V1 New	V2 Old	V2 New	V3 Old	V3 New	V4 Old	V4 New
(-)	(-)	(-)	(-)	(-)	(-)	(-)	(-)	(-)
0	0.1499	0.1777	0.2722	0.2875	0.4327	0.4270	0.6960	0.5667
0.069	0.1502	0.1836	0.2722	0.2973	0.4231	0.4254	0.6430	0.5404
0.138	0.1442	0.1899	0.2929	0.3038	0.4160	0.4260	0.6810	0.5950
0.206	0.1510	0.1893	0.3006	0.3505	0.4107	0.4190	0.6965	0.5997
0.275	0.1430	0.1770	0.2688	0.3101	0.4555	0.4280	0.6430	0.5631
0.344	0.1378	0.1749	0.2711	0.2807	0.3880	0.4138	0.6505	0.5397
0.412	0.1378	0.1801	0.2507	0.2970	0.3275	0.3719	0.6378	0.5147
0.481	0.1456	0.1810	0.2174	0.2834	0.3207	0.3614	0.5518	0.4905
0.55	0.1280	0.1739	0.2377	0.2807	0.2951	0.3551	0.4927	0.4615
0.618	0.1314	0.1798	0.2058	0.2583	0.2361	0.2867	0.4199	0.4106
0.687	0.1204	0.1692	0.1788	0.2468	0.1862	0.2585	0.3383	0.3804
0.756	0.0938	0.1569	0.1557	0.2285	0.1437	0.2137	0.2299	0.2959
0.824	0.0991	0.1447	0.1264	0.1848	0.0911	0.1799	0.1099	0.2467
0.893	0.0807	0.1432	0.0983	0.1737	0.0395	0.1645	0.0865	0.1963

Table A17. Conductivity Probe Group 1 IAC Old and New Algorithm for jg of 0.05 (V1), 0.18 (V2), 0.30 (V3), and 0.7 (V4) Per Second

r/R	V1	V1	V2	V2	V3	V3	V4	V4
	Old	New	Old	New	Old	New	Old	New
(-)	(1/m)	(1/m)	(1/m)	(1/m)	(1/m)	(1/m)	(1/m)	(1/m)
0	305.83	439.79	54.99	243.80	92.01	315.20	68.98	274.25
0.069	279.68	414.07	56.67	200.43	76.53	285.95	92.09	395.69
0.138	313.12	410.56	108.66	250.72	86.13	269.91	108.07	297.20
0.206	357.25	437.34	31.75	235.92	81.02	254.24	85.23	237.40
0.275	292.09	416.34	89.05	236.62	121.86	365.49	92.09	334.74
0.344	282.33	393.58	70.08	230.04	76.77	295.38	108.70	310.43
0.412	282.33	390.24	88.02	237.21	93.09	288.64	82.33	277.97
0.481	337.63	403.39	67.90	220.46	80.55	246.11	125.95	265.65
0.55	266.43	359.21	82.42	229.68	88.69	278.96	129.03	310.97
0.618	247.61	333.30	79.02	216.46	68.67	244.93	113.07	309.69
0.687	251.11	314.22	60.81	186.74	46.93	179.98	106.12	286.92
0.756	181.53	288.07	47.91	178.15	39.41	184.76	72.89	294.89
0.824	192.82	220.83	54.16	181.61	37.13	161.20	80.67	252.88
0.893	72.19	221.83	50.46	205.33	24.26	106.70	46.04	243.87

Table A18. Conductivity Probe Group 2 IAC Old and New Algorithm for jg of 0.05 (V1), 0.18 (V2), 0.30 (V3), and 0.7 (V4) Per Second

r/R	V1	V1	V2	V2	V3	V3	V4	V4
	Old	New	Old	New	Old	New	Old	New
(-)	(1/m)	(1/m)	(1/m)	(1/m)	(1/m)	(1/m)	(1/m)	(1/m)
0	63.76	361.85	102.61	288.38	204.44	345.70	294.67	505.73
0.069	54.98	349.42	107.54	279.68	199.95	373.17	263.22	448.53
0.138	53.10	367.79	140.35	287.26	213.13	369.88	309.35	521.44
0.206	58.94	379.01	138.85	294.47	204.21	320.35	301.58	587.67
0.275	63.22	361.53	119.86	270.08	210.75	304.13	263.22	506.88
0.344	70.25	341.25	145.51	253.16	182.83	331.21	299.06	562.67
0.412	70.25	305.47	131.17	263.29	150.60	317.37	270.25	472.86
0.481	45.79	327.44	116.32	259.93	145.56	299.01	251.02	417.66
0.55	49.84	302.36	121.83	253.16	143.28	319.90	227.60	384.26
0.618	61.67	322.75	103.93	225.11	112.15	245.34	207.46	314.82
0.687	51.41	280.15	97.67	208.78	93.86	179.02	106.12	310.97
0.756	64.86	198.22	71.10	188.36	78.84	142.43	72.89	225.15
0.824	82.70	182.95	49.18	150.97	47.27	105.09	80.67	168.03
0.893	88.38	184.92	44.52	121.46	27.45	48.95	46.04	160.81

Table A19. Conductivity Probe Total IAC Old and New Algorithm for jg of 0.05 (V1), 0.18 (V2), 0.30 (V3), and 0.7 (V4) Per Second

r/R	V1	V1	V2	V2	V3	V3	V4	V4
	Old	New	Old	New	Old	New	Old	New
(-)	(1/m)	(1/m)	(1/m)	(1/m)	(1/m)	(1/m)	(1/m)	(1/m)
0	369.59	801.64	157.61	532.17	296.46	660.89	363.66	779.98
0.069	334.66	763.49	164.21	480.10	276.48	659.12	355.30	844.22
0.138	366.22	778.36	249.01	537.99	299.26	639.80	417.42	818.64
0.206	416.19	816.36	170.60	530.38	285.23	574.59	386.81	825.07
0.275	355.30	777.87	208.91	506.70	332.60	669.61	355.30	841.62
0.344	352.58	734.83	215.59	483.21	259.60	626.59	407.76	873.10
0.412	352.58	695.71	219.19	500.50	243.69	606.01	352.58	750.83
0.481	383.41	730.83	184.22	480.39	226.11	545.12	376.97	683.31
0.55	316.27	661.57	204.25	482.85	231.97	598.86	356.63	695.24
0.618	309.28	656.05	182.95	441.57	180.82	490.27	320.53	624.51
0.687	302.52	594.37	158.47	395.52	140.79	359.00	279.22	597.89
0.756	246.39	486.29	119.01	366.51	118.25	327.19	160.66	520.04
0.824	275.52	403.78	103.35	332.58	84.40	266.29	161.35	420.92
0.893	160.57	406.75	94.98	326.78	51.71	155.64	81.03	404.68

Table A20. Optical Probe Group 1 4-Sensor Effective Bubbles Before (B) and After (A) Diameter for jg of 0.05 (V1), 0.18 (V2), 0.30 (V3), and 0.7 (V4) per 300s

r/R	V1 B	V1 A	V2 B	V2 A	V3 B	V3 A	V4 B	V4 A
(-)	(#)	(#)	(#)	(#)	(#)	(#)	(#)	(#)
0	3600	2730	2370	1980	3240	2640	4680	4200
0.069	3780	2850	2280	1950	2820	2430	4560	4080
0.138	3930	2910	2280	1920	2700	2250	4650	4230
0.206	3660	2850	2280	1920	2970	2550	4350	3870
0.275	3240	2430	2190	1860	3090	2670	4230	3780
0.344	3030	2280	2070	1770	2640	2280	4110	3660
0.412	2970	2190	1950	1650	2460	2130	4440	3930
0.481	2490	1830	1650	1410	1920	1680	3600	3120
0.55	2460	1830	1620	1380	1920	1620	3120	2760
0.618	2040	1560	1710	1470	1680	1410	2970	2640
0.687	1560	1170	1380	1140	1530	1290	2670	2340
0.756	1230	1050	1320	1110	1290	1110	1980	1710
0.824	660	600	990	840	720	600	1770	1470
0.893	690	480	510	420	630	540	1320	1170

Table A21. Optical Probe Group 1 VF Old and New Algorithm for jg of 0.05 (V1), 0.18 (V2), 0.30 (V3), and 0.7 (V4) Per Second

r/R	V1	V1	V2	V2	V3	V3	V4	V4
	Old	New	Old	New	Old	New	Old	New
(-)	(-)	(-)	(-)	(-)	(-)	(-)	(-)	(-)
0	0.1762	0.1479	0.1208	0.1102	0.2033	0.1254	0.1365	0.1282
0.069	0.1820	0.1543	0.1165	0.1090	0.2047	0.1633	0.1344	0.1273
0.138	0.1881	0.1577	0.1214	0.1090	0.1915	0.1233	0.1320	0.1257
0.206	0.1802	0.1551	0.1201	0.1076	0.1190	0.1276	0.1306	0.1237
0.275	0.1806	0.1567	0.1135	0.1036	0.1248	0.1404	0.1353	0.1260
0.344	0.1799	0.1553	0.1172	0.1079	0.1209	0.1104	0.1364	0.1290
0.412	0.1710	0.1446	0.1123	0.1042	0.1165	0.1074	0.1401	0.1299
0.481	0.1622	0.1387	0.1069	0.1001	0.1127	0.1090	0.1374	0.1256
0.55	0.1602	0.1390	0.1080	0.0982	0.1116	0.1033	0.1366	0.1261
0.618	0.1526	0.1317	0.1021	0.0958	0.1093	0.1078	0.1447	0.1322
0.687	0.1383	0.1224	0.0921	0.1014	0.1138	0.1052	0.1426	0.1325
0.756	0.1309	0.1133	0.0975	0.0876	0.1059	0.1002	0.1318	0.1239
0.824	0.1106	0.1128	0.0884	0.0820	0.0914	0.0855	0.1323	0.1235
0.893	0.1072	0.0893	0.0772	0.0664	0.0884	0.0885	0.1239	0.1171

Table A22. Optical Probe Group 2 VF Old and New Algorithm for jg of 0.05 (V1), 0.18 (V2), 0.30 (V3), and 0.7 (V4) Per Second

r/R	V1	V1	V2	V2	V3	V3	V4	V4
	Old	New	Old	New	Old	New	Old	New
(-)	(-)	(-)	(-)	(-)	(-)	(-)	(-)	(-)
0	0.0190	0.0452	0.2216	0.2271	0.1986	0.3373	0.5083	0.5163
0.069	0.0200	0.0454	0.2429	0.2385	0.1912	0.2753	0.5193	0.5256
0.138	0.0157	0.0446	0.2288	0.2385	0.2050	0.3236	0.4985	0.5032
0.206	0.0163	0.0396	0.2152	0.2282	0.2869	0.2936	0.4978	0.5020
0.275	0.0208	0.0400	0.2282	0.2369	0.2375	0.2805	0.4785	0.4860
0.344	0.0186	0.0418	0.2022	0.2096	0.2889	0.3012	0.4631	0.4686
0.412	0.0204	0.0461	0.1958	0.2039	0.2672	0.2729	0.4408	0.4497
0.481	0.0222	0.0440	0.1738	0.1813	0.2403	0.2456	0.3879	0.3978
0.55	0.0268	0.0474	0.1641	0.1738	0.2222	0.2347	0.3502	0.3573
0.618	0.0163	0.0355	0.1761	0.1812	0.2009	0.2032	0.3129	0.3227
0.687	0.0214	0.0355	0.1501	0.1432	0.1757	0.1832	0.2636	0.2720
0.756	0.0174	0.0328	0.1190	0.1281	0.1292	0.1336	0.2219	0.2291
0.824	0.0182	0.0236	0.1061	0.1112	0.0896	0.0908	0.1743	0.1805
0.893	0.0186	0.0331	0.0531	0.0484	0.0726	0.0523	0.1311	0.1337

Table A23. Optical Probe Total VF Old and New Algorithm for jg of 0.05 (V1), 0.18 (V2), 0.30 (V3), and 0.7 (V4) Per Second

r/R	V1	V1	V2	V2	V3	V3	V4	V4
	Old	New	Old	New	Old	New	Old	New
(-)	(-)	(-)	(-)	(-)	(-)	(-)	(-)	(-)
0	0.1953	0.1932	0.3425	0.3374	0.4020	0.4628	0.6448	0.6447
0.069	0.2019	0.1998	0.3595	0.3478	0.3959	0.4387	0.6538	0.6529
0.138	0.2038	0.2024	0.3509	0.3478	0.3965	0.4470	0.6306	0.6289
0.206	0.1965	0.1948	0.3353	0.3358	0.4059	0.4214	0.6284	0.6257
0.275	0.2014	0.1969	0.3417	0.3405	0.3622	0.4210	0.6138	0.6120
0.344	0.1985	0.1971	0.3194	0.3175	0.4098	0.4116	0.5995	0.5977
0.412	0.1914	0.1907	0.3082	0.3081	0.3837	0.3803	0.5810	0.5796
0.481	0.1843	0.1829	0.2807	0.2814	0.3530	0.3546	0.5254	0.5234
0.55	0.1871	0.1864	0.2721	0.2720	0.3338	0.3380	0.4868	0.4834
0.618	0.1690	0.1673	0.2781	0.2770	0.3102	0.3110	0.4577	0.4550
0.687	0.1597	0.1579	0.2423	0.2446	0.2895	0.2884	0.4062	0.4045
0.756	0.1484	0.1461	0.2165	0.2158	0.2351	0.2338	0.3537	0.3530
0.824	0.1289	0.1363	0.1945	0.1932	0.1811	0.1763	0.3066	0.3041
0.893	0.1258	0.1224	0.1303	0.1149	0.1610	0.1409	0.2550	0.2509

Table A24. Optical Probe Group 1 IAC Old and New Algorithm for jg of 0.05 (V1), 0.18 (V2), 0.30 (V3), and 0.7 (V4) Per Second

r/R	V1	V1	V2	V2	V3	V3	V4	V4
	Old	New	Old	New	Old	New	Old	New
(-)	(1/m)	(1/m)	(1/m)	(1/m)	(1/m)	(1/m)	(1/m)	(1/m)
0	556	305.83	248.28	54.99	308.98	92.01	228.01	68.98
0.069	571.31	279.68	238.99	56.67	315.28	76.53	224.6	92.09
0.138	588.08	313.12	249.16	108.66	277.87	86.13	228.51	108.07
0.206	550.99	357.25	250.1	31.75	232.8	81.02	222.97	85.23
0.275	539.52	292.09	232.38	89.05	244.65	121.86	232.59	92.09
0.344	517.03	282.33	222.86	70.08	230.08	76.77	235.11	108.7
0.412	504.37	282.33	224.44	88.02	235.75	93.09	251.7	82.33
0.481	461.22	337.63	217.06	67.9	195.33	80.55	238.41	125.95
0.55	431.83	266.43	220.82	82.42	216.59	88.69	227.02	129.03
0.618	422.6	247.61	196.54	79.02	186.88	68.67	241.86	113.07
0.687	348.6	251.11	169.04	60.81	198.49	46.93	240.33	106.12
0.756	307.75	181.53	193.09	47.91	203.13	39.41	226.27	72.89
0.824	237.47	192.82	164.1	54.16	159.49	37.13	226.96	80.67
0.893	220.39	72.19	121.57	50.46	146.91	24.26	189.98	46.04

Table A25. Optical Probe Group 2 IAC Old and New Algorithm for jg of0.05 (V1), 0.18 (V2), 0.30 (V3), and 0.7 (V4) Per Second

r/R	V1	V1	V2	V2	V3	V3	V4	V4
	Old	New	Old	New	Old	New	Old	New
(-)	(1/m)	(1/m)	(1/m)	(1/m)	(1/m)	(1/m)	(1/m)	(1/m)
0	47.81	185.48	157.62	186.66	225.68	259.34	280.89	302.76
0.069	52.40	198.79	155.84	195.56	215.77	245.66	297.73	321.01
0.138	38.36	192.12	161.84	195.56	197.42	256.33	280.18	290.92
0.206	40.80	167.31	144.60	179.18	197.62	247.94	284.40	304.51
0.275	51.55	169.01	165.50	195.49	183.29	233.37	255.81	280.67
0.344	46.76	165.92	136.30	165.69	182.47	208.88	242.49	259.78
0.412	42.92	173.37	138.02	166.35	182.00	205.82	246.10	279.39
0.481	44.04	158.85	127.84	153.80	147.34	172.24	221.62	246.50
0.55	52.15	154.27	125.33	154.90	149.69	171.95	203.37	228.59
0.618	38.09	129.12	127.91	124.09	126.95	149.86	186.74	210.06
0.687	31.62	103.35	107.06	110.52	118.41	143.43	160.22	181.77
0.756	28.01	105.26	78.24	94.73	90.54	110.26	123.36	138.76
0.824	35.11	48.51	76.67	77.48	58.27	70.88	94.28	121.40
0.893	23.33	77.81	39.25	40.10	46.89	39.41	71.62	83.45

Table A26. Optical Probe Total IAC Old and New Algorithm for jg of 0.05 (V1), 0.18 (V2), 0.30 (V3), and 0.7 (V4) Per Second

r/R	V1	V1	V2	V2	V3	V3	V4	V4
	Old	New	Old	New	Old	New	Old	New
(-)	(1/m)	(1/m)	(1/m)	(1/m)	(1/m)	(1/m)	(1/m)	(1/m)
0	603.81	369.59	405.91	157.61	554.66	296.46	508.89	363.66
0.069	623.71	334.66	394.84	164.21	601.05	276.48	522.33	355.3
0.138	626.44	366.22	411.01	249.01	525.28	299.26	508.69	417.42
0.206	591.79	416.19	394.7	170.6	430.42	285.23	507.37	386.81
0.275	591.07	355.3	397.88	208.91	427.93	332.6	488.4	355.3
0.344	563.8	352.58	359.16	215.59	412.55	259.6	477.61	407.76
0.412	547.29	352.58	362.47	219.19	417.75	243.69	497.8	352.58
0.481	505.26	383.41	344.9	184.22	342.68	226.11	460.02	376.97
0.55	483.98	316.27	346.15	204.25	366.28	231.97	430.4	356.63
0.618	460.69	309.28	324.45	182.95	313.83	180.82	428.6	320.53
0.687	380.22	302.52	276.09	158.47	316.89	140.79	400.55	279.22
0.756	335.76	246.39	271.32	119.01	293.67	118.25	349.63	160.66
0.824	272.59	275.52	240.78	103.35	217.76	84.4	321.24	161.35
0.893	243.72	160.57	160.82	94.98	193.8	51.71	261.59	81.03

Table A27. Optical Probe (OP) and Conductivity Probe (CP) Group 1 VF New Algorithm for jg of 0.05 (V1), 0.18 (V2), 0.30 (V3), and 0.7 (V4) Per Second

r/R	V1	V1	V2	V2	V3	V3	V4	V4
	OP	CP	OP	CP	OP	CP	OP	CP
(-)	(-)	(-)	(-)	(-)	(-)	(-)	(-)	(-)
0	0.1479	0.1150	0.1102	0.0439	0.1254	0.1354	0.1282	0.1238
0.069	0.1543	0.1136	0.1090	0.0548	0.1633	0.1303	0.1273	0.1039
0.138	0.1577	0.1179	0.1090	0.0733	0.1233	0.1156	0.1257	0.1268
0.206	0.1551	0.1155	0.1076	0.0692	0.1276	0.1322	0.1237	0.1083
0.275	0.1567	0.1125	0.1036	0.0701	0.1404	0.1416	0.1260	0.1367
0.344	0.1553	0.1054	0.1079	0.0563	0.1104	0.1368	0.1290	0.1229
0.412	0.1446	0.1112	0.1042	0.0631	0.1074	0.1180	0.1299	0.1229
0.481	0.1387	0.1135	0.1001	0.0557	0.1090	0.0965	0.1256	0.1176
0.55	0.1390	0.1086	0.0982	0.0605	0.1033	0.1104	0.1261	0.1605
0.618	0.1317	0.1095	0.0958	0.0583	0.1078	0.1017	0.1322	0.1522
0.687	0.1224	0.0980	0.1014	0.0472	0.1052	0.0878	0.1325	0.1461
0.756	0.1133	0.0920	0.0876	0.0408	0.1002	0.0913	0.1239	0.1293
0.824	0.1128	0.0846	0.0820	0.0368	0.0855	0.0728	0.1235	0.1191
0.893	0.0893	0.0751	0.0664	0.0417	0.0885	0.0611	0.1171	0.0932

Table A28. Optical Probe (OP) and Conductivity Probe (CP) Group 2 VF New Algorithm for jg of 0.05 (V1), 0.18 (V2), 0.30 (V3), and 0.7 (V4) Per Second

r/R	V1	V1	V2	V2	V3	V3	V4	V4
	OP	CP	OP	CP	OP	CP	OP	CP
(-)	(-)	(-)	(-)	(-)	(-)	(-)	(-)	(-)
0	0.0452	0.0626	0.2271	0.1949	0.3373	0.2915	0.5163	0.4429
0.069	0.0454	0.0701	0.2385	0.2088	0.2753	0.2951	0.5256	0.4365
0.138	0.0446	0.0719	0.2385	0.2041	0.3236	0.3104	0.5032	0.4681
0.206	0.0396	0.0739	0.2282	0.2542	0.2936	0.2869	0.5020	0.4912
0.275	0.0400	0.0645	0.2369	0.2114	0.2805	0.2863	0.4860	0.4263
0.344	0.0418	0.0695	0.2096	0.1881	0.3012	0.2768	0.4686	0.4168
0.412	0.0461	0.0689	0.2039	0.2008	0.2729	0.2539	0.4497	0.3918
0.481	0.0440	0.0676	0.1813	0.2000	0.2456	0.2648	0.3978	0.3729
0.55	0.0474	0.0652	0.1738	0.1881	0.2347	0.2446	0.3573	0.3010
0.618	0.0355	0.0703	0.1812	0.1671	0.2032	0.1850	0.3227	0.2583
0.687	0.0355	0.0712	0.1432	0.1634	0.1832	0.1707	0.2720	0.2343
0.756	0.0328	0.0649	0.1281	0.1560	0.1336	0.1225	0.2291	0.1665
0.824	0.0236	0.0602	0.1112	0.1138	0.0908	0.1071	0.1805	0.1276
0.893	0.0331	0.0681	0.0484	0.0905	0.0523	0.1033	0.1337	0.1032

Table A29. Optical Probe (OP) and Conductivity Probe (CP) Total VF New Algorithm for jg of 0.05 (V1), 0.18 (V2), 0.30 (V3), and 0.7 (V4) Per Second

r/R	V1	V1	V2	V2	V3	V3	V4	V4
	OP	CP	OP	CP	OP	CP	OP	CP
(-)	(-)	(-)	(-)	(-)	(-)	(-)	(-)	(-)
0	0.1932	0.1777	0.3374	0.2875	0.4628	0.4270	0.6447	0.5667
0.069	0.1998	0.1836	0.3478	0.2973	0.4387	0.4254	0.6529	0.5404
0.138	0.2024	0.1899	0.3478	0.3038	0.4470	0.4260	0.6289	0.5950
0.206	0.1948	0.1893	0.3358	0.3505	0.4214	0.4190	0.6257	0.5997
0.275	0.1969	0.1770	0.3405	0.3101	0.4210	0.4280	0.6120	0.5631
0.344	0.1971	0.1749	0.3175	0.2807	0.4116	0.4138	0.5977	0.5397
0.412	0.1907	0.1801	0.3081	0.2970	0.3803	0.3719	0.5796	0.5147
0.481	0.1829	0.1810	0.2814	0.2834	0.3546	0.3614	0.5234	0.4905
0.55	0.1864	0.1739	0.2720	0.2807	0.3380	0.3551	0.4834	0.4615
0.618	0.1673	0.1798	0.2770	0.2583	0.3110	0.2867	0.4550	0.4106
0.687	0.1579	0.1692	0.2446	0.2468	0.2884	0.2585	0.4045	0.3804
0.756	0.1461	0.1569	0.2158	0.2285	0.2338	0.2137	0.3530	0.2959
0.824	0.1363	0.1447	0.1932	0.1848	0.1763	0.1799	0.3041	0.2467
0.893	0.1224	0.1432	0.1149	0.1737	0.1409	0.1645	0.2509	0.1963

Table A30. Optical Probe (OP) and Conductivity Probe (CP) Group 1 IAC New Algorithm for jg of 0.05 (V1), 0.18 (V2), 0.30 (V3), and 0.7 (V4) Per Second

r/R	V1	V1	V2	V2	V3	V3	V4	V4
	OP	CP	OP	CP	OP	CP	OP	CP
(-)	(1/m)	(1/m)	(1/m)	(1/m)	(1/m)	(1/m)	(1/m)	(1/m)
0	472.44	439.79	244.56	243.80	248.28	315.20	223.47	274.25
0.069	487.69	414.07	239.27	200.43	266.34	285.95	219.796	395.69
0.138	494.59	410.56	238.53	250.72	257.12	269.91	226.063	297.20
0.206	476.93	437.34	247.92	235.92	252.96	254.24	218.4601	237.40
0.275	455.38	416.34	228.43	236.62	299.78	365.49	228.8173	334.74
0.344	448.43	393.58	211.85	230.04	219.96	295.38	234.7424	310.43
0.412	425.45	390.24	223.83	237.21	232.74	288.64	247.9924	277.97
0.481	392.39	403.39	214.48	220.46	216.59	246.11	233.6641	265.65
0.55	371.32	359.21	210.90	229.68	214.75	278.96	224.9457	310.97
0.618	360.66	333.30	193.70	216.46	209.46	244.93	242.4448	309.69
0.687	308.13	314.22	200.34	186.74	206.90	179.98	240.0897	286.92
0.756	269.24	288.07	180.41	178.15	216.15	184.76	224.1961	294.89
0.824	244.94	220.83	160.83	181.61	170.68	161.20	233.7487	252.88
0.893	183.09	221.83	153.85	205.33	208.53	106.70	206.8512	243.87

Table A31. Optical Probe (OP) and Conductivity Probe (CP) Group 2 IAC New Algorithm for jg of 0.05 (V1), 0.18 (V2), 0.30 (V3), and 0.7 (V4) Per Second

r/R	V1	V1	V2	V2	V3	V3	V4	V4
	OP	CP	OP	CP	OP	CP	OP	CP
(-)	(1/m)	(1/m)	(1/m)	(1/m)	(1/m)	(1/m)	(1/m)	(1/m)
0	185.48	361.85	186.66	288.38	259.34	345.70	302.76	505.73
0.069	198.79	349.42	195.56	279.68	245.66	373.17	321.01	448.53
0.138	192.12	367.79	195.56	287.26	256.33	369.88	290.92	521.44
0.206	167.31	379.01	179.18	294.47	247.94	320.35	304.51	587.67
0.275	169.01	361.53	195.49	270.08	233.37	304.13	280.67	506.88
0.344	165.92	341.25	165.69	253.16	208.88	331.21	259.78	562.67
0.412	173.37	305.47	166.35	263.29	205.82	317.37	279.39	472.86
0.481	158.85	327.44	153.80	259.93	172.24	299.01	246.50	417.66
0.55	154.27	302.36	154.90	253.16	171.95	319.90	228.59	384.26
0.618	129.12	322.75	124.09	225.11	149.86	245.34	210.06	314.82
0.687	103.35	280.15	110.52	208.78	143.43	179.02	181.77	310.97
0.756	105.26	198.22	94.73	188.36	110.26	142.43	138.76	225.15
0.824	48.51	182.95	77.48	150.97	70.88	105.09	121.40	168.03
0.893	77.81	184.92	40.10	121.46	39.41	48.95	83.45	160.81

Table A32. Optical Probe (OP) and Conductivity Probe (CP) Total IAC New Algorithm
for jg of 0.05 (V1), 0.18 (V2), 0.30 (V3), and 0.7 (V4) Per Second

r/R	V1	V1	V2	V2	V3	V3	V4	V4
	OP	CP	OP	CP	OP	CP	OP	CP
(-)	(1/m)	(1/m)	(1/m)	(1/m)	(1/m)	(1/m)	(1/m)	(1/m)
0	657.92	801.64	431.22	532.17	507.62	660.89	526.22	779.98
0.069	686.49	763.48	434.83	480.10	512.00	659.11	540.81	844.22
0.138	686.71	778.35	434.09	537.99	513.45	639.79	516.985	818.64
0.206	644.25	816.35	427.10	530.38	500.89	574.58	522.97	825.07
0.275	624.39	777.86	423.92	506.70	533.15	669.61	509.48	841.62
0.344	614.35	734.82	377.54	483.21	428.84	626.588	494.52	873.10
0.412	598.82	695.71	390.18	500.50	438.56	606.014	527.38	750.83
0.481	551.23	730.82	368.27	480.39	388.82	545.12	480.15	683.31
0.55	525.59	661.57	365.79	482.85	386.69	598.86	453.53	695.24
0.618	489.78	656.04	317.79	441.57	359.32	490.26	452.50	624.51
0.687	411.47	594.36	310.86	395.52	350.32	358.99	421.85	597.89
0.756	374.5	486.28	275.13	366.51	326.40	327.19	362.95	520.04
0.824	293.45	403.78	238.31	332.58	241.55	266.28	355.14	420.92
0.893	260.89	406.74	193.95	326.78	247.93	155.64	290.30	404.68

BIBLIOGRAPHY

[1]   M. Ishii, Thermo-fluid dynamic theory of two-phase flow. Paris: Eyrolles, 1975.

[2]   M. Ishii and S. T. Revankar, Measurement of interfacial area using four-sensor probe in two phase flow, Purdue University Report, PU NE-91-1, 1991.

[3]   M. Ishii and S. Kim, "Micro four-sensor probe measurement of interfacial area transport for bubbly flow in round pipes," Nuclear Engineering and Design, vol. 205, no. 1-2, pp. 123–131, 2001.

[4]   M. Ishii and K. Mishima, "Two-fluid Model and Hydrodynamic Constitutive Relations." Nuclear Engineering and Design, vol. 82, pp.107-126, 1984.

[5]   M. Ishii and K. Mishima, "Study of two-fluid model and interfacial area." Argonne National Laboratory Report, ANL-80-11, 1980.

[6]   M. Ishii and N. Zuber, "Drag coefficient and relative velocity in bubbly, droplet or particulate flows," AIChE Journal, vol. 25, no. 5, pp. 843–855, 1979.

[7]   T. Chawla and M. Ishii, "Two-fluid model of two-phase flow in a pin bundle of a nuclear reactor," International Journal of Heat and Mass Transfer, vol. 23, no. 7, pp. 991–1001, 1980.

[8]   N. Zuber, "On the dispersed two-phase flow in the laminar flow regime," Chemical Engineering Science, vol. 19, no. 11, pp. 897–917, 1964.

[9]   P. Calderbank and M. Moo-Young, "The continuous phase heat and mass-transfer properties of dispersions," Chemical Engineering Science, vol. 16, no. 1-2, pp. 39–54, 1961.

[10]   B. Gal-Or and H. E. Hoelscher, "A mathematical treatment of the effect of particle size distribution on mass transfer in dispersions," AIChE Journal, vol. 12, no. 3, pp. 499–508, 1966.

[11]   B. Gal-Or and V. Walatka, "A theoretical analysis of some interrelationships and mechanisms of heat and mass transfer in dispersions," AIChE Journal, vol. 13, no. 4, pp. 650–657, 1967.

[12]   M. Ishii and G. Kojasoy, "Interfacial area transport equation and preliminary considerations on closure relations", Purdue University Report, PU NE-93-6, 1993.

[13]   G. Kocamustafaogullari and M. Ishii, "Foundation of the interfacial area transport equation and its closure relations," International Journal of Heat and Mass Transfer, vol. 38, no. 3, pp. 481–493, 1995.

[14]   L. Rayleigh, "On the Instability of Jets," Proceedings of the London Mathematical Society, vol. s1-10, no. 1, pp. 4–13, 1878.

[15]   R. Jackson, The formation and coalescence of drops and bubbles in liquids. London: The Institution of Chemical Engineers, 1964.

[16]   P. H. Calderbank, M. B. Moo-Young, and R. Bibbly, "Coalesence in bubble reactors and absorbers," Proceedings of the Third European Symposium on Chemical Reaction Engineering, Amsterdam, 1964.

[17]   W. Howarth, "Coalescence of drops in a turbulent flow field," Chemical Engineering Science, vol. 19, no. 1, pp. 33–38, 1964.

[18]   G. I. Taylor, "The formation of emulsion in definable field of flow," Proceedings of the Royal Society, London, United Kingdom, Series A, vol. 146, p. 501, 1934.

[19]   A.N. Kolmogorov, "On the disintegration of drops in a turbulent flow," Doklady Akad, vol. 66, p. 825, 1949.

[20]   B. K. Batchelor, "Pressure fluctuation in isotropic turbulence," Proceedings of the Cambridge Philosophical Society, vol. 47, part 2, pp. 359-371,1951

[21]   J. O. Hinze, "Fundamentals of the hydrodynamic mechanism of splitting in dispersion processes," AIChE Journal, vol. 1, no. 3, pp. 289–295, 1955.

[22]   R. M. Davies and G. Taylor, "The Mechanics of Large Bubbles Rising through Extended Liquids and through Liquids in Tubes," Proceedings of the Royal Society A: Mathematical, Physical and Engineering Sciences, vol. 200, no. 1062, pp. 375–390, Jul. 1950.

[23]   S. Kim, Z. Y. Fu, X. Wang, and M. Ishii, "The local interfacial area concentration measurements in a two-phase flow using a four-sensor conductivity probe," ANS Winter Meeting, Washington DC, 1998.

[24]   T. Hibiki and M. Ishii, "Two-group interfacial area transport equations at bubbly-to-slug flow transition," Nuclear Engineering and Design, vol. 202, no. 1, pp. 39–76, 2000.

[25]   M. Ishii and S. Kim, "Development of One-Group and Two-Group Interfacial Area Transport Equation," Nuclear Science and Engineering, vol. 146, no. 3, pp. 257–273, 2004.

[26] R. J. Fruehan and L. J. Matornik, Proceedings of the 3rd International Iron and Steel Congress, pp. 229-38, 1978.

[27] S. H. Kim and R. J. Fruehan, Metallurgical Transactions B, vol. 18B, pp. 673-680, 1987.

[28] J. C. Charpentier, Advanced Chemical Engineering, vol. 11, pp. 1-133, 1981.

[29] P. V. Danckwerts, Gas-Liquid Reaction, New York, NY, McGraw-Hill, pp. 6-151, 1970.

[30] K. R. Webersterterp, W. P. van Swaaij, and A. A. Beenackers, Chemical Reactor Design and Operation, New York, NY, John Wiley & Sons, pp. 357-494, 1984.

[31] T. K. Sherwood, R. L. Pigford, C. R. Wilke, and T. K. Sherwood, Mass transfer. New York: McGraw-Hill, 1975.

[32] M. Ishii, "Interfacial area in two-phase flow," The American Society of Mechanical Engineers Heat Transfer Division, vol. H0075, pp 1-5, 1992

[33] J. Landau, J. Boyle, H. G. Gomaa, and A. M. A. Taweel, "Comparison of methods for measuring interfacial areas in gas-liquid dispersions," The Canadian Journal of Chemical Engineering, vol. 55, no. 1, pp. 13-18, 1977.

[34] H. M. Prasser, A. Böttger, and J. Zschau, "A new electrode-mesh tomograph for gas–liquid flows," Flow Measurement and Instrumentation, vol. 9, no. 2, pp. 111–119, 1998.

[35] Z. Zhang, M. Bieberle, F. Barthel, L. Szalinski, and U. Hampel, "Investigation of upward cocurrent gas–liquid pipe flow using ultrafast X-ray tomography and wire-mesh sensor," Flow Measurement and Instrumentation, vol. 32, pp. 111–118, 2013.

[36] H. Shaban and S. Tavoularis, "Performance evaluation of conductivity wire-mesh sensors in vertical channels," Flow Measurement and Instrumentation, vol. 54, pp. 185–196, 2017.

[37] H.-M. Prasser and R. Häfeli, "Signal response of wire-mesh sensors to an idealized bubbly flow," Nuclear Engineering and Design, 2017.

[38] V. J. Trice and W. Rodger, "Light Transmittance as a Measure of Interfacial Area in Liquid-Liquid Dispersions," Jan. 1956.

[39] L. G. Neal and S. G. Bankoff, "A high resolution resistivity probe for determination of local void properties in gas-liquid flow," AIChE Journal, vol. 9, no. 4, pp. 490–494, 1963.

[40] Delhaye, J. M., and J. L. Achard, "On the averaging operators introduced in two-Phase flow modeling: Proceedings transient two-phase flow," CSNI Specialist Meeting, Toronto, 1976.

[41] S. Lo, "Application of the MUSIG model to bubbly flows," AEA Technology, vol. 1096, 1996.

[42] I. Kataoka, M. Ishii and A. Serizawa, "Local formulation of interfacial area and its measurements in two-phase flow." Argonne National Laboratory Report: NUREG series, ANL-84-68, 1984.

[43] I. Kataoka, M. Ishii, and A. Serizawa, "Local formulation and measurements of interfacial area concentration in two-phase flow," International Journal of Multiphase Flow, vol. 12, no. 4, pp. 505–529, 1986.

[44] I. Kataoka and A. Serizawa, "Interfacial area concentration in bubbly flow," Nuclear Engineering and Design, vol. 120, no. 2-3, pp. 163–180, 1990.

[45] S. Revankar and M. Ishii, "Local interfacial area measurement in bubbly flow," International Journal of Heat and Mass Transfer, vol. 35, no. 4, pp. 913–925, 1992.

[46] I. Kataoka, M. Ishii, and A. Serizawa, "Sensitivity analysis of bubble size and probe geometry on the measurements of interfacial area concentration in gas-liquid two-phase flow," Nuclear Engineering and Design, vol. 146, no. 1-3, pp. 53–70, 1994.

[47] S. Kim, X. Fu, X. Wang, and M. Ishii, "Development of the miniaturized four-sensor conductivity probe and the signal processing scheme," International Journal of Heat and Mass Transfer, vol. 43, no. 22, pp. 4101–4118, 2000.

[48] S. Kim, X. Fu, X. Wang, and M. Ishii, "Study on interfacial structures in slug flows using a miniaturized four-sensor conductivity probe," Nuclear Engineering and Design, vol. 204, no. 1-3, pp. 45–55, 2001.

[49] M. Ishii, S. Kim, and J. Uhle, "Interfacial area transport equation: model development and benchmark experiments," International Journal of Heat and Mass Transfer, vol. 45, no. 15, pp. 3111–3123, 2002.

[50] J. D. Talley, T. Worosz, and S. Kim, "Characterization of horizontal air–water two-phase flow in a round pipe part II: Measurement of local two-phase parameters in bubbly flow," International Journal of Multiphase Flow, vol. 76, pp. 223–236, 2015.

[51] X. Shen and H. Nakamura, "Spherical-bubble-based four-sensor probe signal processing algorithm for two-phase flow measurement," International Journal of Multiphase Flow, vol. 60, pp. 11–29, 2014.

[52]   N. Miller and R. E. Mitchie, in Two-Phase Flow instrumentation, ASME, 1969.

[53]   N. Miller and R. E. Mitchie, Journal of the British Nuclear Energy Society, vol. 9, p. 94, 1970.

[54]   F. Danel and J. M. Delhaye, Mesures, vol., Aug.-Sept., p.99, 1971.

[55]   J. M. Delhaye and J. O. C. Jones, "Summary on experimental methods for statistical transient analysis of two-phase gas-liquid flow. [BWR, PWR, and LMFBR]," Jan. 1976.

[56]   J. P. Galaup and J. M. Delhaye, "Utilization of the miniaturized optical probes for void fraction and gas velocity measurements in two-phase flow. [UTILISATION DE SONDES OPTIQUES MINIATURES EN ECOULEMENT DIPHASIQUE GAZ-LIQUIDE.,]" Houille Blanche, vol. 1, pp. 17-30, 1976.

[57]   N. Abuaf, O. J. Jones, and G. Zimmer, "Optical probe for local void fraction and interface velocity measurements. [BWR; PWR]," Jan. 1978.

[58]   J. J. Frijlink, "Physical aspects of gassed suspension reactors," Ph.D. Thesis, Delft University of Technology, Delft, Netherlands, 1987.

[59]   J. Xue, M. Al-Dahhan, M. P. Dudukovic, and R. F. Mudde, "Bubble Dynamics Measurements Using Four-Point Optical Probe," The Canadian Journal of Chemical Engineering, vol. 81, no. 3-4, pp. 375–381, 2008.

[60]   H. I. Farag, T. Mejdell, K. Hjarbo, P. Ege, M. Lysberg, A. Grislingås, and H. D. Lasa, "Fibre Optic and Capacitance Probes In Turbulent Fluidized Beds," Chemical Engineering Communications, vol. 157, no. 1, pp. 73–107, 1997.

[61]   D. Tian, C. Yan, and L. Sun, "Model of bubble velocity vector measurement in upward and downward bubbly two-phase flows using a four-sensor optical probe," Progress in Nuclear Energy, vol. 78, pp. 110–120, 2015.

[62]   W. D. Deckwer, V. H. Cottrell, and R. W. Field, Bubble Column Reactors, John Wiley and Sons, 1992.

[63]   R. Krishna and S. T. Sie, "Design and scale-up of the Fischer–Tropsch bubble column slurry reactor," Fuel Processing Technology, vol. 64, no. 1–3, pp. 73-105, 2000

[64]   M. Kagumba and M. H. Al-Dahhan, "Impact of Internals Size and Configuration on Bubble Dynamics in Bubble Columns for Alternative Clean Fuels Production," Industrial & Engineering Chemistry Research, vol. 54, no. 4, pp. 1359–1372, 2015.

[65] A. A. Youssef and M. H. Al-Dahhan, "Impact of Internals on the Gas Holdup and Bubble Properties of a Bubble Column," Industrial & Engineering Chemistry Research, vol. 48, no. 17, pp. 8007–8013, Feb. 2009.

[66] R. Buchholz and K. Schuger, "Bubble column bioreactors," European Journal of Applied Microbiology and Biotechnology, vol. 6, no. 4, pp. 301–313, 1979.

[67] K. Seungjin, "Interfacial Area Transport Equation and Measurement of Local Interfacial Characteristics," TESI Doctoral, Purdue University, West Lafayette, Indiana, 1999.

[68] M. Ishii, "One-dimensional drift-flux model and constitutive equations for relative motion between phases in various two-phase flow regimes," Jan. 1977.

[69] Q. Wu and M. Ishii, "Sensitivity study on double-sensor conductivity probe for the measurement of interfacial area concentration in bubbly flow," International Journal of Multiphase Flow, vol. 25, no. 1, pp. 155–173, 1999.

[70] T. Worosz, M. Bernard, R. Kong, A. Toptan, S. Kim, and C. Hoxie, "Sensitivity studies on the multi-sensor conductivity probe measurement technique for two-phase flows," Nuclear Engineering and Design, vol. 310, pp. 552–563, 2016.

[71] C. Shannon, "Communication in The Presence Of Noise," Proceedings of the IEEE, vol. 86, no. 2, pp. 447–457, 1998.

[72] A. Jerri, "The Shannon sampling theorem—Its various extensions and applications: A tutorial review," Proceedings of the IEEE, vol. 65, no. 11, pp. 1565–1596, 1977.

[73] X. Shen, Y. Saito, K. Mishima, and H. Nakamura, "Methodological improvement of an intrusive four-sensor probe for the multi-dimensional two-phase flow measurement," International Journal of Multiphase Flow, vol. 31, no. 5, pp. 593–617, 2005.

[74] X. Shen, K. Mishima, and H. Nakamura, "A method for measuring local instantaneous interfacial velocity vector in multi-dimensional two-phase flow," International Journal of Multiphase Flow, vol. 34, no. 5, pp. 502–509, 2008.

[75] X. Shen and H. Nakamura, "Local interfacial velocity measurement method using a four-sensor probe," International Journal of Heat and Mass Transfer, vol. 67, pp. 843–852, 2013.

[76] S. Paranjape, "Bubble Diameter Calculation." E-mail interview. 16 May 2016.

[77] M. J. Powell, "A Fortran Subroutine for Solving Systems of Nonlinear Algebraic Equations," in Numerical Methods for Nonlinear Algebraic Equations, Gordon and Breach, pp. 87-414, 1970.

VITA

Chandller Stephen-Leslie Mills has had a substantial interest in Physics and Mathematics since he was very young. Chandller graduated from Missouri University of Science and Technology completing his Bachelor of Science in Nuclear Engineering with a Minor in Mathematics May 2014 as summa cum laude. While working toward his bachelor's degree, Chandller worked as a technical assistant developing laboratory experiments for engineering students. Upon graduation, he was awarded the Nuclear Regulatory Commission's Graduate Fellowship and the Chancellor's Graduate Research Fellowship at Missouri University of Science and Technology in the nuclear engineering doctorate program under the guidance of Dr. Joshua Schlegel. In July 2018, he received his Ph.D. in Nuclear Engineering from Missouri University of Science and Technology.

Throughout his doctorate studies, he worked as part of the team to develop, design, and build Missouri University of Science and Technology's Thermal Hydraulics Laboratory (in Hypoint, Missouri) for the study of two phase flows and heat transfer research, supporting the development and improvements in the use of nuclear reactors. Chandller's major area of research has been in two-phase flows with an emphasis on void fraction and interfacial area concentration measurements directed towards improving the accuracy of the two-fluid model.